Optical Properties of Wurtzite InN and Related Alloys

DISSERTATION

zur Erlangung des akademischen Grades
doctor rerum naturalium (Dr. rer. nat.)

vorgelegt dem Rat der Fakultät für
Mathematik und Naturwissenschaften
der Technischen Universität Ilmenau

von
M.Sc. Egidijus Sakalauskas
geboren am 21.11.1982 in Panevėžys, Litauen

urn:nbn:de:gbv:ilm1-2012000326

1. Gutachter: Prof. Dr. rer. nat. habil. Rüdiger Goldhahn
(Otto-von-Guericke-Universität Magdeburg)

2. Gutachter: Prof. Dr. Norbert Esser
(Leibniz-Institut für Analytische Wissenschaften - ISAS - e.V.)

3. Gutachter: Priv. Doz. Dr. Stefan Krischok
(Technische Universität Ilmenau)

Tag der Einreichung: 7. März 2012
Tag der wissenschaftlichen Aussprache: 2. Oktober 2012

Dedicated to my parents

Abstract

In this work, the optical properties of wurtzite InN and related ternary InGaN and AlInN as well as quaternary AlInGaN alloys are investigated. The main focus is put on the spectroscopic ellipsometry characterization. The InN films grown on Si(111) substrates and carbon doped InN sample series are investigated from the mid-infrared up to vacuum-ultraviolet range. A carrier concentration is estimated by solving a self-consistent problem that consists of the infrared spectroscopic ellipsometry data analysis and the absorption onset fitting. The intrinsic strain-free band gap for InN samples is determined by taking into consideration the band-gap renormalization, the Burstein-Moss shift and the strain influence. The $\mathbf{k}\cdot\mathbf{p}$ method is employed in order to evaluate a strain-induced band-gap shift. It is shown that by increasing the flux of a carbon dopant CBr_4 during the molecular beam epitaxy growth process, the electron concentration increases in the grown InN samples. The In-related alloys are investigated in the spectral range from the near infrared up to vacuum ultraviolet. The analytical model permitting to describe the dielectric function of the alloys in the range 1-10 eV is presented. By applying the analytical model to the experimental dielectric function, the band-gap and high-energy inter-band transition energies are determined. The strain-free band-gap bowing parameters for ternary InGaN and AlInN are determined. It is found that the bowing parameter for AlInN alloy is composition dependent. With the knowledge of the ternary alloys bowing parameters, the empirical expression permitting to estimate the band gap of the quaternary alloys is developed. All the experimental band gaps determined for the alloys by spectroscopic ellipsometry are supported by the state-of-the-art *ab initio* data.

Contents

Acknowledgment

First of all, I would like to acknowledge my doctoral thesis supervisor prof. R. Goldhahn and my colleague dr. P. Schley for training me on ellipsometry characterization tool and useful scientific discussions. I thank prof. G. Gobsch for giving me an opportunity to stay at TU Ilmenau, Institute of Physics as well as S. Schneider and T. Nicolai for the administrative support. I also thank dr. P. Ruterana for an excellent EU project RAINBOW ITN coordination and workshops' organization. For the collaboration, I am grateful to H. Behmenburg, T. Öcal, dr. C. Giesen, dr. K. Christiansen, prof. M. Heuken from AIXTRON SE, L. C. de Carvalho and prof. F. Bechstedt from Friedrich-Schiller-Universität Jena, D. Van Dinh, M. Pristovsek, and prof. M. Kneissl from TU Berlin, B. Reuters, L. Rahimzadeh Khoshroo, and prof. A. Vescan from RWTH Aachen University, A. Kraus, R. Buß, dr. U. Rossow, and prof. A. Hangleiter from TU Braunschweig, D. Dobrovolskas and prof. G. Tamulaitis from Vilnius University, A. Eisenhardt, dr. S. Krischok, dr. S. Shokhovets, dr. M. Himmerlich, dr. J. Pezoldt, K. Tonisch, and F. Niebelshütz from TU Ilmenau, A. Knübel from IAF Freiburg, M. Wieneke, dr. A. Dadgar, J. Bläsing, and prof. A. Krost from OvGU Magdeburg, M. Neumann, M. Röppischer, C. Werner, dr. C. Cobet, and prof. N. Esser from ISAS Berlin, M.V. Rzheutski, dr. E.V. Lutsenko, and prof. G.P. Yablonskii from Stepanov Institute of Physics, National Academy of Science Belarus, and B. Holländer from FZ Jülich GmbH. For the financial support I acknowledge the European Commission (Grant agreement N:PITN-GA-2008-213238) and Helmholtz-Zentrum Berlin. Finally, I am grateful to my family for moral support.

List of publications in peer-reviewed journals

[1] E. Sakalauskas, P. Schley, J. Räthel, T. A. Klar, R. Müller, J. Pezoldt, K. Tonisch, J. Grandal, M. A. Sanchez-Garcia, E. Calleja, A. Vilalta-Clemente, P. Ruterana, and R. Goldhahn, *Optical properties of InN grown on Si(111) substrate*, Phys. Status Solidi A **207**, 1066 (2010).

[2] E. Sakalauskas, H. Behmenburg, C. Hums, P. Schley, G. Rossbach, C. Giesen, M. Heuken, H. Kalisch, R. H. Jansen, J. Bläsing, A. Dadgar, A. Krost, and R. Goldhahn, *Dielectric function and optical properties of Al-rich AlInN alloys pseudomorphically grown on GaN*, J. Phys. D: Appl. Phys. **43**, 365102 (2010).

[3] E. Sakalauskas, H. Behmenburg, P. Schley, G. Gobsch, C. Giesen, H. Kalisch, R. H. Jansen, M. Heuken, and R. Goldhahn, *Dielectric function of Al-rich AlInN in the range 1-18 eV*, Phys. Status Solidi A **208**, 1517 (2011).

[4] E. Sakalauskas, B. Reuters, L. Rahimzadeh Khoshroo, H. Kalisch, M. Heuken, A. Vescan, M. Röppischer, C. Cobet, G. Gobsch and R. Goldhahn, *Dielectric function and optical properties of quaternary AlInGaN alloys*, J. Appl. Phys. **110**, 013102 (2011).

[5] E. Sakalauskas, M. Wieneke, A. Dadgar, G. Gobsch, A. Krost, and R. Goldhahn, *Optical anisotropy of a-plane $Al_{0.8}In_{0.2}N$ grown on an a-plane GaN pseudosubstrate*, Phys. Status Solidi A **209**, 29 (2012).

[6] E. Sakalauskas, Ö. Tuna, A. Kraus, H. Bremers, U. Rossow, C. Giesen, M. Heuken, A. Hangleiter, G. Gobsch, and R. Goldhahn, *Dielectric function and bowing parameters of InGaN alloys*, Phys. Status Solidi B **249**, 485 (2012).

[7] P. Schley, J. Räthel, E. Sakalauskas, G. Gobsch, M. Wieneke, J. Bläsing, A. Krost, G. Koblmüller, J. S. Speck, and R. Goldhahn, *Optical anisotropy of A- and M-plane InN grown on free-standing GaN substrates*, Phys. Status Solidi A **207**, 1062 (2010).

[8] I. Hotovy, J. Pezoldt, M. Kadlecikova, T. Kups, L. Spiess, J. Breza, E. Sakalauskas, R. Goldhahn, and V. Rehacek, *Structural characterization of sputtered indium oxide films deposited at room temperature*, Thin Solid Films **208**, 4508 (2010).

[9] A. Kraus, S. Hammadi, J. Hisek, R. Buß, H. Jönen, H. Bremers, U. Rossow, E. Sakalauskas, R. Goldhahn, and A. Hangleiter, *Growth and characterization of InGaN by RF-MBE*, J. Cryst. Growth **323**, 72 (2011).

[10] B. Reuters, A. Wille, B. Holländer, E. Sakalauskas, N. Ketteniss, C. Mauder, R. Goldhahn, M. Heuken, H. Kalisch, and A. Vescan, *Growth studies on quaternary AlInGaN layers for HEMT application*, J. Electron. Mater. **41**, 905 (2012).

Contribution of the Author

The author made a contribution to this work by conducting spectroscopic ellipsometry measurements on the InN and In-related alloy samples. A commercial variable angle ellipsometer at TU Ilmenau and a synchrotron ellipsometer at the electron storage ring (BESSY II, Helmholtz-Zentrum Berlin) provided by prof. N. Esser (ISAS Berlin) were used. E. Sakalauskas also analyzed the *in-situ* growth of the InN epilayers in the metalorganic vapour phase epitaxy reactor during his research visit at AIXTRON SE as well as characterized the InGaN samples by using a confocal microscope at Vilnius University, Semiconductor Physics Department. He wrote the publications in the peer-reviewed journals [1–6] and made a contribution as a co-author for the publications [7–10] by providing the spectroscopic ellipsometry characterization data.

Used abbreviations

A, B, C	optical transitions $\Gamma_9^{\mathrm{v}} \to \Gamma_7^{\mathrm{c}}$, $\Gamma_{7+}^{\mathrm{v}} \to \Gamma_7^{\mathrm{c}}$, $\Gamma_{7-}^{\mathrm{v}} \to \Gamma_7^{\mathrm{c}}$, respectively
AFM	Atomic Force Microscopy
BGR	Band-gap renormalization
BMS	Burstein-Moss shift
BS	Band structure
BZ	Brillouin zone
CB	Conduction band
CBM	Conduction-band minimum
CP	Critical point
DF	Dielectric function
DFT	Density functional theory
EMA	Effective medium approximation
GW	Green's function
HEMT	High electron mobility transistor
IR	Infrared
IR-SE	Infrared spectroscopic ellipsometer
JDOS	Joined density of states
LD	Laser diode
LDA	Local density approximation
LED	Light emitting diode
LM	Lattice matched
LO	Longitudinal optical phonon mode
LPP	Longitudinal optical phonon-plasmon mode
MBE	Molecular beam epitaxy
MOVPE	Metalorganic vapour phase epitaxy
MSE	Mean-square error
PL	Photoluminescence
QP	Quasi particle
rms	Root mean square
RT	Room temperature
SE	Spectroscopic ellipsometry
SIC	Self-energy correction
TO	Transversal optical phonon mode
UHV	Ultra-high vacuum
UV	Ultraviolet
VB	Valence band
VBM	Valence band maximum
VUV	Vacuum ultraviolet
WZ	Wurtzite
XRD	X-ray diffraction

Used symbols

$\alpha(\omega)$	Absorption coefficient
Γ	Broadening energy
γ_{LO}	Broadening of the LO phonon mode
γ_{p}	Broadening of the plasma frequency
γ_{TO}	Braodening of the TO phonon mode
Δ	Ellipsometric parameter, phase shift
Δ_{BGR}	Band-gap reduction due to BGR effect
Δ_{cf}	Crystal field splitting energy
Δ_{so}	Spin-orbit splitting energy
$\bar{\varepsilon}(\omega)$, $\bar{\varepsilon}_{\mathrm{o}}(\omega)$, and $\bar{\varepsilon}_{\mathrm{e}}(\omega)$	isotropic, ordinary, and extraordinary dielectric functions
ε_{∞}	High-frequency dielectric constant
ε_0	Vacuum dielectric constant
$\varepsilon_1(\omega)$, and $\varepsilon_2(\omega)$	real and imaginary, respectively, parts of the dielectric function
ε_{r}	relative dielectric constant
$\epsilon_{\parallel}$, and $\epsilon_{\perp}$	Deformations in [0001] and perpendicular to it directions, respectively
Θ	Step function
$\kappa(\omega)$	Extinction coefficient
λ	Wavelength
$\rho_{\mathrm{cv}}(\omega)$	combined density of states
φ	Angle of incidence (for ellipsometry measurements)
χ_e	Electric susceptibility
Ψ	Ellipsometric parameter, azimuth angle
ω	angular frequency of the electromagnetic wave
ω_{LO}	Eigen-frequency of the LO mode
ω_{p}	Plasma frequency
ω_{TO}	Eigen-frequency of the TO Mode
A_0	Amplitude of the vector potential
a	lattice parameter
b	Band-gap bowing parameter
C_{ij}	Elasticity coefficient
c	lattice parameter parallel to [0001] direction
c_0	speed of light in vacuum
$\mathbf{D}$	Electric displacement field
$D(E)$	Density of states
D_i	Deformation potencial
d	Thilm thickness
$\mathbf{E}$	Electric field
E_{F}	Fermi level
$E_{\mathrm{F}}(k_{\mathrm{F}})$	Fermi energy at Fermi wavevector
E_n	Energy of the nth state

E_0	Fundamental band gap
E_{ren}	Renormalized band gap
e	elementary charge
$f(E_{\mathrm{c}})$	Fermi-Dirac distribution function
$f_{i,\beta}$	Relative oscillator strength
ω	Photon energy
$\hbar$	Reduced Planck constant
$\mathbf{k}$	Wave vector
k_{B}	Boltzmann constant
k_{F}	Fermi wave vector
M	Impulse matrix element between CB and VB Bloch functions
m_e^* and m_h^*	effective mass of electron and hole, respectively
N_{e}	Electron concentration
$\bar{N}(\omega)$	Complex refractive index
$n(\omega)$	Real refractive index
$\mathbf{P}$	Electric polarization field
R	Reflectivity
R_y, R_y^*	Rydberg energy, effektive Rydberg energy
T	Temperature

1 Introduction

Since the revision of the indium nitride (InN) band gap in the years 2002-2003 [11, 12], this material and its related alloys have attracted a lot of attention of scientific community. A wurtzite InN with its narrow fundamental band gap of 0.675 eV [13] and high electron mobility [14] is considered as a promising material for the applications in the near-infrared opto-electronic and high-speed electronic devices, sensors as well as terahertz emission [15–23].

The ternary InGaN alloys are already widely used in the commercial devices such as LDs and LEDs (used for TV, LCD monitor and mobile display back-lighting and solid state lighting applications). The band gap of the InGaN alloys can be tuned from 0.675 eV [13] to 3.435 eV [24] at room temperature. Due to this wide spectral range covering almost the whole solar spectrum, the InGaN system is a promising candidate for high-efficiency multi-junction solar cells applications [25–29].

The ternary AlInN alloys with band gaps at room temperature ranging from 0.675 eV [13] to 6.03 eV [30] are promising materials to improve the performance of optoelectronic and electronic devices. The $Al_{1-x}In_xN$ has its unique property that it is lattice-matched (LM) to GaN with x=17-18%, i.e., this allows to grow high quality stress-free AlInN epilayer on the GaN. The AlInN/GaN heterostructures are employed for high-electron-mobility transistors (HEMTs) fabrication used for high-frequency and high-power microwave applications [31–33]. High-quality distributed Bragg reflectors dedicated for vertical-cavity surface-emitting lasers can also be produced by using LM AlInN and GaN [34, 35]. Recently, Tong *et al* demonstrated promising thermoelectric properties of AlInN material [36].

The quaternary AlInGaN alloys (QNAs) offer a couple of advantages for the development of advanced devices such as blue-green and blue-violet laser diodes (LDs) [37–39], UV-LDs [40], UV/DUV light-emitting diodes (LEDs) [41–48], photodetectors [49, 50], and high-electron mobility transistors (HEMTs) [51–53]. Lee *et al* [54] applied a quaternary AlInGaN as a protective layer to suppress a thermal damage of InGaN multiple quantum layers. QNAs with an appropriate composition ratio can be grown lattice-matched to GaN, i.e., this enables a reduction of strain-induced defects and piezoelectric polarisation related built-in electric fields. Additionally, QNAs allow to adjust the band gap and the strain state independently. Moreover, quaternary alloys containing an indium have a strongly enhanced photoluminescence intensity in comparison with AlGaN alloys [55, 56]. The incorporation of indium allows to tune a lattice parameter, band gap, and thermal conductivity. Recently, Wang *et al* [57] have demonstrated that AlInGaN used as a quantum barrier for UV LEDs can significantly reduce the efficiency droop at high injection currents.

A lot of research studies have been devoted on the InN material and related alloys. However, the carbon doping in the InN material, the band gap as a function of alloy composition, strain influence on the band gap and optical constants for the In-related alloys still remain open questions. For example, according to the recent published results (of the Year 2010), the estimated AlInN alloy band-gap bowing parameter values varies in the broad range from 3.4 eV [58] up to 10.3 eV [59].

A software-based modelling allows precisely simulate device operation and reduce R&D costs. Therefore, the determination of the complex dielectric function (DF) $\bar{\varepsilon} = \varepsilon_1 + i\varepsilon_2$ (or optical constants $\bar{N} = n + ik = \sqrt{\bar{\varepsilon}}$) and precise band-gap bowing parameters are needed for the In-related alloys.

The aims of this work are:

- To investigate the optical properties of unintentionally doped InN films grown on Si(111) substrates;
- To investigate the optical properties of carbon doped InN samples;
- To determine the DFs (or optical constants) for the In-related alloys;
- To obtain an analytical representation of the DF for the In-related alloys;
- To estimate the band-gaps and high-energy inter-band transitions for the In-related alloys by applying the analytical DF model;
- To calculate a strain influence on the band gap by using the $\mathbf{k}\cdot\mathbf{p}$ method;
- To determine a strain-free band gap and high-energy inter-band transitions bowing parameters for the ternary InGaN and AlInN alloys;
- To develop an empirical expression that allows to determine the band gap and high-energy inter-band transitions for the quaternary AlInGaN alloy.

The introduction to the band structure will be provided in Chapter 2. The DF and its analytical models are discussed in Chapter 3. The spectroscopic ellipsometry will be introduced in Chapter 4. The epitaxial growth techniques used to grow the investigated samples will be described in Chapter 5. A comprehensive determination of optical properties for unintentionally and carbon doped InN films will be presented in Chapter 6. The results obtained for Ga-rich InGaN alloys are reported in Chapter 7. In Chapter 8, the Al-rich AlInN samples are investigated. Finally, the optical properties of quaternary AlInGaN alloys will be discussed in Chapter 9.

2 Band structure

Theoretical calculations of the electronic structures are usually based on the density functional theory (DFT). The DFT calculations with local density approximation (LDA) taking into account In 4*d* valence electrons give the negative band-gap for wurtzite structure InN [60, 61]. This effect is caused by an overestimation of the *p*-*d* repulsion between *p* valence states and shallow *d* core states. In order to get a positive band gap, a method is proposed to freeze the In 4*d* electrons in the core and use a construction of pseudo-potentials and self-energy corrections (SIC) [62, 63].

Recently, de Carvalho *et al* [64] applied an AM05 exchange-correlation (XC) functional to calculate the band structure of the wurtzite InN and its structural and electronic parameters. Figure 2.1 shows the calculated band structure and the density of states for the wurtzite InN. The calculated lattice parameters yielded a_0=3.549 Å and c_0=5.736 Å that are close to the experimental values 3.53774 Å and 5.70374 Å, respectively, as obtained from the work of Paszkowicz *et al* [65]. The fundamental band

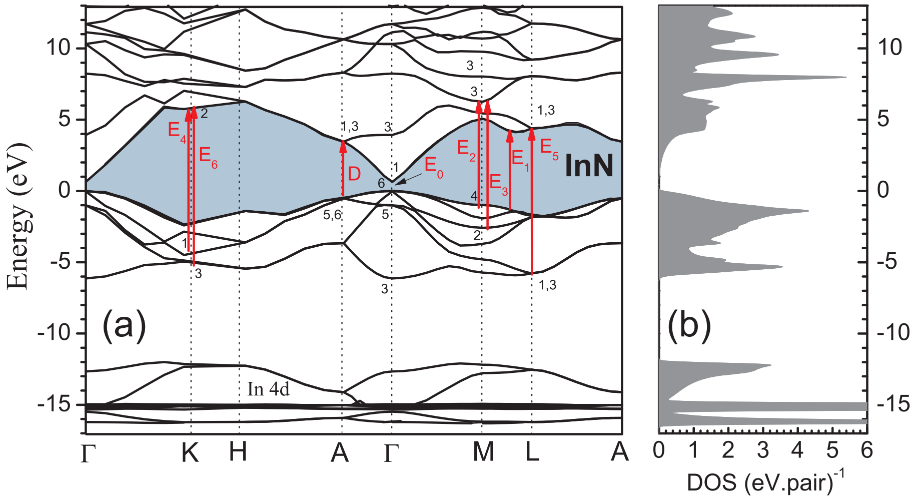

Figure 2.1: Quasi-particle band structure for wurtzite InN calculated using DFT with AM05 exchange-correlation functional without spin-orbit interaction [64]. Vertical arrows indicate the inter-band transitions allowed for a configuration $\mathbf{E}\perp\mathbf{c}$. Courtesy of L. C. de Carvalho.

gap of wurtzite InN was calculated to be 0.638 eV that is close to the experimentally determined value of 0.64 [12]. The vertical arrows in Fig. 2.1 indicate the inter-band transitions allowed for a configuration $\mathbf{E}\perp\mathbf{c}$ (will be discussed in Chapter 3).

Wurtzite structure III-V nitride semiconductors are direct band gap materials. The conduction band minimum (CBM) and the valence band maximum (VBM) are in the center of the BZ at the Γ point. The Bloch wave function of the conduction band (CB) and the valence band (VB) are described by *s*-states and *p*-states, respectively. In the wurtzite structure semiconductors a crystal-field splitting appears owing to the structural anisotropy. Due to a crystal-field splitting (Δ_{cf}) and spin-orbit (Δ_{so}) interaction, the VB is splitted into one Γ_9^{v} and two-fold degenerate Γ_7^{v} VBs. The spin-orbit and crystal-field energies for GaN [66] amount to 18.9 meV and 9.2 meV, respectively. For an InN, values of Δ_{so}=13 meV [67] and Δ_{cf}=19 meV explain the splitting between the ordinary and extraordinary absorption edge, as it was measured by ellipsometry [7, 68]. In contrast to the two latter binaries, an AlN [30] exhibits a large negative crystal-field splitting energy of -212 meV, while the spin-orbit energy of 16 meV is only slightly larger than for an InN and a GaN. According to the quasi-cubic model [69], the energetic position of the bands is given by

$$\Gamma_7^{\mathrm{c}} = \Delta_{\mathrm{cf}} + \frac{\Delta_{\mathrm{so}}}{3} + E_{\mathrm{A}}, \tag{2.1}$$

$$\Gamma_9^{\mathrm{v}} = \Delta_{\mathrm{cf}} + \frac{\Delta_{\mathrm{so}}}{3}, \tag{2.2}$$

$$\Gamma_{7+}^{\mathrm{v}} = \frac{\Delta_{\mathrm{cf}}}{2} - \frac{\Delta_{\mathrm{so}}}{6} + \frac{1}{2}\sqrt{(\Delta_{\mathrm{cf}} + \Delta_{\mathrm{so}})^2 - \frac{8}{3}\Delta_{\mathrm{cf}}\Delta_{\mathrm{so}}}, \tag{2.3}$$

$$\Gamma_{7-}^{\mathrm{v}} = \frac{\Delta_{\mathrm{cf}}}{2} - \frac{\Delta_{\mathrm{so}}}{6} - \frac{1}{2}\sqrt{(\Delta_{\mathrm{cf}} + \Delta_{\mathrm{so}})^2 - \frac{8}{3}\Delta_{\mathrm{cf}}\Delta_{\mathrm{so}}}. \tag{2.4}$$

The energy difference $\Gamma_7^{\mathrm{c}} - \Gamma_9^{\mathrm{v}} = E_{\mathrm{A}}$ for strain-free material is always used as a reference point for the analysis of inter-band absorption. The relative VB ordering as a function of the crystal-field splitting energy and Δ_{so}=13 meV is shown in Fig. 2.2. One can notice that the VB crossing occurs at $\Delta_{\mathrm{cf}} = 0$ meV and for an AlN the topmost valence band is Γ_{7+}^{v}, while for an InN and a GaN the topmost VB is Γ_9^{v}. By using the $\mathbf{k}\cdot\mathbf{p}$ method developed by Chuang and Chang [70], it is possible to calculate a band structure near the Γ point. At k=0 the VB and CB Hamiltonians are described separately if the band gap is large and the the interaction between VB and CB Hamiltonians can be neglected. The CB Hamiltonian is described by 2×2 matrix:

$$H_{\mathrm{cc}} = \begin{bmatrix} E_c & 0 \\ 0 & E_c \end{bmatrix} . \tag{2.5}$$

While the VB Hamiltonian is described by 6×6 matrix:

$$H_{\mathrm{vv}} = \begin{bmatrix} F & -K^* & -H^* & 0 & 0 & 0 \\ -K & G & H & 0 & 0 & \Delta \\ -H & H^* & \lambda & 0 & \Delta & 0 \\ 0 & 0 & 0 & F & -K & H \\ 0 & 0 & \Delta & -K^* & G & -H^* \\ 0 & \Delta & 0 & H^* & -H & \lambda \end{bmatrix} . \tag{2.6}$$

The Hamiltonian elements are determined as follows:

$$\begin{aligned} E_c &= E_g + \Delta_1 + \Delta_2 + \frac{\hbar^2 k_z^2}{2m_{e,\|}} + \frac{\hbar^2 (k_x^2 + k_y^2)}{2m_{e,\perp}} + \alpha_{cz}\epsilon_{zz} + \alpha_{ct}(\epsilon_{xx} + \epsilon_{yy}), \qquad (2.7) \\ F &= \Delta_1 + \Delta_2 + \lambda + \theta, \\ G &= \Delta_1 - \Delta_2 + \lambda + \theta, \\ K &= \frac{\hbar^2}{2m_0} A_5 (k_x + ik_y)^2 + D_5(\epsilon_{xx} + 2i\epsilon_{xy} - \epsilon_{yy}), \\ H &= \frac{\hbar^2}{2m_0} A_6 k_z (k_x + ik_y) + D_6(\epsilon_{zx} + i\epsilon_{yz}), \\ \lambda &= \frac{\hbar^2}{2m_0} \left[A_1 k_z^2 + A_2 k_t^2\right] + D_1\epsilon_{zz} + D_2(\epsilon_{xx} + \epsilon_{yy}), \\ \theta &= \frac{\hbar^2}{2m_0} \left[A_3 k_z^2 + A_4 k_t^2\right] + D_3\epsilon_{zz} + D_4(\epsilon_{xx} + \epsilon_{yy}), \\ \Delta &= \sqrt{2}\Delta_3. \end{aligned}$$

where, E_g is a band gap of the material. The Δ_1, Δ_2 and Δ_3 are related to the spin-orbit and crystal-field splitting energies. The parameters D_i and α_i correspond to the deformation potentials for the VB and CB, respectvely. The effective masses parallel and perpendicular to the c-axis are indicated as $m_{e,\|}$ and $m_{e,\perp}$, respectively. The parameters A_j define the contribution of the remote bands. In the quasi-cubic approximation: $\Delta_1 = \Delta_{\mathrm{cf}}$ and $\Delta_2 = \Delta_3 = \Delta_{\mathrm{so}}/3$, D_3=D_2-D_1, D_4=-$D_3/2$, $\Delta_2 = \Delta_3$.

Table 2.1: Parameters used in **k**·**p** calculations for InN, GaN, and AlN at RT.

Parameter	InN	GaN	AlN
E_A (eV)	0.675 [13]	3.435 [24]	6.24 [30]
E_B (eV)	-	-	6.03 [30]
Δ_cf (meV)	19 [68]	9.2 [67]	-212 [30]
Δ_so (meV)	13 [67]	18.9 [67]	16 [30]
α (eV)	-7.2 [75]	-44.5 [71]	-20.5 [75]
D_1 (eV)	-3.7 [76]	-41.4 [71]	-17.1 [76]
D_2 (eV)	4.5 [76]	-33.3 [71]	-8.7 [76]
D_5 (eV)	-4 [76]	-4.7 [71]	-3.4 [76]
a_0 (Å)	3.53774 [65]	3.1894 [74]	3.112 [74]
C_{13} (GPa)	92 [76]	114 [72]	108 [76]
C_{33} (GPa)	224 [76]	381 [72]	373 [76]

For a GaN, the following deformation-potential parameter values are employed: $\alpha_\perp = \alpha_\| = \alpha = -44.5$ eV, D_1=-41.4 eV, D_2=-33.3 eV, and D_5=-4.7 eV [71]. The stiffness constants C_{13}=114 GPa and C_{33}=381 GPa are taken from Ref. 72. For an InN (AlN), the deformation potentials α=-7.2 eV (-20.5 eV), D_1=-3.7 eV (-17.1 eV), D_2=4.5 eV (-8.7 eV), and D_5=-4.0 eV (-3.4 eV) as well as the stiffness constants C_{13}=92 GPa (108 GPa) and C_{33}=224 GPa (373 GPa) were used from Ref. 73. The strain-free lattice constants of a_0^{InN}=3.5377 [65], a_0^{GaN}=3.1894 [74], and a_0^{AlN}=3.112 [74] for an InN, a GaN, and an AlN, respectively, were employed. For clarity, the used parameters are summarized in Table 2.1. The in-plane strain is described by using the following equation:

$$\epsilon_{xx} = \epsilon_{yy} = \frac{a - a_0}{a_0}, \tag{2.8}$$

while the out-of-plane strain is described by

$$\epsilon_{zz} = \frac{c - c_0}{c_0} = -\frac{2C_{13}}{C_{33}}\ \epsilon_{xx}\ , \tag{2.9}$$

where a_0 (c_0) and a (c) are the lattice parameters for a strain-free and strained material, respectively. From the **k**·**p** calculations it is possible to estimate the strain induced band-gap shift and relative oscillator strengths for the transitions A ($\Gamma_9^\mathrm{v} \rightarrow \Gamma_7^\mathrm{c}$), B ($\Gamma_{7+}^\mathrm{v} \rightarrow \Gamma_7^\mathrm{c}$) and C ($\Gamma_{7-}^\mathrm{v} \rightarrow \Gamma_7^\mathrm{c}$). Figure 2.3(a) and (b) show the calculated relative oscillator strength as a function of crystal-field splitting energy for the configuration $\boldsymbol{E}\perp\boldsymbol{c}$ and configuration $\boldsymbol{E}\|\boldsymbol{c}$, respectively.

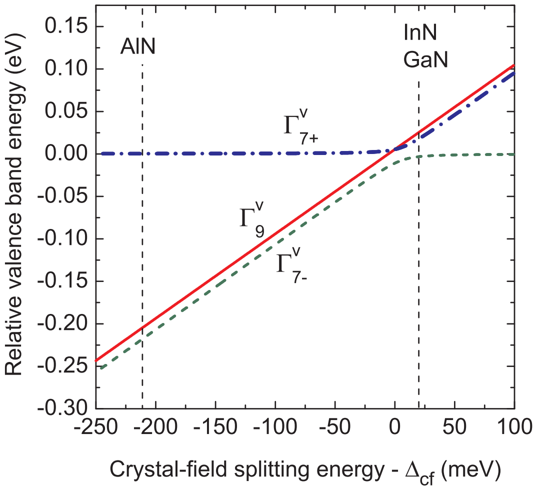

Figure 2.2: The relative VB energy as a function of crystal-field splitting energy. Δ_{so} is fixed to 13 meV.

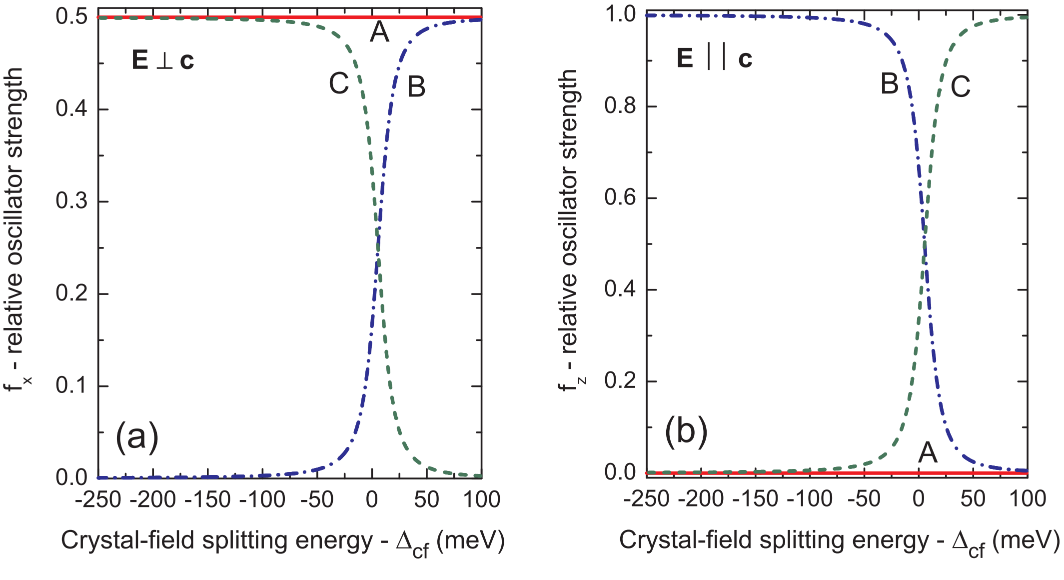

Figure 2.3: Relative oscillator strength for configuration $\boldsymbol{E}\perp\boldsymbol{c}$ (a) and configuration $\boldsymbol{E}\|\boldsymbol{c}$ (b) as a function of crystal-field splitting energy.

3 Dielectric function

3.1 Introduction to the dielectric function

The dielectric function (DF) describes the linear response of a material to the electromagnetic wave. The important information is obtained about semiconductor electronic properties from the optical spectrum. The DF is a complex function consisting of the real and imaginary parts. The imaginary part represents the absorption of the material, while the real part describes how strong the material is polarized.

The electric field induces the dipole moments in the dielectric material, which are described by the electric polarization **P**. The electric displacement **D** is related to the electric field vector **E** via the following expression:

$$\mathbf{D} = \varepsilon_0 \mathbf{E} + \mathbf{P}, \tag{3.1}$$

where ε_0 is a vacuum permittivity. Employing the following equations

$$\mathbf{P} = \varepsilon_0 \chi_e \mathbf{E}, \tag{3.2}$$

$$\varepsilon_r = 1 + \chi_e, \tag{3.3}$$

where ε_r is a relative permittivity and χ_e is an electric susceptibility, the Eq. 3.1 can be re-written as

$$\mathbf{D} = \varepsilon_0 \varepsilon_r \mathbf{E} = \overset{\leftrightarrow}{\varepsilon} \mathbf{E}. \tag{3.4}$$

The **D** and **E** are related through the dielectric tensor $\overset{\leftrightarrow}{\varepsilon}(\omega)$. For isotropic material (space group $F4_3m(T_d^2)$) the dielectric tensors are equal in all directions. The strain-free hexagonal group-III-nitride material (space group $\mathrm{P}6_3mc(C_{6\mathrm{v}}^4)$) are optically uniaxial materials. The optical axis is parallel to a crystallographic c-axis and perpendicular to x-y plane. For uniaxial crystals a light velocity varies depending on a propagation direction. This phenomenon is called birefringence. The dielectric tensor is described in the following form:

$$\overleftrightarrow{\varepsilon} = \begin{pmatrix} \bar{\varepsilon}_x & 0 & 0 \\ 0 & \bar{\varepsilon}_y & 0 \\ 0 & 0 & \bar{\varepsilon}_z \end{pmatrix} = \begin{pmatrix} \bar{\varepsilon}_\mathrm{o} & 0 & 0 \\ 0 & \bar{\varepsilon}_\mathrm{o} & 0 \\ 0 & 0 & \bar{\varepsilon}_\mathrm{e} \end{pmatrix} . \tag{3.5}$$

The $\bar{\varepsilon}_\mathrm{o}$ and $\bar{\varepsilon}_\mathrm{e}$ correspond to the ordinary and extraordinary components of the dielectric tensor that describe the material's interaction with an electromagnetic wave having an electric field vector configurations $\boldsymbol{E} \perp \boldsymbol{c}$ and $\boldsymbol{E} \parallel \boldsymbol{c}$, respectively. Both components are complex and depend on a photon energy. The optical properties of a semiconductor (i.e., the description of a material's and an electromagnetic wave's interaction) is described by a complex DF. The DF $\bar{\varepsilon}_j(\omega)$ with its real $(\varepsilon_{1,j}(\omega))$ and imaginary $(\varepsilon_{2,j}(\omega))$ part is given by

$$\bar{\varepsilon}_j(\omega) = \varepsilon_{1,j}(\omega) + i\varepsilon_{2,j}(\omega); \quad (j = \mathrm{o},\ \mathrm{e}). \tag{3.6}$$

The real part and imaginary part of the DF are related through Kramers-Kronig relation:

$$\varepsilon_{1,j}(\omega) = 1 + \frac{2}{\pi}\mathcal{P}\int\limits_0^{+\infty} \frac{\omega' \cdot \varepsilon_{2,j}(\omega')}{\omega'^2 - \omega^2} d\omega' \ , \tag{3.7}$$

$$\varepsilon_{2,j}(\omega) = -\frac{2\omega}{\pi}\mathcal{P}\int\limits_0^{+\infty} \frac{\varepsilon_{1,j}(\omega')}{\omega'^2 - \omega^2} d\omega' \ , \tag{3.8}$$

where $\mathcal{P}$ is Cauchy integral's main value. The complex DF and complex optical constants for non magnetic material are related through the following expressions:

$$\bar{N}_j(\omega) = n_j(\omega) + i\kappa_j(\omega) = \sqrt{\bar{\varepsilon}_j(\omega)}, \tag{3.9}$$

$$\varepsilon_{1,j}(\omega) = n_j^2(\omega) - \kappa_j^2(\omega), \tag{3.10}$$

and

$$\varepsilon_{2,j}(\omega) = 2n_j(\omega)\kappa_j(\omega), \tag{3.11}$$

with n_j and κ_j corresponding to the real and imaginary part, respectively, of the complex refraction index $\bar{N}_j$.

Spectroscopic ellipsometry (described in Chapter 4) is a common technique to determine a sample's complex DF. The spectroscopic ellipsometer measures an optical response under a certain angle of incidence and the obtained ellipsometric parameters Ψ and Δ reflect mainly the spectral dependence of the ordinary DF for the (0001)-oriented films. The deviations around the band gap are only found if the material exhibits sharp excitonic resonances for both polarization directions [77, 78]. Further, in this work, the DF determined from the (0001)-oriented samples will be called an *isotropic* DF. In the non-polar sample case, the c-axis is on the surface plane. Therefore, by measuring the sample by ellipsometry at two different configurations (i.e., the c-axis perpendicular to the plane of incidence and c-axis parallel to the plane of incidence), both *ordinary* and *extraordinary* DFs can be extracted. For comparison, Figure 3.1 shows the isotropic (solid black line), ordinary (dashed black line), and extraordinary (dashed dotted red line) imaginary parts of the DF obtained for the wurtzite structure InN. It is observed that the isotropic DF is close to the ordinary DF, i.e., the energetic positions of characteristic features (peaks and shoulders) of the ε_2 are at the same energetic positions.

An absorption coefficient $\alpha_j(\omega)$ is related to the imaginary part of the DF through an expression:

$$\alpha_j(\omega) = \frac{\omega}{n_j(\omega)c_0}\varepsilon_{2,j}(\omega) \ . \tag{3.12}$$

It is important to emphasize that $\alpha_j(\omega)$ depends not only on the imaginary part of the DF - $\varepsilon_{2,j}(\omega)$, but also on the refractive index $n_j(\omega)$ that is not a constant. Therefore, by extrapolating a linear region of the squared absorption coefficient, one must take a refractive index into consideration. An absorption of the photon with an energy $\hbar\omega \geq E_0$

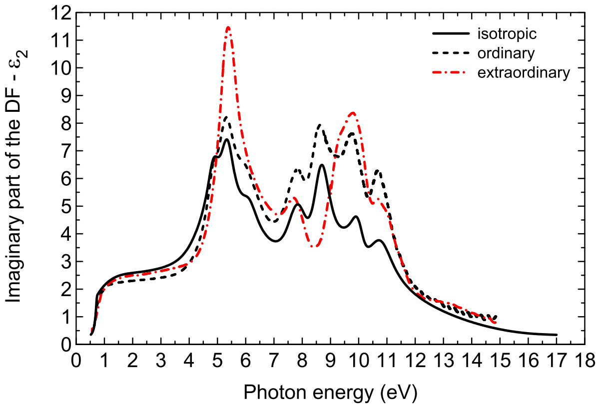

Figure 3.1: Experimental isotropic (black solid line), ordinary (black dashed line), and extraordinary (red dashed-dotted line) imaginary part of the DF for the wurtzite InN.

causes the electron transition from the VB to the CB. Disregarding in the first step the electron-hole interaction (exciton effects), the transition probability is described as

$$W_j(\omega) = \frac{1}{V}\frac{2\pi}{\hbar}\left(\frac{eA_0}{2m_0}\right)^2 \sum_{\mathbf{k}_\mathrm{c},\mathbf{k}_\mathrm{v}} |\mathbf{e}\mathbf{P}_{\mathrm{vc},j}|^2 \delta(E_\mathrm{c}(\mathbf{k}) - E_\mathrm{v}(\mathbf{k}) - \hbar\omega), \tag{3.13}$$

where A_0 is a vector potential amplitude, V is a volume of the unit cell, m_0 is an electron mass and e is an elementary charge. The optical anisotropy will be determined by the direction dependent momentum matrix element $|\mathbf{e}\mathbf{P}_{\mathrm{vc},j}|^2$ [79], which connects the VB and CB Bloch states. The absorption coefficient $\alpha_j(\omega)$ is related to $W_j(\omega)$ via the following expression:

$$\alpha_j(\omega) = \frac{2\hbar}{\varepsilon_0 c_0 n_j \omega A_0^2} W_j(\omega). \tag{3.14}$$

The impulse of a photon is very small in comparison with a wave vector $\mathbf{k}$ within the first BZ. Therefore, it is assumed that a transition takes place in a vertical direction ($\mathbf{k}_\mathrm{v} = \mathbf{k}_\mathrm{c}$). A sum of all $\mathbf{k}_\mathrm{v}$ and $\mathbf{k}_\mathrm{c}$ can be replaced by the integration over all $\mathbf{k}$-vectors in the first BZ. Then, the imaginary part of the DF can be expressed as

$$\varepsilon_{2,j}(\omega) = \frac{\pi e^2}{\varepsilon_0 \omega^2 m_0^2} |\mathbf{e}\mathbf{P}_{\mathrm{vc},j}|^2 \frac{2}{8\pi^3} \int\limits_{BZ} \delta(E_\mathrm{c}(\mathbf{k}) - E_\mathrm{v}(\mathbf{k}) - \hbar\omega) d^3k \ . \tag{3.15}$$

Here, the joint density of states (JDOS) $\rho_\mathrm{cv}(\omega)$ is introduced

$$\begin{aligned} \rho_\mathrm{cv}(\omega) &= \frac{2}{8\pi^3} \int\limits_{BZ} \delta(E_\mathrm{c}(\mathbf{k}) - E_\mathrm{v}(\mathbf{k}) - \hbar\omega) d^3k \\ &= \frac{2}{8\pi^3} \int\limits_{E=E_\mathrm{c}-E_\mathrm{v}=konst} \frac{dS}{|\nabla_\mathbf{k}(E_\mathrm{c}(\mathbf{k}) - E_\mathrm{v}(\mathbf{k}))|} \ , \end{aligned} \tag{3.16}$$

where the integration over all $\mathbf{k}$-vectors in the first BZ also over constant energies takes place. From Eq. 3.16 it is evident that JDOS depend on the CB and VB alignment. The density of states possesses the singularities at points where $|\nabla_\mathbf{k}(E_\mathrm{c}(\mathbf{k}) - E_\mathrm{v}(\mathbf{k}))|$ vanishes. These points are called the critical points (CPs) of the band structure and the corresponding singularities in the JDOS are called van Hove singularities [80]. The peaks and shoulders in the imaginary part of the DF are attributed to van Hove singularities.

However, according to the recent state-of-the-art many body *ab initio* calculations from the work of Riefer *et al* [81], the JDOS is not necessarily large at a critical point. For example, the JDOS is zero at M_0 point that indicates the absorption onset and rises proportionally to the square root of the energy for parabolic bands. Some peaks in the imaginary part of the DF can be assigned to bound excitonic states at M_0 or M_1 critical points [81]. It is known that the shape of imaginary part of the DF (ε_2) is influenced by the electron-hole interaction. Already in 1957, Elliott developed a method for the analysis of the Wannier excitons [82]. Due to Coulomb attraction of electrons and holes, the hydrogen-like states are formed below a single-particle gap. The energies of the hydrogen states are discrete and depend on the effective Rydberg constant

$$R_y^* = \frac{\mu e^4}{2(4\pi\varepsilon_0\varepsilon_r\hbar)^2}, \tag{3.17}$$

where $\mu = (m_e^{-1} + m_h^{-1})^{-1}$ with m_e and m_h electron and hole masses, respectively. However, in order to prove if the Coulomb interaction makes an influence in the high-energy range, the theoretical studies, which includes the Coulomb correlated electron-hole pairs, are needed. The theoretical calculations of the DF for InN and AlN from the works of Furthmüller *et al* [62] and Riefer *et al* [81], respectively, have shown that excitonic effects make influence to the DF at high energy range. Figure 3.2 compares the InN experimental imaginary part of the isotropic DF (that is close to the ordinary DF) and the the calculated ordinary imaginary part of the DF with excitonic effects (red dashed curve) and without excitonic effects (blue dotted curve) from the work of Furthmüller *et al* [62]. There is a clear tendency for a redistribution of peaks to lower photon energies due to the Coulomb attraction and the peak positions are very close

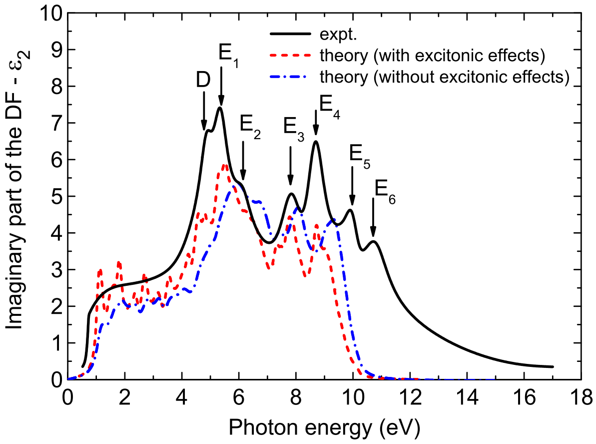

Figure 3.2: Experimental isotropic imaginary DF for the wurtzite InN in comparison with calculated ordinary DFs [62]: with included excitonic effects (red dashed line) and without excitonic effects (blue dashed dotted line).

Table 3.1: InN high-energy inter-band transitions allowed for a configuration $\mathbf{E}\perp\mathbf{c}$. Courtesy of L. C. de Carvalho.

Transition notation	corresponding points in the Brillouin zone
D	$\mathrm{A}^{\mathrm{v}}_{5,6} \longrightarrow \mathrm{A}^{\mathrm{c}}_{1,3}$
E_1	$\mathrm{U}^{\mathrm{v}}_{1} \longrightarrow \mathrm{U}^{\mathrm{c}}_{4}$
E_2	$\mathrm{M}^{\mathrm{v}}_{4} \longrightarrow \mathrm{M}^{\mathrm{c}}_{3}$
E_3	$\mathrm{M}^{\mathrm{v}}_{2} \longrightarrow \mathrm{M}^{\mathrm{c}}_{3}$
E_4	$\mathrm{K}^{\mathrm{v}}_{1} \longrightarrow \mathrm{K}^{\mathrm{c}}_{2}$
E_5	$\mathrm{L}^{\mathrm{v}}_{1,3} \longrightarrow \mathrm{L}^{\mathrm{c}}_{1,3}$
E_6	$\mathrm{K}^{\mathrm{v}}_{3} \longrightarrow \mathrm{K}^{\mathrm{c}}_{2}$

to the positions of the experimental DF, as it can be observed, as it can be observed in Fig.3.2. The CPs of the band structure D, E_1, E_2, E_3, E_4, E_5, and E_6 are denoted by arrows in Fig. 3.2 and their corresponding inter-band transitions allowed for the configuration $\mathbf{E}\perp\mathbf{c}$ are indicated in Fig. 2.1 (see previous Chapter). In addition, the transitions D, E_1, E_2, E_3, E_4, E_5, and E_6 with the corresponding points in the Brillouin zone are summarized in Table 3.1.

3.2 Analytical representation of the dielectric function

In this section, two analytical models will be described. The first model based on the parametric oscillators allows to present the DF in the wide spectral photon energy. This model was developed by Goldhahn *et al* [83] based on the experimental data for a GaN [84], and an AlN [83] from 1 up to 9.5 eV. It completely reproduces all peculiarities of the DFs, i.e., the contributions from the free excitonic transitions and the excitonic continuum around the band gap as well as the pronounced features due to the high-energy critical points. In Chapters 8-9 it will be demonstrated that the model is also suitable to describe the DFs of ternary and quaternary In-related alloys. The second simplified model developed by Shokhovets *et al* [85], allows to describe the dispersion below the band gap and extract the high-frequency dielectric constant. Accurate analytical form of the DF is necessary for device modelling and analysis of the material optical properties.

3.2.1 Analytical representation in the wide spectral range

The imaginary part of the DF can be separated in two parts:

$$\varepsilon_2 = \varepsilon_{2,\mathrm{low}} + \varepsilon_{2,\mathrm{high}}, \tag{3.18}$$

where the term $\varepsilon_{2,\mathrm{low}}$ describes ε_2 in the band gap region and the second term $\varepsilon_{2,high}$ - in the higher energy range. They are expressed as follows:

$$\begin{aligned}\varepsilon_{2,\mathrm{low}} &= \sum_{\mathrm{j=A,B,C}} \frac{A_{\mathrm{BS}}\hbar\omega\Gamma_{\mathrm{BS}}}{((E_{\mathrm{j}}-R)^2-\hbar^2\omega^2)^2+(\hbar\omega\Gamma_{\mathrm{BS}})^2} \\ &+ \sum_{\mathrm{j=A,B,C}} \frac{A_{\mathrm{CS}}}{\hbar\omega}\frac{1+\mathrm{erf}[(\hbar\omega-E_{\mathrm{j}})/\Gamma_{\mathrm{CS}}]}{1-\exp(-2\pi\sqrt{R/|\hbar\omega-E_{\mathrm{j}}|})};\end{aligned} \tag{3.19}$$

$$\begin{aligned}\varepsilon_{2,\mathrm{high}} &= \sum_{\mathrm{j=1,2,3}} \frac{A_{\mathrm{j}}\hbar\omega\Gamma_{\mathrm{j}}}{(E_{\mathrm{j}}^2-\hbar^2\omega^2)^2+(\hbar\omega\Gamma_{\mathrm{j}})^2}\times \\ &\times\left[\Theta(E_{\mathrm{j}}-\hbar\omega)\frac{\hbar\omega-E_{\mathrm{A}}}{E_{\mathrm{j}}-E_{\mathrm{A}}}+\Theta(\hbar\omega-E_{\mathrm{j}})\right].\end{aligned} \tag{3.20}$$

The real part of the damped harmonic oscillators (DHOs) in the first term of $\varepsilon_{2,\mathrm{low}}$ (Eq. 3.19) represents the bound exciton states below the band gap, while the exciton continuum is represented by the second term. DHOs with the Heaviside step function Θ in Eq. 3.20 describe the high-energy critical points (CPs). The real part of the DF is described by

$$\begin{aligned}\varepsilon_1 &= b+\sum_{\mathrm{j=A,B,C}}\left(\frac{A_{\mathrm{BS}}((E_{\mathrm{j}}-R)^2-\hbar^2\omega^2)}{((E_{\mathrm{j}}-R)^2-\hbar^2\omega^2)^2+(\hbar\omega\Gamma_{\mathrm{BS}})^2}\right) \\ &+\frac{1}{\pi}\Re\left(A_0\ln\frac{E_{\mathrm{P}}^2-(\hbar\omega+\mathrm{i}\Gamma_0)^2}{E_{\mathrm{A}}^2-(\hbar\omega+\mathrm{i}\Gamma_0)^2}\right) \\ &+\frac{1}{\pi}\Re\left(\frac{A_{\mathrm{P}}E_{\mathrm{P}}}{E_{\mathrm{P}}^2-(\hbar\omega+\mathrm{i}\Gamma_0)^2}\right) \\ &+\sum_{\mathrm{j=1,2,3}}\frac{A_{\mathrm{j}}(E_{\mathrm{j}}^2-\hbar^2\omega^2)}{(E_{\mathrm{j}}^2-\hbar^2\omega^2)^2+(\hbar\omega\Gamma_{\mathrm{j}})^2}.\end{aligned} \tag{3.21}$$

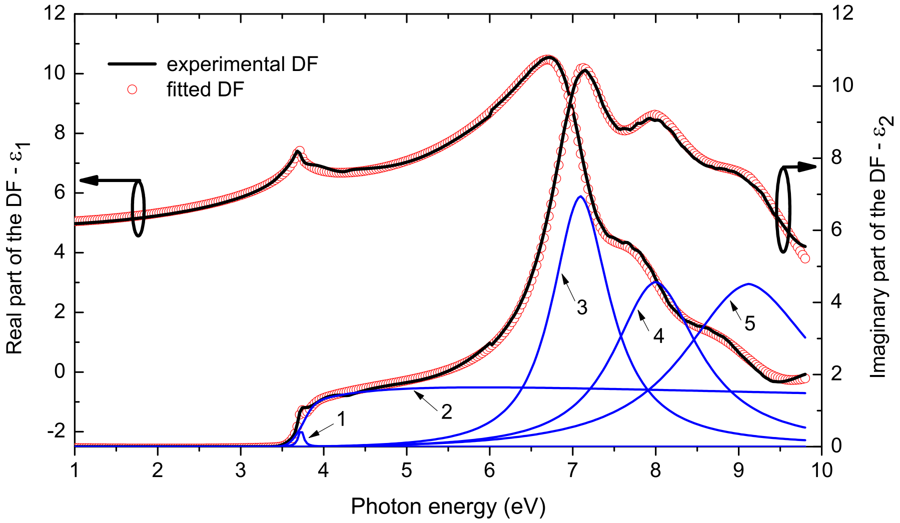

Figure 3.3: Experimental isotropic DF (black solid lines) and its analytical representation (red open circles) for the (0001)-oriented AlInGaN sample (Al 28% and In 4%). The blue lines represent the separate damped harmonic oscillators of the imaginary part of the DF as described by Eq. 3.18.

The bound excitonic states and high-energy CPs in Eq. 3.21 are represented by the DHOs, while the excitonic continuum is modeled by a logarithmic function and b is a constant term.

The analytical expressions (Eq. 3.18 and Eq. 3.21) are fitted simultaneously to the experimentally obtained real and imaginary parts of the DF using a least square method. The fit yields the transitions E_A or E_B and the high-energy inter-band transitions E_1, E_2, and E_3. For example, the experimental isotropic DF and its analytical form for the (0001)-oriented AlInGaN sample (with Al 28% and In 4% content) are represented in Fig. 3.3. The separate oscillators are shown with the blue solid lines in Fig. 3.3 for the imaginary part of the DF, as described by Eqs. 3.19-3.20. The harmonic oscillator 1 represents the bound exciton states below the band gap, while the harmonic oscillator 2 represents the excitonic continuum. The oscillators 3, 4 and 5 represent high-energy CPs.

It is important to emphasize that DF modelling permits to determine more accurately the band-gap energy. Many studies use linear interpolation of the squared absorption coefficient to determine the gap. As it is seen in Figure 3.3, the excitonic peak is appearing. A linear interpolation of the squared absorption coefficient allows to determine only the excitonic transition. With the knowledge that AlN exciton binding energy is ~55 meV [86], the interpolation of the squared absorption coefficient could lead to the band-gap estimation error of several tens of milli-electronvolts for Al-rich alloys.

3.2.2 Dispersion below the band gap and high-frequency dielectric constant

The dispersion of ε_1 in the transparent region (below the band gap) is expressed by the analytical expression developed by Shokhovets *et al* [85] and described as

$$\varepsilon_1(\hbar\omega) = 1 + \frac{2}{\pi}\left(\frac{A_G}{2}\ln\frac{E_H^2-(\hbar\omega)^2}{E_G^2-(\hbar\omega)^2} + \frac{A_H E_H}{E_H^2-(\hbar\omega)^2}\right), \tag{3.22}$$

where energies E_G and E_H denote an average band-gap and high-energy transitions, with their amplitudes A_G and A_H, respectively. The high-frequency dielectric constant (ε_∞) is obtained by fitting the experimentally determined ε_1 below the band gap with the analytical expression (3.22) and by extrapolating this expression to zero photon energy ($\hbar\omega \to 0$).

For example, Fig. 3.4 shows the experimental and modelled (by using Eq. 3.22) real part of the isotropic DF for the AlInGaN sample (Al 28% and In 4%).

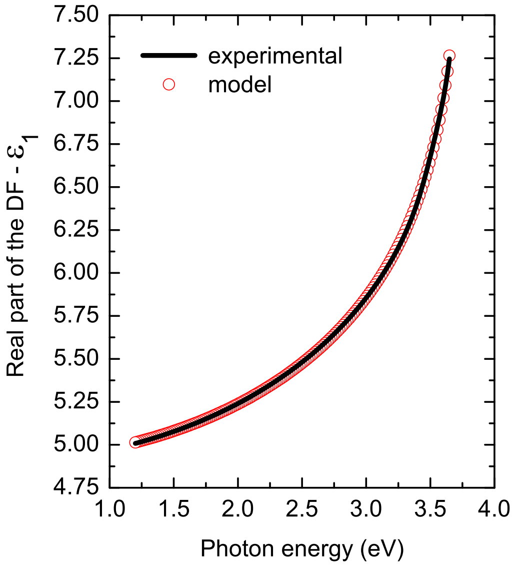

Figure 3.4: Experimental ε_1 (black solid lines) and its analytical representation (red open circles) in the transparent region (below the band gap) for the AlInGaN sample (Al 28% and In 4%).

3.3 Model for the mid-infrared range dielectric function

Due to the low Γ-point conduction band minimum that is significantly below the charge neutrality level, the InN material possesses a surface electron accumulation layer [87–93]. Therefore, the conventional Hall measurement estimates only an average carrier concentration (which is normally higher than a bulk carrier concentration).

However, the infrared spectroscopic ellipsometry (IR-SE) measurements allow to estimate accurately a carrier concentration. The electron concentration is obtained from the analysis of the mid-infrared DF. A plasmon-phonon coupling is observed in a mid-infrared range. The anisotropic DF for the materials with free carriers is described using the factorized model based on the anharmonic coupling effects between free-carrier plasmons and longitudinal-optical phonons [94]:

$$\bar{\varepsilon_j}(\omega) = \varepsilon_{\infty,j} \frac{\prod_{n=1}^{2} \left(\omega^2 + i\gamma_{\mathrm{LPP},nj}\omega - \omega^2_{\mathrm{LPP},nj}\right)}{(\omega^2 + i\gamma_{\mathrm{p},j}\omega)\left(\omega^2 + i\gamma_{\mathrm{TO},j}\omega - \omega^2_{\mathrm{TO},j}\right)} \,. \tag{3.23}$$

where $\omega_{\mathrm{LPP},nj}$ and $\gamma_{\mathrm{LPP},nj}$ is the frequency and broadening, respectively, of the n-th longitudinal-phonon-plasmon (LPP) mode. The parameter $\gamma_{\mathrm{p},j}$ is the plasma excitation broadening parameter. The frequency and the broadening of the TO phonons are denoted by $\omega_{\mathrm{TO},j}$ and $\gamma_{\mathrm{TO},j}$, respectively. The high-frequency dielectric constant is denoted as $\varepsilon_{\infty,j}$. The frequency $\omega_{\mathrm{LPP},nj}$ is related with TO phonon frequency $\omega_{\mathrm{TO},j}$ and the plasma frequency $\omega_{\mathrm{p},j}$ via the following expression:

$$\omega^2_{\mathrm{LPP},nj} = \frac{1}{2}\left[\omega^2_{\mathrm{LO},j} + \omega^2_{\mathrm{p},j} + (-1)^n \sqrt{(\omega^2_{\mathrm{LO},j} + \omega^2_{\mathrm{p},j})^2 - 4\omega^2_{\mathrm{p},j}\omega^2_{\mathrm{TO},j}}\right] . \tag{3.24}$$

From the model fit, the plasma frequency is obtained that is related to the carrier concentration through the following expression:

$$\omega^2_{p,j} = \frac{N_e e^2}{\varepsilon_0 \varepsilon_{\infty,j} m^*(N_e)} . \tag{3.25}$$

One can observe in Eq. 3.25 that only the ratio $N_e/m^*(N_e)$ can be determined. Thus, the problem must be solved self-consistently by analyzing the IR-SE data and the imaginary part of the DF (ε_2) around the band gap, as it will be demonstrated in Chapter 6.

4 Spectroscopic ellipsometry

A spectroscopic ellipsometer is a powerful characterization tool used at research laboratories as well as in microelectronics and solar industries. An ellipsometry measurement is dedicated to characterize thin films and bulk materials. A determination of materials' optical constants and layer thickness is the most common application of the spectroscopic ellipsometry. Accurate complex optical constants ($\bar{N}_j(\omega) = n_j(\omega) + i\kappa_j(\omega)$) or dielectric function ($\bar{\varepsilon}_j(\hbar\omega) = \varepsilon_{1,j}(\omega) + i\varepsilon_{2,j}(\omega)$) in the visible and ultraviolet (UV) regions are necessary for opto-electronic device design and modelling. Moreover, the ellipsometry data analysis provides the information concerning a surface (or interface) roughness, optical anisotropy, alloy composition, and crystallinity. The advanced ellipsometer with an integrated rotating compensator allows also to determine film thickness non-uniformity. An integrated *in-situ* ellipsometer in a molecular beam epitaxy or metalorganic vapour phase epitaxy reactor can also be used to determine the growth ratio of the epitaxial layers.

At the beginning of this chapter, the basics of spectroscopic ellipsometry will be introduced. Then, three types of spectroscopic ellipsometer setups, used for sample investigations, will be briefly described; starting with an infrared spectroscopic ellipsometer (IR-SE) covering the spectral range 300 - 2000 cm^{-1} (0.04 - 0.25 eV), a variable angle spectroscopic ellipsometer permitting to work in the photon energy range 0.56-6.4 eV and finishing with a synchrotron ellipsometer enabling to conduct measurements in the high-energy range 5-20 eV. At the end of this chapter, an ellipsometry data analysis is discussed.

4.1 Principles of ellipsometry

An ellipsometer uses a polarized light and measures its polarization state of the reflected (or transmitted, depending on the ellipsometer configuration) light. The experimental data are usually expressed in terms of the parameters Ψ and Δ that are related to a ratio of the Fresnel reflection coefficients. This ratio is a complex number and contains a *phase* information. This makes a measurement very sensible. Moreover, an ellipsometer measures the ratio of two values and makes a measurement very accurate. It is important to understand that ellipsometry does not measure sample parameters directly. Therefore, to estimate sample parameters (e.g., thilm thicknes or optical constants), it is necessary to solve an inverse problem by modelling the measured experimental data, as it will be discussed in section 4.5.

The electromagnetic plane wave is describe as

$$\mathbf{E}(\mathbf{r},\mathbf{t}) = \mathbf{E_0}\mathbf{e}^{\mathrm{i}(\mathbf{kr}-\omega\mathbf{t})}. \tag{4.1}$$

The plane wave can be divided in the two components perpendicular and parallel to the plane of incidence (POI). The perpendicular component is denoted as $\mathbf{E}_\mathrm{s}$ and the parallel component is denoted as $\mathbf{E}_\mathrm{p}$. A column vector describes both components:

$$\mathbf{E} = \begin{pmatrix} \bar{E}_\mathrm{p} \\ \bar{E}_\mathrm{s} \end{pmatrix}. \tag{4.2}$$

As it is depicted in Fig. 4.1, the linearly polarized light with a polarization angle χ (angle between the POI and electric field vector) shines a sample at the angle of incidence φ_0 and the polarization state of the reflected beam becomes in general case elliptically polarized, since the perpendicular and parallel components of the reflected light are not in phase. For example, Fig. 4.2(a) and (b) show the polarization states of the reflected linearly polarized light with polarization angles of 30° and 45°, respectively, and with different phase shift values Δ. The reflected and transmitted perpendicular and parallel

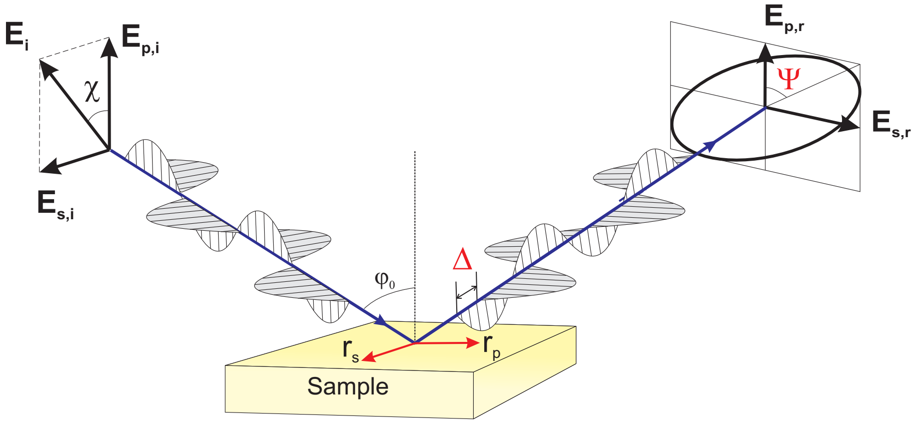

Figure 4.1: Basic principle of ellipsometry. Linear polarized light becomes elliptically polarized after a reflection.

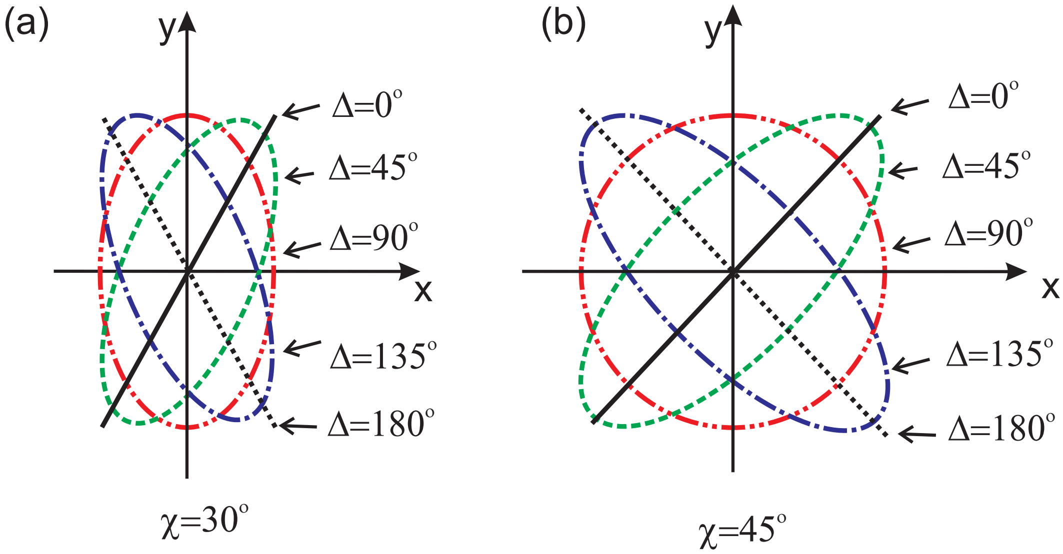

Figure 4.2: Polarization states of the reflected linearly polarized light with polarization angles of 30° (a) and 45° (b) and different phase shift values Δ.

components of the plane wave at medium interfaces are described as follows:

$$\begin{pmatrix} \bar{E}_{\mathrm{p}} \\ \bar{E}_{\mathrm{s}} \end{pmatrix}_{\mathrm{r}} = \begin{pmatrix} \bar{r}_{\mathrm{p}} & 0 \\ 0 & \bar{r}_{\mathrm{s}} \end{pmatrix} \begin{pmatrix} \bar{E}_{\mathrm{p}} \\ \bar{E}_{\mathrm{s}} \end{pmatrix}_{\mathrm{i}}, \tag{4.3}$$

$$\begin{pmatrix} \bar{E}_{\mathrm{p}} \\ \bar{E}_{\mathrm{s}} \end{pmatrix}_{\mathrm{t}} = \begin{pmatrix} \bar{t}_{\mathrm{p}} & 0 \\ 0 & \bar{t}_{\mathrm{s}} \end{pmatrix} \begin{pmatrix} \bar{E}_{\mathrm{p}} \\ \bar{E}_{\mathrm{s}} \end{pmatrix}_{\mathrm{i}}. \tag{4.4}$$

The indices i, r and t denote an incident, a reflected, and a transmitted wave components, respectively. The (2×2) matrices contain the complex reflexion and transmission Fresnel coefficients. Using these matrices, it is possible to describe the reflected or transmitted wave from the incident wave:

$$\bar{r}_{\mathrm{p}} \equiv \frac{\bar{E}_{\mathrm{p,r}}}{\bar{E}_{\mathrm{p,i}}}, \tag{4.5}$$

$$\bar{t}_{\mathrm{p}} \equiv \frac{\bar{E}_{\mathrm{p,t}}}{\bar{E}_{\mathrm{p,i}}}, \tag{4.6}$$

$$\bar{r}_{\mathrm{s}} \equiv \frac{\bar{E}_{\mathrm{s,r}}}{\bar{E}_{\mathrm{s,i}}}, \tag{4.7}$$

$$\bar{t}_{\mathrm{s}} \equiv \frac{\bar{E}_{\mathrm{s,t}}}{\bar{E}_{\mathrm{s,i}}}. \tag{4.8}$$

The Fresnel coefficients can be calculated as follows:

$$\bar{r}_{\mathrm{p}} = \frac{\bar{N}_1 \cos\varphi_0 - \bar{N}_0 \cos\bar{\varphi}_1}{\bar{N}_1 \cos\varphi_0 + \bar{N}_0 \cos\bar{\varphi}_1}, \tag{4.9}$$

$$\bar{r}_{\mathrm{s}} = \frac{\bar{N}_0 \cos\varphi_0 - \bar{N}_1 \cos\bar{\varphi}_1}{\bar{N}_0 \cos\varphi_0 + \bar{N}_1 \cos\bar{\varphi}_1}, \tag{4.10}$$

$$\bar{t}_{\mathrm{p}} = \frac{2\bar{N}_0 \cos\varphi_0}{\bar{N}_1 \cos\varphi_0 + \bar{N}_0 \cos\bar{\varphi}_1}, \tag{4.11}$$

$$\bar{t}_{\mathrm{s}} = \frac{2\bar{N}_0 \cos\varphi_0}{\bar{N}_0 \cos\varphi_0 + \bar{N}_1 \cos\bar{\varphi}_1}, \tag{4.12}$$

where φ_0 is the angle of incidence and $\bar{N}_j$ (j=0,1,2) is the complex index of refraction for respective mediums.

In general case, a sample consists of several layers and the multiple reflections from the layer interfaces must be considered. A schematic sample structure consisting of a substrate and a thin layer with a thickness d is represented in Fig. 4.3. The incident wave in the medium 0 reaches the surface of the medium 1 with the different refractive index. One part of this wave is reflected and the other is refracted, then, the latter is transmitted in the medium 1. If the layer (medium 1) is transparent, the beam is again reflected from the interface between medium 1 and medium 2. The refracted part of the beam enters the medium 2. For such a sample, the multiple reflections and refractions

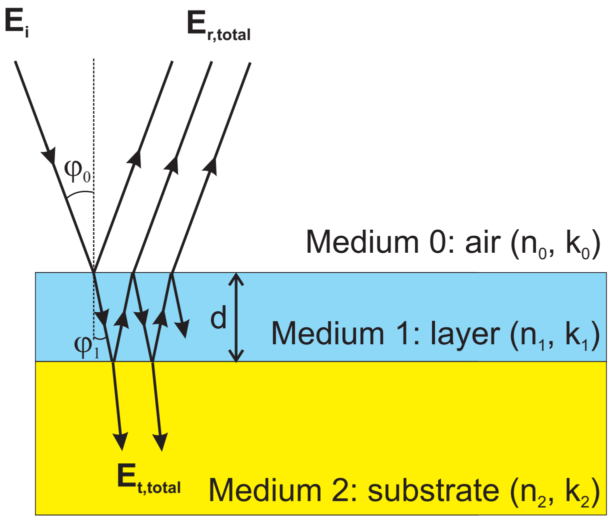

Figure 4.3: Multiple reflections in the thin film.

occur at the layer interfaces. Because of the different optical paths, the reflected beams will differ in phases. An optical path difference has a phase shift β:

$$\begin{aligned}\beta = \bar{N}_1 d \cdot k \cos \bar{\varphi}_1 = kd \cdot \bar{N}_1 \sqrt{1 - \sin^2 \bar{\varphi}_1} &= kd \cdot \bar{N}_1 \sqrt{1 - \frac{\bar{N}_0^2 \sin^2 \varphi_0}{\bar{N}_1^2}} \\ &= \frac{2\pi}{\lambda} d \cdot \sqrt{\bar{N}_1^2 - \bar{N}_0^2 \sin^2 \varphi_0}.\end{aligned} \tag{4.13}$$

Assuming that for an incident medium κ_0=0, the total reflected field strength is obtained by summing up phase shifted separate beams [95]:

$$\bar{E}_{\mathrm{r,total}} = \left(\bar{r}_{01} + \bar{t}_{10} \bar{t}_{01} e^{\mathrm{i}2\beta} \sum_{\nu=2}^{\infty} \left(\bar{r}_{10}\right)^{\nu-2} \left(\bar{r}_{12}\right)^{\nu-2} e^{-\mathrm{i}2\nu\beta} \right) \cdot \bar{E}_{\mathrm{e}}, \tag{4.14}$$

where $\bar{r}$ and $\bar{t}$ indicate reflection and transmission, respectively, complex Fresnel coefficients and their indices indicate the interfaces between the respective mediums. The summation term in Eq. 4.14 build up a convergent series and yields

$$\bar{E}_{\mathrm{r,total}} = \left(\frac{\bar{r}_{01} + \bar{r}_{12} e^{-\mathrm{i}2\beta}}{1 + \bar{r}_{01} \bar{r}_{12} e^{-\mathrm{i}2\beta}} \right) \cdot \bar{E}_{\mathrm{e}}. \tag{4.15}$$

The pseudo-reflection Fresnel coefficients are described:

$$\langle \bar{r}_{\mathrm{p}} \rangle \equiv \frac{\bar{E}_{\mathrm{p,r,total}}}{\bar{E}_{\mathrm{p,i}}} = \frac{\bar{r}_{\mathrm{p},01} + \bar{r}_{\mathrm{p},12} e^{-\mathrm{i}2\beta}}{1 + \bar{r}_{\mathrm{p},01} \bar{r}_{\mathrm{p},12} e^{-\mathrm{i}2\beta}}, \tag{4.16}$$

$$\langle \bar{r}_{\mathrm{s}} \rangle \equiv \frac{\bar{E}_{\mathrm{s,r,total}}}{\bar{E}_{\mathrm{s,i}}} = \frac{\bar{r}_{\mathrm{s},01} + \bar{r}_{\mathrm{s},12} e^{-\mathrm{i}2\beta}}{1 + \bar{r}_{\mathrm{s},01} \bar{r}_{\mathrm{s},12} e^{-\mathrm{i}2\beta}}. \tag{4.17}$$

From the pseudo-reflection Fresnel coefficients the ellipsometric parameters (Ψ and Δ) are derived

$$\bar{\rho} = \frac{\langle \bar{r}_{\mathrm{p}} \rangle}{\langle \bar{r}_{\mathrm{s}} \rangle} = \frac{|\langle \bar{r}_{\mathrm{p}} \rangle|}{|\langle \bar{r}_{\mathrm{s}} \rangle|} \cdot e^{\mathrm{i}(\delta_{\mathrm{p}} - \delta_{\mathrm{s}})} \equiv \tan \Psi \cdot e^{\mathrm{i}\Delta}, \tag{4.18}$$

where δ_{p} and δ_{s} are the phase difference between the reflected and incident electric fields for parallel and perpendicular components, respectively, and Δ is the phase difference between the latter.

4.2 Infrared ellipsometer

An infrared spectroscopic ellipsometer (IR-SE) is used to investigate the vibrational properties of the material. Sentech company's IR-SE covering the spectral range from 300 cm^{-1} to 2000 cm^{-1} is used. An experimental setup of the IR-SE is shown in Fig. 4.4. An infrared light is emitted from a glowing black-body source. The Michelson interferometer is employed to produce an interferogram that passes the polarizer P_1, reflects from a sample and a retarder (with the known phase shift δ), passes a polarizer P_2 and enters a detector. A measured signal is digitized and a Fourier transformation is performed. Finally, an infrared spectrum is obtained. In order to obtain ellipsometric parameters Ψ and Δ, measurements are performed at four different polarizator P_1 angles $\alpha = 0°, 45°, 90°$ and $135°$, while the polarizator P_2 is fixed at angle α_2 [96]. After

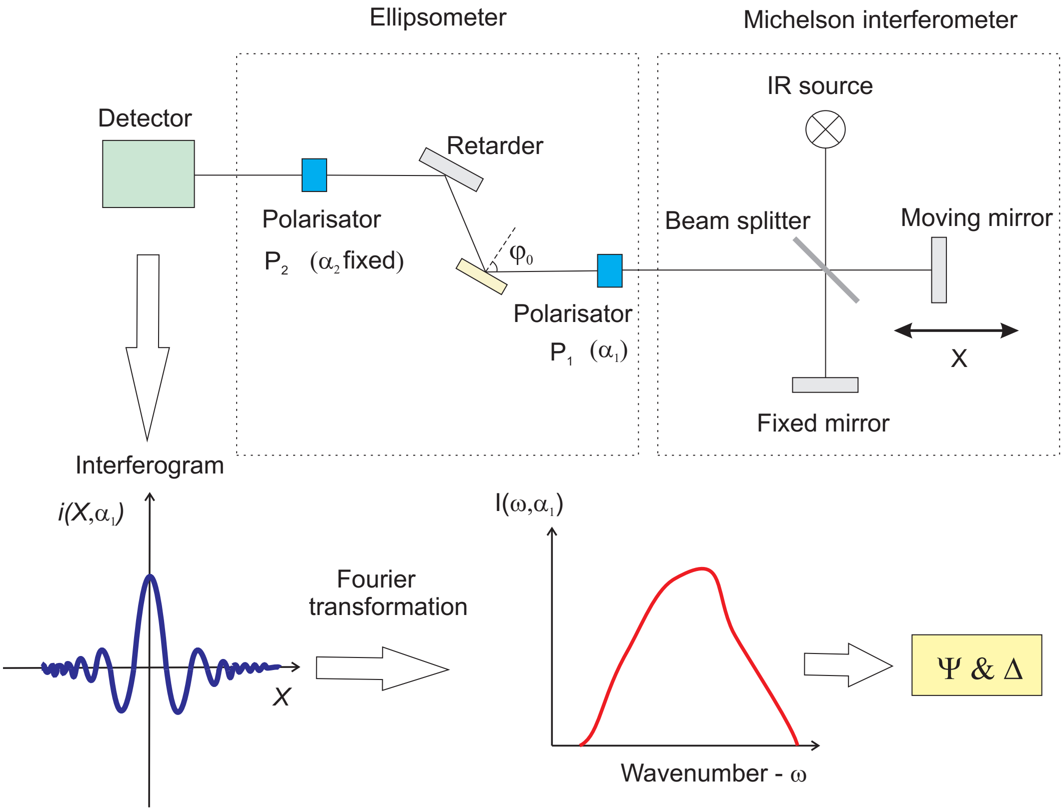

Figure 4.4: Schematic sketch of the IR spectroscopic ellipsometer setup.

applying the Fourier transformation, the measured intensity is expressed by the following relation:

$$\begin{aligned} I(\omega{,}\alpha_1) &= \frac{1}{2}(r_x^2\cos^2\alpha_2 + r_y^2\sin^2\alpha_2)(1-\cos 2\Psi'\cos 2\alpha_1 + \sin 2\Psi'\cos\Delta\sin 2\alpha_1)F(\alpha_1), \\ I(\omega{,}\alpha_1) &= \frac{1}{2}(s_0 + s_1\cos 2\alpha_1 + s_2\sin 2\alpha_1)F(\alpha_1), \qquad (4.19) \end{aligned}$$

where s_0, s_1 and s_2 are the Fourier coefficients and are calculated from the ratio $I(\omega{,}\alpha_1)/F(\alpha_1)$. The factor $F(\alpha_1)$ is determined from the calibration measurements without any sample. For calibration measurements $\cos 2\Psi=0$, $\cos\Delta=1$, and $r_x=r_y=1$. By fixing polarizer's P_2 angle at $\alpha_2=45°$ and choosing $\alpha_1=0°$, 45°, 90°, the factor $F(\alpha_1)$ is the measured intensity:

$$I_0(\omega{,}\alpha_1) = \frac{1}{2}(1+\sin 2\alpha_1)F(\omega{,}\alpha_1). \qquad (4.20)$$

For different polarizer P_1 angles α_1, the factor $F(\omega{,}\alpha_1)$ is expressed as follows:

$$\begin{aligned} F(\omega{,}0°) &= 2I_0(\omega{,}0°), &(4.21)\\ F(\omega{,}45°) &= I_0(\omega{,}45°), &(4.22)\\ F(\omega{,}90°) &= 2I_0(\omega{,}90°). &(4.23) \end{aligned}$$

Using Eqs. 4.21-4.23, the measured intensities in Eq. 4.19 are normalized:

$$\begin{aligned} \bar{I}_0 &= \frac{I(\omega{,}0°)}{2I_0(\omega{,}0°)} = \frac{1}{2}(s_0+s_1), &(4.24)\\ \bar{I}_1 &= \frac{I(\omega{,}45°)}{2I_0(\omega{,}45°)} = \frac{1}{2}(s_0+s_2), &(4.25)\\ \bar{I}_2 &= \frac{I(\omega{,}90°)}{2I_0(\omega{,}90°)} = \frac{1}{2}(s_0-s_1). &(4.26) \end{aligned}$$

For the three polarizer azimuths, the ellipsometric parameters Ψ and Δ are determined:

$$\begin{aligned} \cos 2\Psi' &= -\frac{s_1}{s_0} = \frac{I_2-I_0}{I_2+I_0}, &(4.27)\\ \sin 2\Psi'\cos\Delta &= \frac{s_2}{s_0} = \frac{2I_1}{I_2+I_0} - 1, &(4.28)\\ \tan\Psi' &= \frac{\tan\Psi}{\tan\alpha_2}. &(4.29) \end{aligned}$$

In the extended measurements mode $0° \leq \Delta \leq 360°$, it is necessary to use an additional polarizer angle $\alpha_1=135°$ [96].

4.3 Variable angle ellipsometer

A commercial variable angle rotating analyzer ellipsometer from J.A. Woollam Co, Inc. company is used to conduct measurements in the spectral range 0.56-6.42 eV. A variable angle of incidence permits to obtain more accurate measurements, since the modelling of the Ψ and Δ parameters measured at different angles of incidence reduces a correlation between the optical constants and film thickness. A simplified schema of a variable angle rotating analyzer spectroscopic ellipsometer is presented in Figure 4.5. A high-pressure xenon lamp is used as a light source. First, the light from the xenon lamp shines on a monochromator. Then, the monochromatic light reaches a collimator via an optical fiber cable. After passing a polarizer, it becomes linearly polarized. In addition, a compensator (as an optional element) can be used for the advanced ellipsometry measurements. The polarized light shines a sample, then, reflects, passes through a rotating analyzer and, finally, reaches an InGaAs or a Si diode detector (depending in which spectral range a measurement is conducted). A signal intensity in the detector is described as

$$I_\mathrm{D} \propto 1 + \alpha \cos(2A) + \beta \sin(2A), \tag{4.30}$$

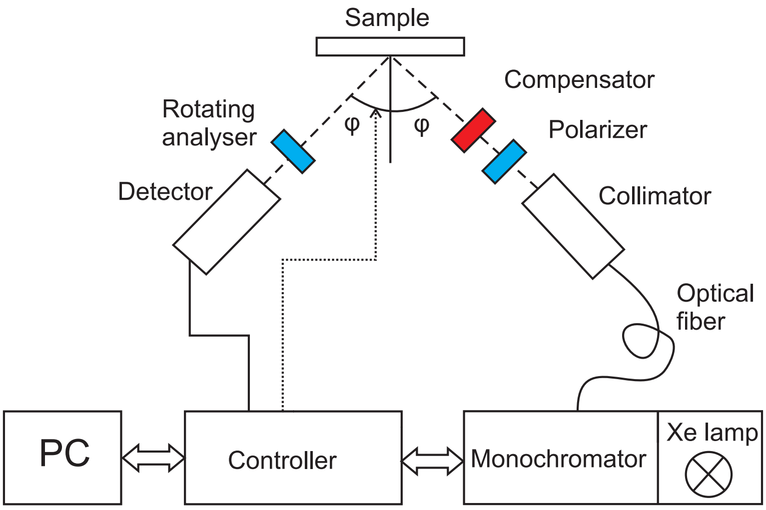

Figure 4.5: Schematic representation of the rotating analyzer ellipsometer setup.

where A is an azimuthal angle of the analyzer. Both measured parameters are the Fourier coefficients α and β that are expressed as

$$\alpha = \frac{\tan^2\Psi - \tan^2 P}{\tan^2\Psi + \tan^2 P} \quad \text{and} \tag{4.31}$$

$$\beta = \frac{2\tan\Psi\cos\Delta\tan P}{\tan^2\Psi + \tan^2 P} \ , \tag{4.32}$$

where P is an azimuthal angle of the polarizator. From the obtained Fourier coefficients, the ellipsometric parameters Ψ and Δ are derived by using the following relations:

$$\tan\Psi = \sqrt{\frac{1+\alpha}{1-\alpha}} \cdot |\tan P| \ , \tag{4.33}$$

$$\cos\Delta = \frac{\beta}{\sqrt{1-\alpha^2}} \cdot \frac{\tan P}{|\tan P|} \ . \tag{4.34}$$

Before conducting the measurements, an ellipsometer is calibrated in order to determine the parameters A_0 and P_0 (absolute angles of the analysator and polarizator, respectively) as well as η representing a calibration parameter equal to the relative attenuation of the AC component of the detector signal with respect to the DC component. The experimentally determined α and β are corrected with A_0 and η. The corrected Fourier coefficients are expressed as

$$\alpha' = \eta(\alpha\cos 2A_0 + \beta\sin 2A_0) \ , \tag{4.35}$$

$$\beta' = \eta(\beta\cos 2A_0 - \alpha\sin 2A_0) \ . \tag{4.36}$$

Then, the equations (4.33) and (4.34) are transformed to

$$\tan\Psi = \sqrt{\frac{1+\alpha'}{1-\alpha'}} \cdot |\tan(P-P_0)| \ , \tag{4.37}$$

$$\cos\Delta = \frac{\beta'}{\sqrt{1-\alpha'^2}} \cdot \frac{\tan(P-P_0)}{|\tan(P-P_0)|} \ . \tag{4.38}$$

By employing the expressions (4.35) - (4.38), the ellipsometric parameters Ψ and Δ are derived.

4.4 Synchrotron ellipsometer

A synchrotron ellipsometer setup attached at the Berlin electron storage ring (BESSY II) is a large-scale facility at Helmholtz-Zentrum Berlin (HZB) and provided by the research group of prof. N. Esser and dr. C. Cobet from the ISAS Berlin. The synchrotron ellipsometer is designed to serve researchers from universities, research institutions and industry. Figure 4.6 shows the bird's eye view of the BESSY II synchrotron ring.

The ellipsometer uses a synchrotron light obtained from the TGM4 or 10m-NIM beam lines and covering the spectral range from 3 up to 30 eV photon energy. This synchrotron ellipsometer, permitting to investigate the materials in such a wide photon energy range, is unique worldwide.

The synchrotron ellipsometer setup and its simplified schematic sketch are shown in Fig. 4.7 and Fig. 4.8, respectively. All optical components of the ellipsometer setup are mounted in an ultra-high vacuum (UHV) chamber, since an air (nitrogen) absorbs the light with photon energies above ≈6.5 eV(≈9.5 eV). Where are no transparent materials which can be used as window in the chamber above 10 eV photon energy. For this reason, the vacuum chamber of the ellipsometer has to be connected with the UHV system of the electron storage ring. The base pressure of 2×10^{-10} mbar is created in the main ellipsometer's chamber where the sample is mounted. The synchrotron ellipsometer is based on a rotating-analyzer ellipsometry design.

Figure 4.6: BESSY II synchrotron ring.

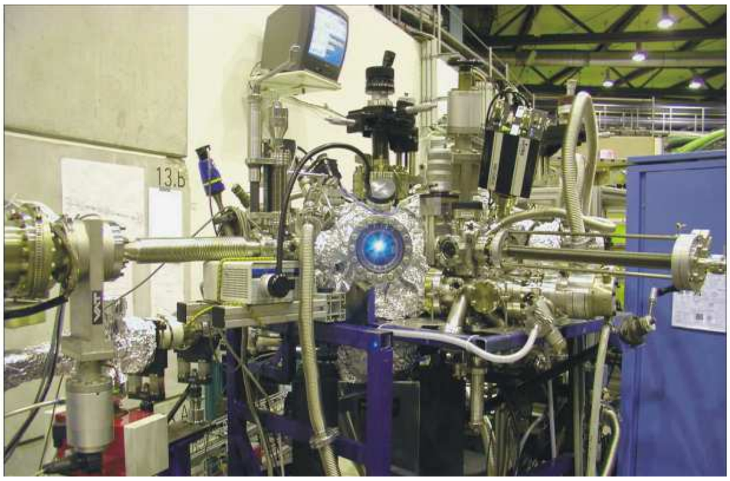

Figure 4.7: Synchrotron ellipsometer setup.

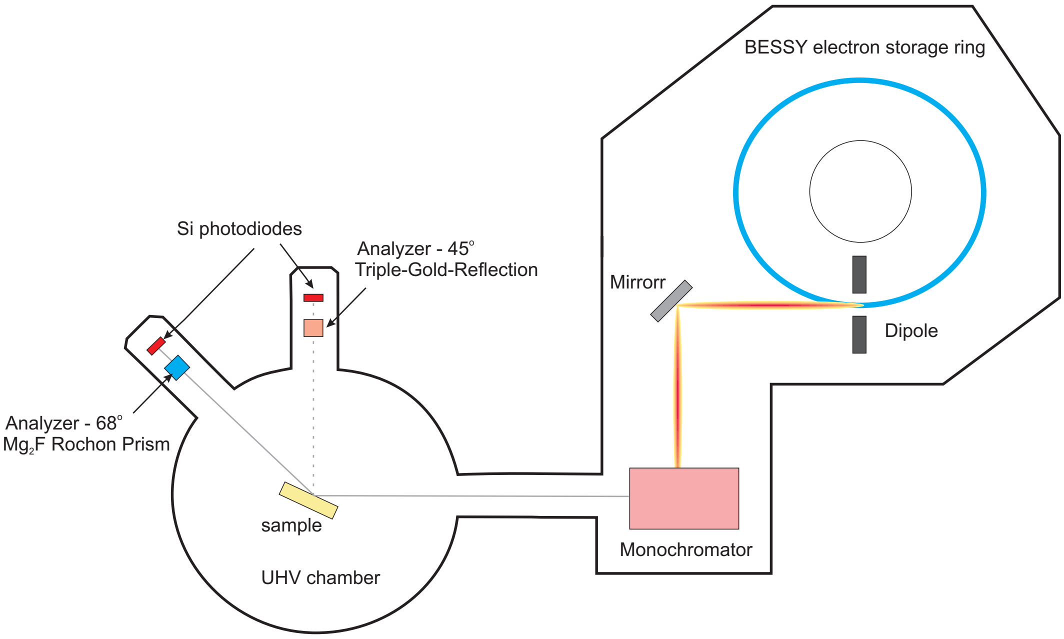

Figure 4.8: Simplified schematic representation of the synchrotron ellipsometer setup.

As it is indicated in Fig. 4.8, the incoming linearly polarized synchrotron light reflects from a grating monochromator, then, the monochromatic light beam shines on a sample mounted in the UHV chamber and after reflection from the sample enters an analyzer chamber. Depending on the measured photon energy range, the angle of incidence is chosen at 45° or at 68°. Each analyzer chamber is equipped with a rotating analyzer and a Si-photodiode detector. For the energies below 10 eV the MgF_2 polarizer is used in the analyzer chamber tilted at 68°, while for the energies above 10 eV the triple reflection *gold-Si-gold* polarizer is used in the analyzer chamber tilted at 45°. In order to remove the surface contaminations on the sample, the annealing of the sample is performed in the UHV chamber. More detailed description about this synchrotron ellipsometer can be found elsewhere [97, 98].

4.5 Ellipsometry data analysis

For an arbitrary sample, a so called *pseudo* DF is obtained from the equation

$$< \bar{\varepsilon} >= \sin^2\varphi \left[1 + \tan^2\varphi \left(\frac{1-\bar{\rho}}{1+\bar{\rho}} \right)^2 \right] \ , \tag{4.39}$$

where φ is an angle of incidence. Equation 4.39 yields a *true* DF only for a semi-infinite isotropic bulk crystal with a perfect surface. It is important to understand that the investigated samples are not *ideal* and contain a thickness non-uniformity, interface and surface roughness. To extract the *true* DF of the investigated sample, the ellipsometry experimental data are needed to be simulated. An optical multilayer model [99], which includes a substrate, interfaces, investigated layer, and surface roughness overlayer, is applied. The optical constants of the the substrate and the layers, which are below the top layer, are taken from the database or measured separately. The surface roughness is taken into account by including an over-layer for which the DF is given by the Bruggeman effective medium approximation (EMA) [100] assuming 50% air voids in the top layer matrix. In order to reduce a correlation between a layer thickness and a DF, ellipsometric parameters Ψ and Δ are recorded at several different angles of incidence. All data are fitted together to get the layer thicknesses and the DF of the investigated top layer. The experimental values (Ψ_{meas} and Δ_{meas}) and model generated values (Ψ_{model} and Δ_{model}) are fitted using the Levenberg-Marquardt algorithm to minimize the mean square error (MSE):

$$MSE = \frac{1}{N-M} \sum_{i=1}^{N} \left[\left(\frac{\Psi^i_{\mathrm{model}} - \Psi^i_{\mathrm{meas}}}{\sigma^i_{\Psi}} \right)^2 + \left(\frac{\Delta^i_{\mathrm{model}} - \Delta^i_{\mathrm{meas}}}{\sigma^i_{\Delta}} \right)^2 \right] , \tag{4.40}$$

where N is the number of Ψ and Δ pears and M is the number of the fitted parameters in the model. The standard deviation of the experimental data is defined by σ. Fig. 4.9

shows a typical result of the fitting procedure; the measured and simulated (using a multi-layer model) ellipsometric parameters Ψ and Δ as well as $<\varepsilon_1>$ and $<\varepsilon_2>$ values

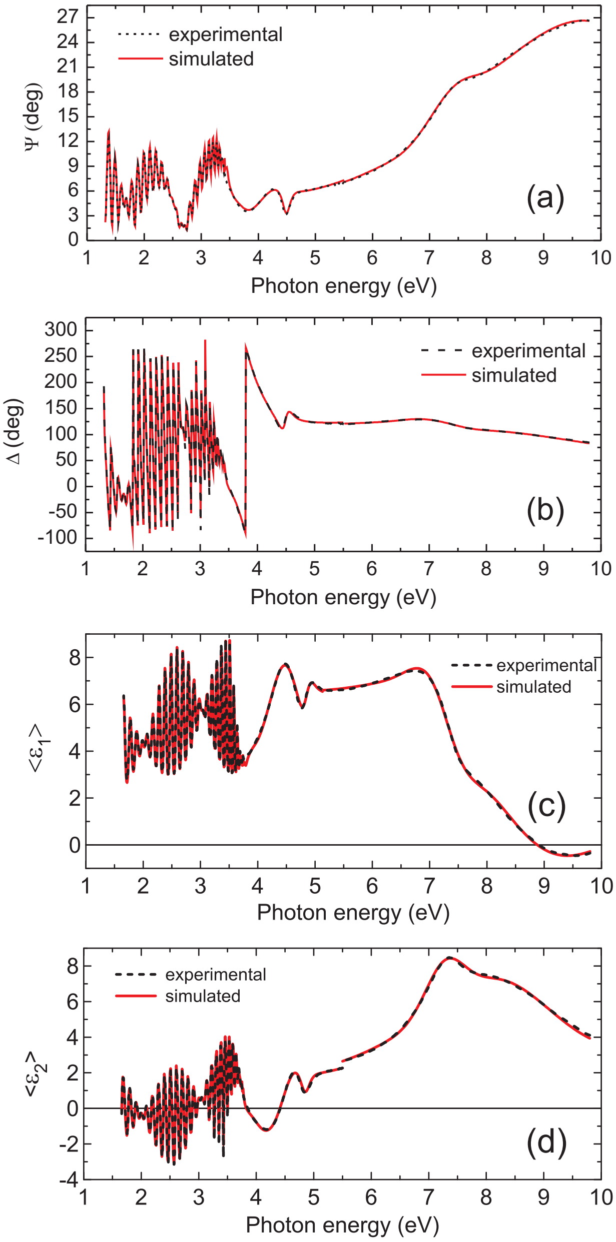

Figure 4.9: Measured (black dashed line) and fitted (red solid line) ellipsometric parameters Ψ (a) and Δ (b) as well as $<\varepsilon_1>$ (c) and $<\varepsilon_2>$ (d) as a function of photon energy for AlInGaN (Al 56% and In 3%)) sample. The data refer to an angle of incidence of 67°.

are shown in Fig. 4.9(a), (b), (c), and (d), respectively, as a function of photon energy for the (0001)-oriented quaternary AlInGaN film (grown on GaN/AlN/sapphire substrate) at the angle of incidence of 67°. No assumption is made concerning the spectral shape of the DF, i.e., ε_1 and ε_2 were fitted separately for each photon energy followed by a proof of Kramers-Kronig consistency between two quantities. The multi-layer consists of the sapphire substrate, the AlN and GaN buffer layers (with the already known DFs), and finally, the AlInGaN film which is of particular interest. The peculiarities for three ranges (transparent, around the band gap, and at high photon energies) are well reproduced. Fabry-Perot like oscillations with small energy spacing appear in the range below 3.4 eV for which the thick GaN film becomes transparent. The long-period envelop reflects the contribution from the much thinner AlN buffer and AlInGaN layer. The next feature is found around 3.4 eV where Ψ exhibits a sharp dip, it is unambiguously attributed to the band gap of AlInGaN. Because the thick GaN layer is already opaque in this range, the fit is very sensitive to the DF of AlInGaN. Finally, the features above 7 eV arise from contributions related to the high-energy critical points of the band structure, as it can be observed in $<\varepsilon_2>$ shown in Fig.4.9(d).

As ellipsometry is not a direct deductive method (only the parameters Ψ_{meas} and Δ_{meas} are measured directly and the optical constants and film thickness are obtained indirectly via modeling), it is also worth to check the investigated film thickness or surface roughness with other characterization tools, e.g., XRD, SEM, or TEM (for a film thickness) and AFM (for a surface roughness).

In the following example, it will be demonstrated that a free-carrier concentration absorption modelling with the Drude oscillator significantly improves a multilayer model for the InN sample. It is known that an InN material has an electron accumulation at the surface [87–93] and at the interface (between an InN and a buffer layer or a substrate) [101]. Using high-resolution electron-energy-loss spectroscopy (HREELS), Veal *et al* [101] found that the surface sheet density at the InN/GaN interface is to be in the the order of 10^{13} cm^{-2}. The free electrons exhibit a distinctive optical absorption that can be described by using the Drude model (this is a special case of a single Lorentz oscillator with the center energy fixed at zero).

Fig. 4.10 shows two different multilayer models used for the experimental ellipsometry data fitting for the InN sample (indicated as sample C0 in Chapter 6). On the left side of the figure, the multilayer model consisting of a sapphire substrate, a GaN buffer layer, an InN layer, and an overlayer (EMA layer consisting of 50% of InN material and 50% air voids). A multilayer model presented on the right side of the Fig. 4.10, in addition, has a 10 nm thick interlayer that contains the Drude oscillator and the known InN parametric oscillator model [2].

Below the schematic multilayer representations the experimental and fitted Ψ parameters as well as the obtained DF together with the point-by-point DF are shown. It is clearly seen that by inserting the interlayer that contains the Drude oscillator, the model fit improves significantly.

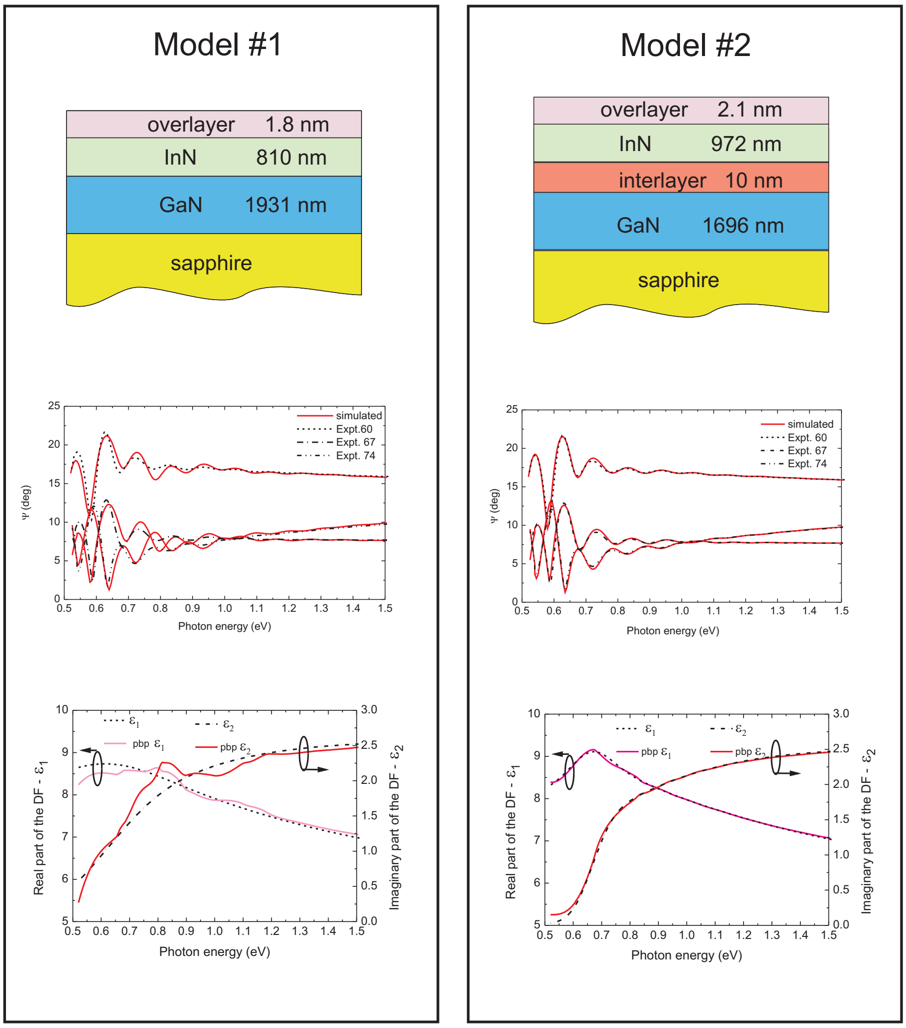

Figure 4.10: Optical multilayer model without (model No. 1) and with (model No. 2) an interlayer.

5 Epitaxial growth

Several techniques are used to grow III-V nitride materials: metalorganic vapour phase epitaxy (MOVPE), molecular beam epitaxy (MBE), hydrogen vapour phase epitaxy (HVPE), and remote plasma chemical vapour deposition (RPCVD) [102]. For industrial production of the nitride based optoelectronic devices, the MOVPE equipments are widely used. The MOVPE allows high growth ratios, high wafer throughput and precise *in-situ* temperature and growth monitoring. With the MOVPE system it is possible to grow relatively thick films (several micrometers), to control the layer thickness in the nanometer range and the composition in the alloy. This is necessary to grow high quality quantum structures used in LEDs. Alternative epilayer growth techniques are MBE, HVPE, and RPCVD. The MBE allows a better control of the film thickness and the alloy composition. However, the MBE growth needs ultra-high vacuum and the growth rates are very slow, therefore, it is more used at the research scale. The HVPE offers very high growth rates, permitting to grow very thick films (several millimeters). A disadvantage of the HVPE is that it is difficult to control a film thickness and it is not possible to grow very thin quantum structures that are necessary for LEDs production. The RPCVD technique allows to grow films at lower temperatures. This is very promising for the growth of high quality In-rich InGaN alloys.

All investigated samples in this work were grown by MOVPE or MBE, therefore, theses techniques will be shortly introduced in the next sections.

5.1 MOVPE epitaxial growth

In this section, the basic principles of the MOVPE process and equipment setup will be briefly described. Fig. 5.1 demonstrates the MOVPE growth process. A gas mixture consisting of the precursors passes over a heated substrate. The precursor molecules pyrolyze. The atoms bind to a substrate surface and a new crystalline epilayer is grown. The precursors for III-V nitrides are group III metals such as an aluminum (Al), a gallium (Ga), and an indium (In) as well as group V element nitrogen (N). The standard metalorganic precursors are a trimethylgallium (TMGa), a trimethylalliuminium

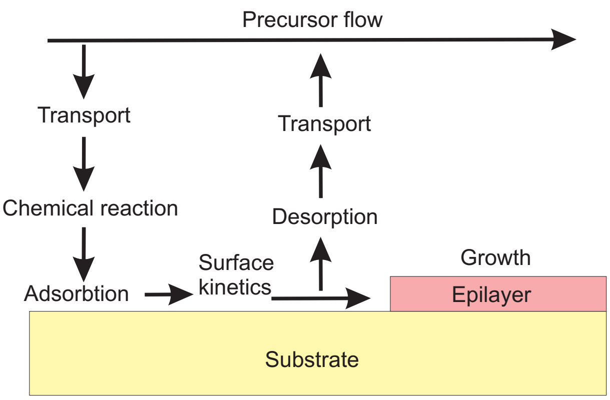

Figure 5.1: MOVPE growth process.

(TMAl), and a trimetylindium (TMIn). A schematic drawing of the TMGa molecule is shown in Fig. 5.2. The ammonia (NH_3) is used as a precursor for the group V element nitrogen. The reaction is described by equation

$$R_3M_{gas} + EH_{3(gas)} = ME_{(solid)} + 3RH_{(gas)}, \tag{5.1}$$

where R is an organic alkyl, M is the group III metal, and E is the group V element.

A temperature of the substrate controls an adsorption, a surface kinetics, and a desorption. The growth rate in a logarithmic scale as a function of inversed substrate temperature T_S is shown in Fig. 5.3. Three growth regimes are distinguished: kinetic limited, transport limited and desorption.

The n-type doping in III-V compounds is achieved by using hydride precursors silane (SiH_4) and germane (GeH_4). The p-type doping is obtained by using a Cp_2Mg. A residual oxygen and moisture are presenting in the ammonia. Therefore, the oxygen is incorporated in the grown epilayers [103]. A highly corrosive chemical ammonia is

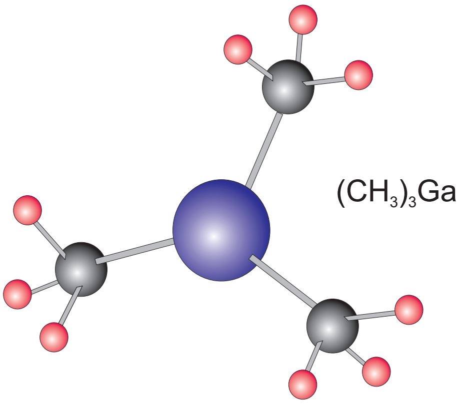

Figure 5.2: Schematic drawing of the TMGa molecule.

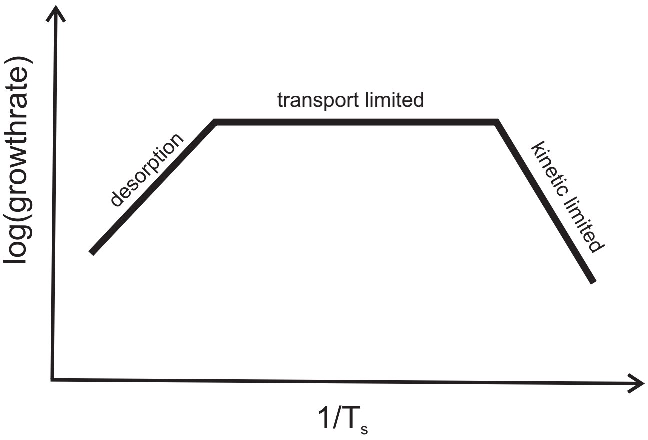

Figure 5.3: Growth rate in a logarithmic scale as a function of inverse substrate temperature.

believed to react with a stainless steel that causes the contaminations in the epilayers. Transition metals (iron, chromium, and vanadium) are also detected in grown layers [104]. A carbon, which comes from the metalorganics, is very common contaminant in the epilayers [104, 105].

Stacking faults and dislocations in an epilayer are caused due to a lattice mismatch. A thermal mismatch causes the epilayer to crack during cooling process. III-V nitride semiconductors an InN, a GaN, and an AlN as well as their related alloys are commonly grown on a sapphire substrate. The growth on c-plane and a-plane sapphire yields a c-plane orientation, while growth on r-plane sapphire yields an a-plane orientation of the epilayer. Other more common substrates are a SiC and a Si(111). A silicon substrate is promising as being very cheap and commercially viable. Recently, Dadgar *et al* [106] demonstrated a crack-free highly conductive GaN (doped with Ge) epilayer grown on a Si substrate. A free-standing GaN prepared by HVPE is very expensive substrate. However, for high reliability devices a low concentration of threading dislocations is required, therefore, a homoepitaxy is needed.

5.1.1 MOVPE setup

MOVPE systems are widely used in research as well as in industrial sector. With increasing LED market, the MOVPE system manufacturers already sell the equipments adapted for 8-inch wafers. The main elements in the MOVPE system are a reactor, a gas storage unit and a control unit. Fig. 5.4 shows a schematic representation of the AIXTRON Close Coupled Showerhead system. Precursor source flows are stabilized by using a vent line. Just before the growth process, the 5/2 valves switch the source stream to the run lines. The flow rates are controlled by mass flow controllers. The

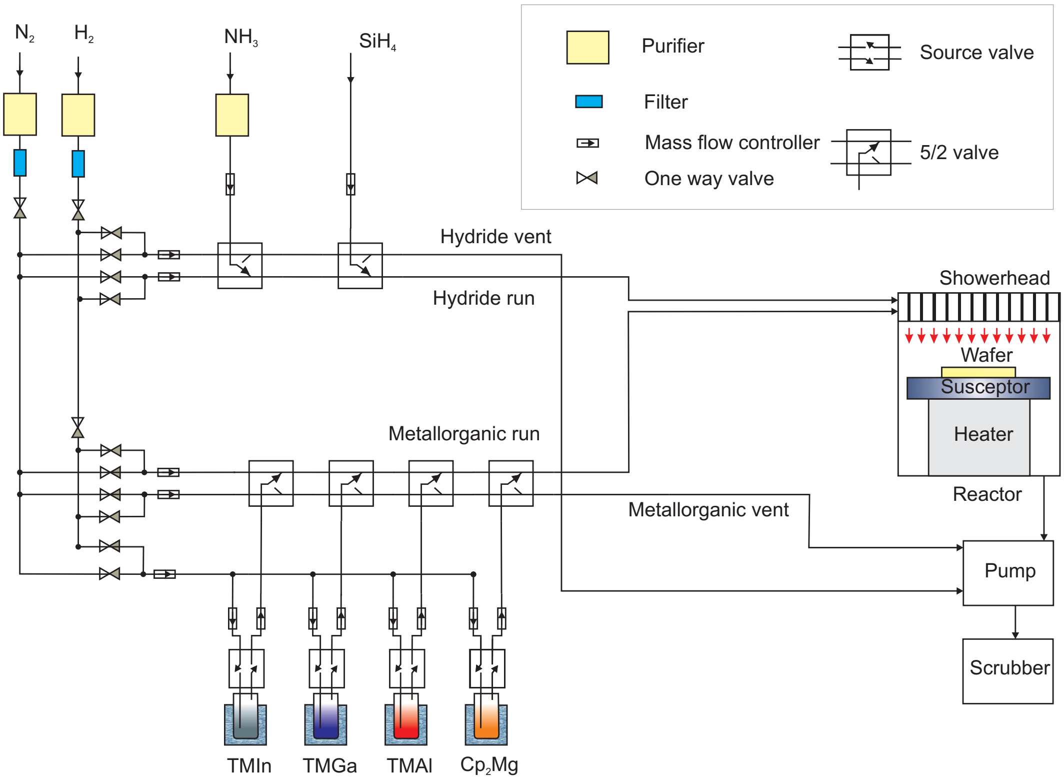

Figure 5.4: Schematic sketch of the MOVPE system.

group III and V precursors arrive at reactors' shower head in two separated plenum chambers. They are mixed inside the reactor chamber and deposits on the hot wafer. In order to have a better epilayer uniformity, a susceptor is rotating together with a wafer on it. The heater is installed below the susceptor. The exhaust gases are pumped out and neutralized in the scrubber.

A constant pressure is kept in the reactor. A partial pressure of the gaseous precursor is expressed as [107]

$$P_{gp} = \frac{Q_{gp}}{Q_{tot}} P_r, \tag{5.2}$$

where Q_{gp}, Q_{tot}, P_r are a flow of the precursor, a total flow, and a total reactor pressure, respectively. The metalorganics are kept in the so called *bubbles* that assure stable temperature. The stability of the temperature and, consequently, the stability of the vapour pressure is very important, because only defined precursor quantities must be provided in the reactor. A vapour pressure of the metalorganic is expressed as

$$log_{10}(P) = B - \frac{A}{T}, \tag{5.3}$$

where P is a pressure in Torr, T is the temperature in Kelvin, A and B are the coefficients for the group III metalorganics listed in Table 5.1.

Table 5.1: Vapour pressure for the group III metalorganics (data from AkzoNobel).

Metallorganic	Molecular formula	A	B	Vapour pressure @10° (Torr)
TMAl	$(CH_3)_3Al$	2134	8.224	6.57
TMGa	$(CH_3)_3Ga$	1703	8.07	113.6
TEGa	$(C_2H_5)_3Ga$	2162	8.083	2.80
TMIn	$(CH_3)_3In$	3204	10.98	0.46

Carrier gases are used to transport the metalorganics from the bubblers to the reactor. A hydrogen (H) or a nitrogen (N) of very high purity (9N=99.9977777%) are used as carrier gases. The carrier gas flows to the bublers, then, the gas mixture of the metalorganics and the carrier gas is obtained and transfered to the reactor via pipelines. The piplines are separated for the group III metals and the group V element (ammonia). To achieve a high quality epilayers and reduce an oxygen incorporation, the high purity precursors are required. Even the highest purity ammonia (6.0 equivalent to 99.9999%) contains a moisture and foreign residual substances. Additionaly, the purification units, which contain catalytic metal filters, are used in the gas lines, as it is shown in Fig. 5.4.

5.1.2 In-situ optical monitoring

An *in-situ* monitoring is very important for the growth control in the MOVPE reactor. A growth rate, a layer thickness, a wafer curvature as well as a growth temperature can be monitored *in-situ* in the MOVPE reactor. Here, an example of the *in-situ* monitoring will be shown for the InN sample growth. The commercial company's Laytec *in-situ* reflectance, temperature, and curvature measurement system, installed in the MOVPE reactor, was used for a growth monitoring. A detailed description of the Laytec *in-situ* system can be found elsewhere [108].

A sample consisting of a substrate and a thin layer with incident and reflected beams is depicted in Fig. 5.5. The incident light intensity is denoted as I_i and the

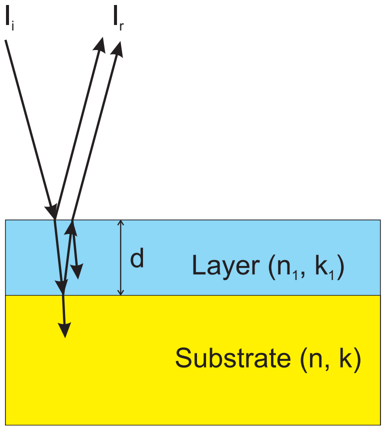

Figure 5.5: Schematic drawing of the sample consisting of a substrate and a thin film. The arrows indicate incident and reflected beams.

reflected light intensity is denoted as I_r. In short, the reflectance is described as the ratio of the incident and reflected light:

$$R = \frac{I_r}{I_i}. \tag{5.4}$$

Assuming that an ambient medium has a refractive index n_0=1 and the normal incidence of the light beam, the reflectivity from the first interface (ambient-layer) is expressed as follows:

$$R = \frac{(n_1 - 1)^2 + \kappa_1^2}{(n_1 + 1)^2 + \kappa_1^2}, \tag{5.5}$$

where n_1 is a refractive index and κ_1 is an extinction coefficient of the top layer. However, if the thin layer deposited on the substrate is transparent for the used light wavelength, the multiple reflections from the surface and interface will occur. By growing an epilayer, its thickness will increase with a time and the Fabry-Perot oscillations will be observed in a signal of the reflected light. The growth rate is determined from the Fabry-Perot oscillations period [109]:

$$r = \frac{\lambda / n_1}{2 \cdot \Delta t}, \tag{5.6}$$

where Δt is an oscillation period, n_1 is a refraction index of the epilayer at wavelength λ.

For example, Fig. 5.6(a) shows *in-situ process* (black line) and *true* (blue line) temperatures for the InN layer grown on an AlN and a GaN buffer layers with a sapphire substrate. Here, the *process* temperature is called a temparature measured with a thermocouple installed near the heating element below a subsceptor. The *true* temperature is called a temperature obtained from the emissivity-corrected pyrometry. A detailed de-

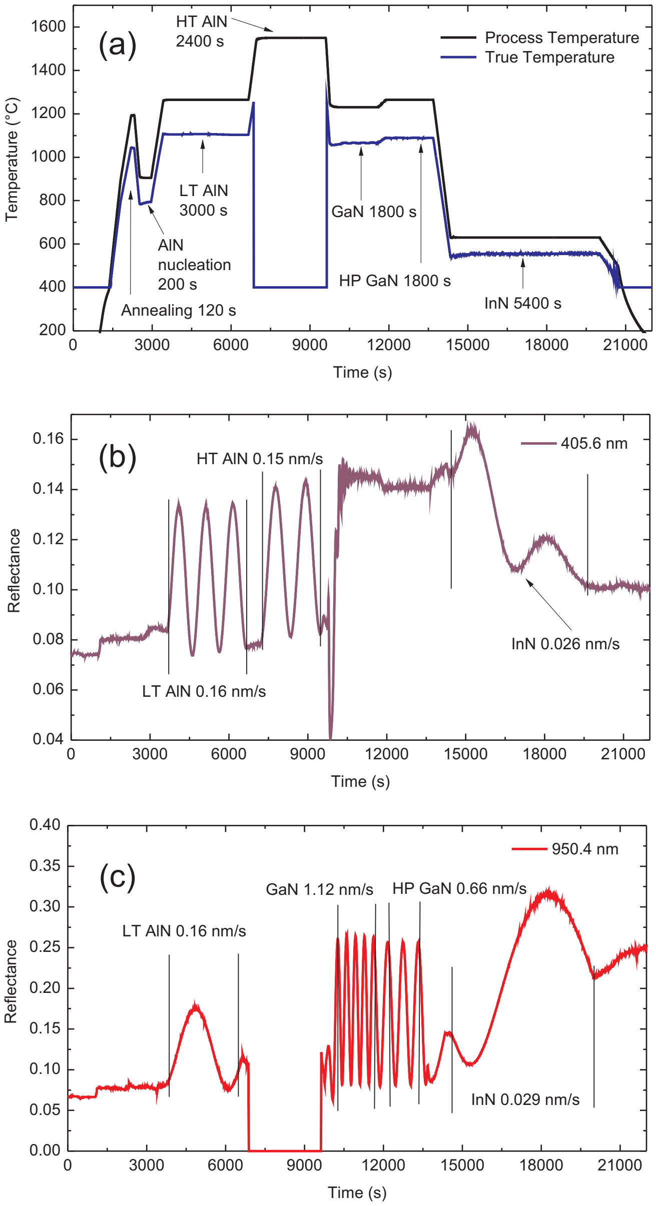

Figure 5.6: In-situ temperature (a) as well as reflectance at the wavelength of 405.6 nm (b) and 950.4 nm (c) measured for the InN sample grown on GaN/sapphire template.

scription of the emissivity-corrected pyrometry is given elsewhere [110]. For the *in-situ* growth analysis, the high-temperature optical constants of GaN and AlN were used from the database (provided in the commercial Laytec software). However, the optical con-

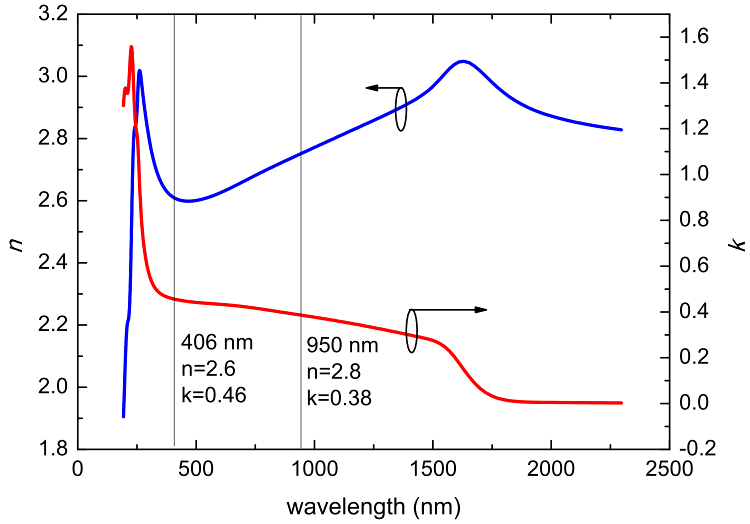

Figure 5.7: Room temperature optical constants for InN.

stants for the InN were not provided in the database, therefore, the room temperature InN optical constants, determined by spectroscopic ellipsometry, were employed. The room temperature optical constants for the InN sample (indicated as sample B0 in Chapter 6) are shown in Fig. 5.7. Drago *et al* [111] measured the optical constants at various temperatures and demonstrated that significant deviation from room temperature optical constants occurs only in the photon energy range above 3 eV (or below 413.3 nm). From the fit of the Fabry-Perot oscillations, it was possible to determine the growth rate of the epilayer. Fig. 5.6(b) and (c) show the reflectance measurements at 405.6 nm and 950.4 nm, respectively. The low-temperature (LT) AlN buffer layer growth rate was determined to be 0.16 nm/s from both 405.6 nm and 950.4 nm wavelength reflectance. The high-temperature (HT) AlN layer growth temperature was determined to be 0.15 nm/s from the 405.6 nm wavelength reflectance. The GaN and high-pressure (HP) GaN buffer layers growth rates were determined to be 1.12 nm/s and 0.66 nm/s, respectively, from

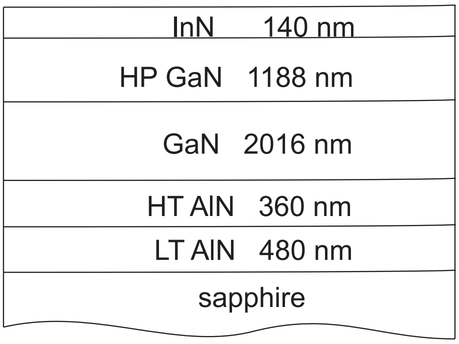

Figure 5.8: Schematic multilayer representation of the grown sample.

the 950.4 nm wavelength reflectance. And finally, the InN layer growth rate was determined to be 0.026 nm/s and 0.029 nm/s from 405.6 nm and 905.4 nm wavelength reflectance, respectively. With the knowledge of the growth time and growth ratio, it is possible to calculate the layer thickness. A schematic grown multilayer structure with the indicated layer thicknesses is represented in Fig. 5.8.

It is also important to control a curvature of a wafer in the MOVPE growth process [112]. Where are several reasons causing the curvature of the wafer. The in-plane lattice parameter of the epilayer normally differs to that of the substrate. The wafer will become convex or concave depending on a tensile or a compressive strain of the deposited layer. The wafer is heated and the bottom of the wafer is hotter than the top (the top of the wafer is cooled by the process gases). A formed vertical temperature gradient leads to the different thermal expansions of the top and bottom layers. The hotter bottom surface expands more, therefore, the concave curvature is formed. Too large concave or convex wafer curvature will create a gap between the wafer and susceptor. This induces a temperature variations on the wafer surface plane. Consequently, it will lead to the epilayer thickness non-uniformities [113]. For a convex wafer a center is expected to be cooler, while for a concave wafer the edges are cooler. A control of the wafer bowing is especially important for the InGaN based LED fabrication with a homogeneous wavelength emissivity, since the indium incorporation is very sensible to the temperature. This issue becomes more crucial for a large diameter wafers. Therefore, the *in-situ* curvature control plays an important role in the LEDs production.

A curvature radius R is obtained by measuring the distance between the spots of the reflected (from the wafer's surface) two parallel laser beams. The curvature K is expressed as an inverse of radius $K = \frac{1}{R}$. It consists of three components [114]:

$$\frac{1}{R} = \frac{1}{R^{\text{initial}}} + \frac{1}{R^{\text{thermal}}} + \frac{1}{R^{\text{growth}}} \,, \tag{5.7}$$

where $\frac{1}{R^{\text{initial}}}$ is an initial curvature of the wafer. The second curvature component induced by a thermal gradient is expressed as

$$\frac{1}{R^{\text{thermal}}}(T) = \alpha_{\text{s}} \frac{T_{\text{back}} - T_{\text{front}}}{d_{\text{s}}} \,, \tag{5.8}$$

where α_{s} is a substrate's thermal expansion coefficient and d_{s} is a substrate thickness. The temperature of the wafer's top and bottom are denoted as T_{front} and T_{back}, re-

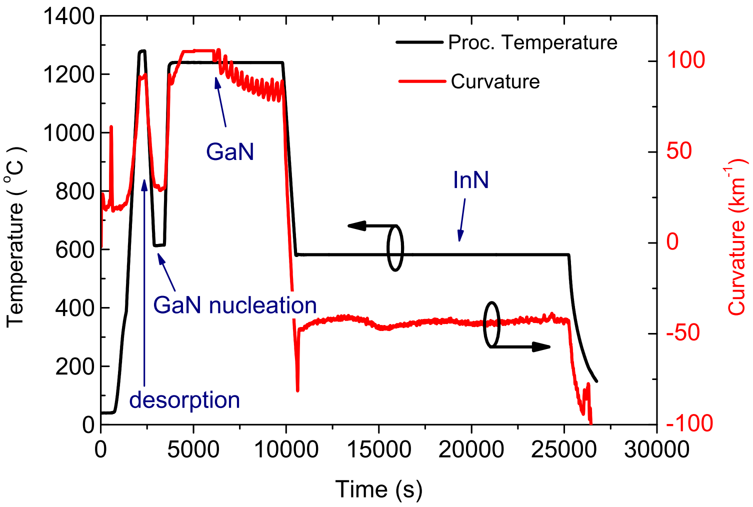

Figure 5.9: In-situ temperature and curvature measurements for the InN sample grown on GaN/sapphire template.

spectively. Finally, the third curvature component caused by the growth is expressed as

$$\frac{1}{R^{\mathrm{growth}}}(T) = -\frac{6d_{\mathrm{f}}}{d_{\mathrm{s}}^2 a_{\mathrm{s}}}\frac{M_{\mathrm{f}}\epsilon}{M_{\mathrm{s}}} \; , \tag{5.9}$$

where M_{f} and M_{s} is a biaxial elastic modulus of the film and substrate, respectively. A strain is denoted as ϵ and an epitaxial film thickness is denoted as d_f. The substrate's lattice parameter is expressed as a_s=$a_s(T)$=$a_s^{\mathrm{RT}}(1$+$\alpha_s(T$-$T_{\mathrm{RT}}))$, where T_{RT} is a room temperature. The approximation in Eq. 5.9 is valid only for $d_{\mathrm{f}}/d_{\mathrm{s}} \ll 1$. Fig. 5.9 shows a measured curvature for a grown InN film on the 2 inch sapphire wafer. At high annealing temperatures, reached during desorption process, the wafer curvature radius amounts to ~90 km^{-1}. This is caused due to a vertical thermal gradient in the wafer. At annealing temperature, the curvature is positive, therefore, the wafer becomes concave. When the wafer is cooled down to the GaN nucleation temperature, the curvature radius decreases to 30 km^{-1}. Again, when the temperature is increased to the temperature of GaN crystallization and GaN growth, the wafer curvature increases to ~75-100 km^{-1}. Finally, when the temperature is cooled down to the InN growth temperature, the curvature decreases to ≈-50 km^{-1}. It remains similar during all InN growth period. After cooling down to RT, the curvature still decreases to a huge ≈-115 km^{-1} value. This curvature corresponds to a large convex wafer bowing.

5.2 MBE epitaxial growth

In MBE systems, thin films are grown in the UHV environment on a heated substrate. The advantages of the MBE system is the growth of abrupt interfaces, a low contamination (UHV 10^{-11} Torr), an *in-situ* growth control by using a reflection high energy electron diffraction. The plasma-assisted (PA) MBE has also an advantage in growing high-quality InN and In-rich alloys at lower temperatures. In the PA-MBE setup, the nitrogen radicals are generated separately in a plasma source, while for the MOVPE the NH_3 pyrolysis on the wafer surface requires much higher temperatures. The group III sources (In, Ga, Al) used in the MBE system are in solid form and evaporated thermally from the effusion cells (Knudsen cells). A nitrogen source is an ammonia that thermally decomposes on the sample surface or a nitrogen radicals (for the PA-MBE setup) that are activated by RF source. Source elements are heated in Knudsen cells. The directed beams of molecules or atoms on the heated substrate are created. They react with the atomic or ionic nitrogen on the substrate surface and epilayer starts to grow. For n- or p-type doping the Si and Mg, respectively, are evaporated. Fig. 5.10 depicts a schematic MBE setup representation.

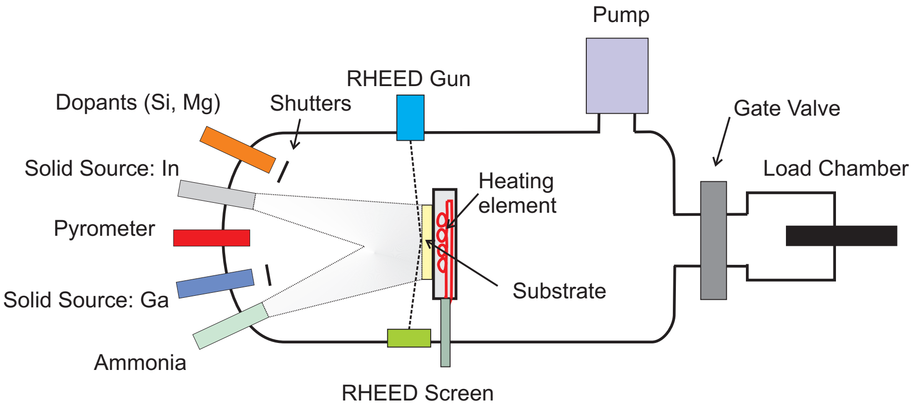

Figure 5.10: Schematic sketch of the MBE setup.

6 Optical properties of InN

In the first part of this chapter, optical properties of the (0001)-oriented unintentionally doped InN films grown on the Si(111) substrate with different nucleation/buffer layers will be compared to the results obtained for a film grown on a sapphire substrate. In previous studies, Schley *et al* [13] investigated wurtzite structure InN samples with carrier concentration in the range of 10^{18} cm^{-3} by using a spectroscopic ellipsometry and obtained an intrinsic strain-free band-gap of 0.675 eV. In this work, the InN films grown on the Si(111) exhibit one order of magnitude higher carrier concentration. The isotropic DFs are obtained in the range from 0.56 eV to 9.5 eV. Taking into consideration the strain influence on the band gap, the Burstein-Moss shift (BMS), and the band-gap renormalization (BGR), a strain-free intrinsic band gap will be estimated. Moreover, in the second part, the series of a carbon doped (0001)-oriented InN samples will be investigated. Recently, theoretical studies from Ramos *et al* [115] and Duan and Stampfl [116] claimed that a carbon is a possible p-type dopant in the InN material. The p-type InN doping is still critical and limiting device applications. So far, only Mg doping has shown evident p-type doping in the InN material [117, 118]. However, from the IR-SE and SE investigations presented here, it will be proved that a carbon doping leads to an increased electron concentration in the InN material. The isotropic DFs for the carbon doped InN samples will be presented in the extended energy range up to 17 eV. It will be shown that the characteristic features in the high-energy part of the imaginary part of the DF for different samples remain at the same energetic positions.

Figure 6.2 and 6.3 in this chapter are reprinted with permission from Sakalauskas *et al*, Physica Status Solidi A, Vol. 207, Page 1066, (2010). Copyright 2010, John Wiley & Sons, Inc.

6.1 Description of the investigated InN samples

Two InN samples grown by PA-MBE on the Si(111) substrates are denoted as A1 and A2, while the sample with a sapphire substrate (used as a reference) is denoted as B0. These samples were provided by dr. J. Grandal from ISOM, Technical University of

Madrid. The sample A1 consists of a 50 nm thick AlN nucleation layer grown on Si(111) substrate at a temperature of 890 °C under stoichiometric conditions. The InN layer of 390 nm thickness (as determined by SE) was directly grown on the nucleation layer under slightly N-rich condition at 450 °C. The InN film of the second sample (A2) was grown at the same conditions as sample A1. Additionally, sample A2 contains a GaN buffer layer of 250 nm thickness deposited under stoichiometric conditions at 730 °C. The InN layer thickness for sample A2 amounts to 412 nm. The third sample (B0) has the following multi-layer structure: A commercial Lumilog n-type GaN:Si (doping 2×10^{18} cm^{-3}) template layer of 3500 nm thickness grown by MOVPE on a sapphire substrate served as a template. PA-MBE started with the growth of a 80 nm thick GaN buffer layer under slightly Ga-rich conditions at 700 °C. Finally, the InN film of 688 nm thickness was deposited at 470 °C under slightly N-rich conditions.

For the purpose of a carbon doping analysis in the InN material, a series of $\sim$1 μm thick (0001)-oriented InN films were grown by PA-MBE on a sapphire/GaN templates. The carbon doped InN samples were provided by dr. A. Knübel from Fraunhofer IAF. A gaseous CBr_4 was used as a carbon doping source. A supply pressure of gaseous

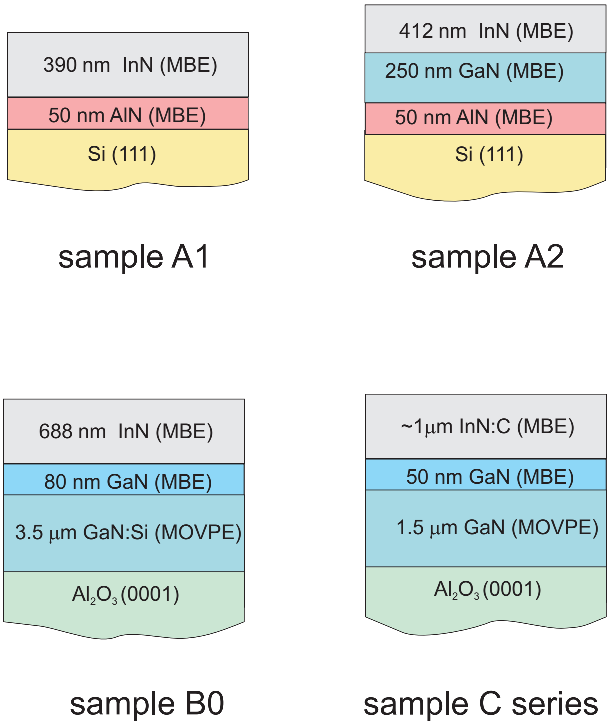

Figure 6.1: Schematic representation of the investigated InN samples.

CBr_4 was varied for different samples. The CBr_4 supply was varied by a mass flow controller. The investigated samples are labeled from C0 to C4 according with increase of carbon CBr_4 supply pressure in the samples. The sample labeled as C0 is the reference sample grown without CBr_4 source supply. The different CBr_4 pressures of 5, 20, 50, and 80 mTorr were used for the growth of samples labeled as C1, C2, C3, and C4, respectively. When the CBr_4 molecule reaches a hot substrate, it cracks and then carbon is incorporated in the InN material. The bromine is desorbed due to its relatively high vapour pressure, thus, its incorporation can be neglected. All C series samples were grown at 470 °C temperature. The flux ratios In/N for samples were chosen at slightly In-rich condition in order to get smooth surfaces. Due to the slightly In-rich growth conditions, the In droplets were accumulated on the the top of the sample surface. After the growth, the In droplets were etched using HCl.

6.2 Structural properties of the investigated InN samples

The structural properties were characterized by X-ray diffraction (XRD) measurements (provided by the growth groups). All samples exhibit (0001)-orientation, i.e., the c-axis oriented along the growth direction. Rocking curves of the symmetric (0002) reflections revealed a full width at half maximum (FWHM) of 917 (A1), 973 (A2), and 512 arcsec (B0). The FWHM values of the symmetric (0002) reflections for C0 to C4 samples were determined to be 331, 320, 288, 295, and 299 arcsec. The lattice parameters a and c were obtained from the reciprocal space maps. The structural characterization results of the investigated InN samples are summarized in Tab. 6.1. It is important to note that the InN film grown directly on the AlN nucleation layer (sample A1) experiences a

Sample	a (Å)	c (Å)	ϵ_{xx} (10^{-4})	ϵ_{zz} (10^{-4})	E_2^{H} (cm^{-1})	FWHM (0002) (arcsec)
A1	3.554	5.700	46.9	-6.5	490.6	917
A2	3.528	5.707	-27.3	6.0	491.8	973
B0	3.516	5.709	-62.2	9.8	494.8	512
C0	3.5259	5.7153	-33.36	20.34	-	331
C1	3.5237	5.7157	-39.57	21.04	-	320
C2	3.5267	5.7153	-31.09	20.34	-	288
C3	3.5266	5.7160	-31.38	21.56	-	295
C4	3.5208	5.7178	-47.77	24.72	-	299

Table 6.1: Structural parameters of the investigated InN samples.

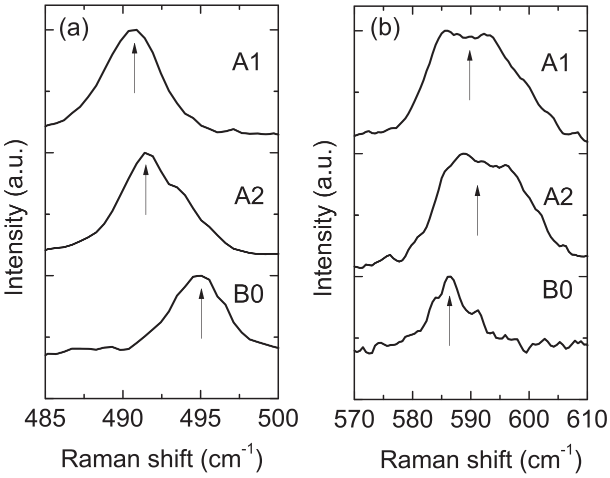

Figure 6.2: Raman spectra in the range of the E_2^{H} (a) and A_1(LO) (b) phonon modes.

tensile in-plain strain. The insertion of a GaN buffer leads to a compressive strain that is most pronounced if a sapphire substrate is used (sample B0).

In addition, the strongly different ϵ_{xx} values for the samples A1, A2, and B0 are emphasized by Raman studies; corresponding spectra are shown in Fig. 6.2. They were measured in backscattering geometry employing the 514 nm line of an argon ion laser. The symmetry-allowed E_2^{H} high mode in Fig. 6.2(a) shifts in agreement with other studies [119] to larger wavenumbers (see Tab. 6.1) with increasing in-plane compressive strain. It is expected that the longitudinal A_1(LO) phonon couples to the plasmons giving rise to mixed plasmon-LO-phonon excitations. As it can be seen in Fig. 6.2(b), a signal appears around 585 to 595 cm^{-1} which corresponds to the expected position of the unscreened A_1(LO) frequency. This observation is attributed to the scattering of virtual electron-hole pairs on structural defects of the lattice violating wave vector conservation [120]. The larger broadening of the feature for samples A1 and A2 indicates more defects than for sample B0.

6.3 Analysis of the unintentionally doped InN samples

The isotropic DFs of the investigated unintentionally doped InN samples A1, A2, and B0 in the photon energy range from 0.56 eV to 9.5 eV are presented in Figure 6.3(a), (b), and (c), respectively. The general shape is consistent with previous results [68, 121]. First of all, the attention will be focused at the DF around the band gap. The DFs around the band gap are compared for sample A1 and B0 in Fig. 6.4. The absorption onset (imaginary part of the DF-ε_2 around the gap) is blue-shifted for sample A1 with respect to the absorption onset of sample B0. Following the Kramers-Kronig relation, the real part of the DF (ε_1) for sample A1 is also shifted to higher energies. Applying the Eq. 3.22 presented in Chapter 3.2, the high-frequency dielectric constant ε_∞ for each sample was obtained and summarized in Tab. 6.2. The shift of the absorption edge towards higher energies lowers ε_∞, i.e., this quantity becomes sample dependent. In order to explain the obtained different absorption edge for the degenerated wurtzite structure InN samples and to evaluate the intrinsic strain-free band gap, the following effects must be taken into consideration:

- Band-gap renormalization;
- Burstein-Moss shift;
- Strain influence on the band gap.

The first effect, the band-gap renormalization, is caused due to many body interaction that induces a band-gap reduction. The second effect, the Burstein-Moss shift [122,123], is due to degenerated Fermi gas with Fermi level that is above the conduction band minimum. The third effect to be considered, is a strain influence on a band gap. The InN films are normally grown on a sapphire or Si wafers with different buffer layers. The different thermal expansion coefficients as well as lattice mismatch between a buffer and an InN epilayer lead to the tensile or compressive InN layer strain. All these effects

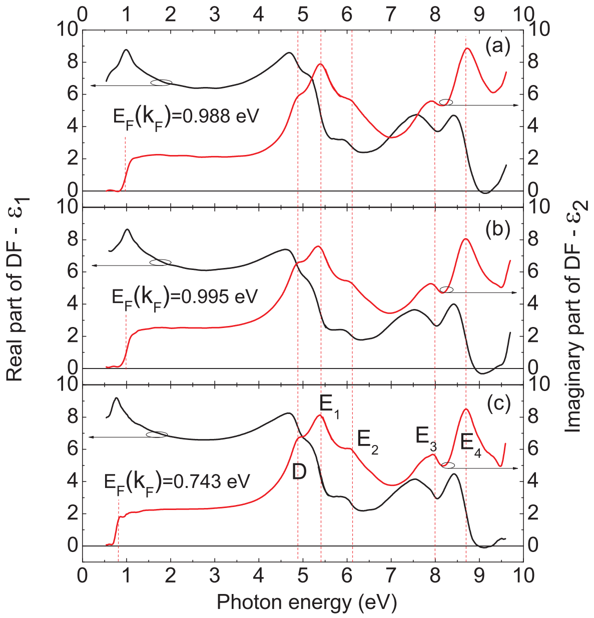

Figure 6.3: Isotropic DFs for samples A1 (a), A2 (b), and B0 (c).

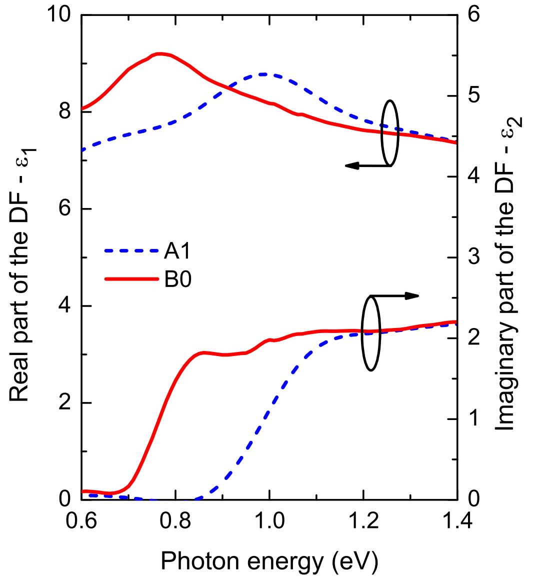

Figure 6.4: Isotropic DFs for sample A1 (dashed lines) and B0 (solid lines) around the gap region.

must be taken into consideration in order to obtain an intrinsic strain-free band-gap of InN material.

The following approach is used to estimate the band-gap renormalization. The presence of high electron concentrations in a narrow band-gap semiconductor leads to characteristic changes of the band structure around the Γ-point of the Brillouin zone. A carrier induced many-body interaction causes a shrinkage Δ_{BGR} of the intrinsic gap E_0, as denoted in Fig. 6.5. Recent studies [13, 121] emphasized the approach given in Ref. [11] for calculating Δ_{BGR}. Therefore, this approach is also applied in this work. The lower or *renormalized* gap is denoted by E_{ren} and indicated in Fig. 6.5. The gap renormalization enhances the non-parabolicity of the conduction band and, thus, the characteristic electron effective mass [121]. Wu *et al* [11] proposed to describe the band-gap renormalization shift Δ_{BGR} as the sum of electron-electron and electron-ion interaction contributions:

$$\Delta_{\mathrm{BGR}} = \Delta E_{\mathrm{e-e}} + \Delta E_{\mathrm{e-i}} \; . \tag{6.1}$$

The electron-electron interaction component is described as follows:

$$\Delta E_{\mathrm{e-e}} = -\frac{2e^2 k_{\mathrm{F}}}{4\pi^2 \varepsilon_0 \varepsilon_{\mathrm{r}}} - \frac{e^2 k_{\mathrm{TF}}}{8\pi \varepsilon_0 \varepsilon_{\mathrm{r}}} \left[1 - \frac{4}{\pi} \arctan\left(\frac{k_{\mathrm{F}}}{k_{\mathrm{TF}}} \right) \right] , \tag{6.2}$$

where $k_{\mathrm{F}} = (3\pi^2 N_{\mathrm{e}})^{1/3}$ is the Fermi wave-vector, $k_{\mathrm{TF}} = (k_{\mathrm{F}}/a_{\mathrm{B}})^{1/2}$ is the inverse of Thomas-Fermi screening length, and $a_{\mathrm{B}} = 0.53 \times 10^{-10} \varepsilon_{\mathrm{r}} m_0 / m_e^*(N_{\mathrm{e}})$ is the effective

Bohr-radius. For the effective mass $m_e^*(N_\mathrm{e})$ calculation, the approach proposed by Schley *et al* [121] is employed. Schley *et al* [121] considered the non-parabolic CB of InN and proposed to use an effective mass $m^*(N_\mathrm{e})$ described by the following equation [124]:

$$\frac{1}{m^*(N_\mathrm{e})} = \frac{1}{12\pi^3\hbar^2 N_\mathrm{e}} \int d\mathbf{k} \frac{\partial^2 E_\mathrm{c}(k)}{\partial k^2} f(E_\mathrm{c}) \;. \tag{6.3}$$

The integral runs from the renormalized gap E_ren over all occupied states in the CB. The Fermi-Dirac distribution function $f(E_\mathrm{c})$ at temperature T is described as

$$f(E_\mathrm{c}) = \frac{1}{1 + e^{\frac{E_\mathrm{c}(k) - E_\mathrm{F}}{k_\mathrm{B}T}}} \;, \tag{6.4}$$

where $E_\mathrm{c}(k) = \hbar\omega + E_\mathrm{v}(k)$ and $E_\mathrm{v}(k)$ are conduction and valence-band energy, respectively. Moreover, Schley *et al* [121] proposed to use the renormalized band-gap ($E_\mathrm{ren} = E_0 + \Delta_\mathrm{BGR}$) instead of intrinsic band-gap E_0 in the Kane's two-band $\mathbf{k}{\cdot}\mathbf{p}$ model [125]:

$$E_\mathrm{c}(k) = \frac{E_\mathrm{ren}}{2} + \frac{\hbar^2 k^2}{2m_0} + \frac{1}{2}\sqrt{E_\mathrm{ren}^2 + 4E_\mathrm{P}\frac{\hbar^2 k^2}{2m_0}} \;. \tag{6.5}$$

The second component that describes the electron-ion interaction is given by [11]

$$\Delta E_\mathrm{e-i} = -\frac{e^2 N_\mathrm{e}}{\varepsilon_0 \varepsilon_\mathrm{r} a_\mathrm{B} k_\mathrm{TF}^3} \;. \tag{6.6}$$

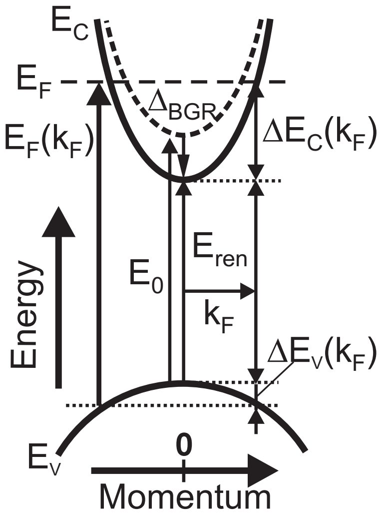

Figure 6.5: Schematic band diagram illustrating the influence of many-particle effects.

The Burstein-Moss shift can be explained as follows: In the degenerated semiconductors, the Fermi level E_{F}, which depends on the electron concentration N_{e}, is localized above the CBM ($\Delta E_{\mathrm{c}}(k_{\mathrm{F}})$) as it is depicted in Fig 6.5. The electron concentration is described with an integral

$$N_{\mathrm{e}} = \int\limits_{E_{\mathrm{ren}}}^{\infty} f(E_{\mathrm{c}}) D(E) dE \ , \tag{6.7}$$

where $D(E){=}\frac{[k(E)]^2}{\pi^2} \cdot \frac{dk(E)}{dE}$ is a density of states of CB electrons. Due to the conduction band filling, the absorption occurs near the Fermi wave-vector $\mathbf{k}_{\mathrm{F}}$. Under assumption that $T{=}0$ K, all states up to the Fermi level are occupied. According to the Pauli exclusion principle, the excitation of electrons from the valence band to the conduction band in the wave vector range $0 \leq \mathbf{k} \leq \mathbf{k}_{\mathrm{F}}$ is forbidden. With increasing a carrier concentration, an absorption onset shifts to higher energies and occurs at $E_{\mathrm{F}}(k_{\mathrm{F}})$. At the $\mathbf{k}_{\mathrm{F}}$, the valence band also makes a small contribution $\Delta E_{\mathrm{v}}(k_{\mathrm{F}})$ to the BMS ($\Delta E_{\mathrm{cv}}(k_{\mathrm{F}}) = \Delta E_{\mathrm{c}}(k_{\mathrm{F}}) - \Delta E_{\mathrm{v}}(k_{\mathrm{F}}) = E_{\mathrm{F}}(k_{\mathrm{F}}) - E_{\mathrm{ren}}$), as it is indicated in Fig. 6.5. The dispersion of the valence band is assumed to be parabolic and described with the effective mass of $m_h^* = 0.5\, m_0$ [76]:

$$E_{\mathrm{v}}(k) = \frac{\hbar^2 k^2}{2m_h^*} \ . \tag{6.8}$$

In order to estimate the intrinsic band gap of InN, a self-consistent problem (involving the IR-SE and the imaginary part of the DF-ε_2 data analysis) must be solved. The quantities E_{ren}, E_{F}, $\Delta E_{\mathrm{cv}}(k_{\mathrm{F}})$ and $m^*(N_{\mathrm{e}})$ depend on the carrier concentration. The carrier concentration is determined from the IR-SE analysis by employing the mid-infrared DF model (presented in Chapter 3, section 3.3) that gives the plasma frequency $\omega_{\mathrm{p},j}$ [124]:

$$\omega_{\mathrm{p},j}^2 = \frac{N_{\mathrm{e}} e^2}{\varepsilon_0 \varepsilon_{\infty,j} m^*(N_{\mathrm{e}})}, \tag{6.9}$$

where the averaged effective mass $m^*(N_{\mathrm{e}})$ is calculated from Eq. 6.3 and the high-frequency dielectric constant $\varepsilon_{\infty,j}$ is estimated from Eq. 3.22 (presented in Chapter 3). As it is evident from Eq. 6.9, only the ratio $N_{\mathrm{e}}/m^*(N_{\mathrm{e}})$ is determined from the plasma frequency. Therefore, the problem must be solved self consistently, the IR-SE data are analyzed together with the imaginary part of the DF (ε_2) around the band gap (absorption onset). The imaginary part of the DF is given by

$$\varepsilon_2(\hbar\omega) \sim \frac{1}{(\hbar\omega)^2} \frac{2}{(2\pi)^3} \int\limits_{\mathrm{BZ}} |P_{\mathrm{cv}}|^2 [1 - f(E_{\mathrm{c}})] \times \delta(E_{\mathrm{c}}(k) - E_{\mathrm{v}}(k) - \hbar\omega) \ d^3k. \tag{6.10}$$

Table 6.2: Obtained parameters for the investigated samples A1, A2, and B0.

Parameter	Sample A1	Sample A2	Sample B0
ω_{p} (cm^{-1})	2144	2088	766
N_{e} (cm^{-3})	3.1×10^{19}	3.0×10^{19}	3.5×10^{18}
$\varepsilon_{\infty}(N_e)$	6.75	6.88	7.52
$m^*(N_e)/m_0$	0.0898	0.0903	0.0717
$E_{\mathrm{F}}(k_{\mathrm{F}})$ (meV)	988	995	743
$\Delta E_{\mathrm{cv}}(k_{\mathrm{F}})$ (meV)	509	498	133
E_{ren} (meV)	479	497	610
$\Delta E_{\mathrm{strain}}$ (meV)	-26	15	34
Δ_{BGR} (meV)	-180	-178	-77
E_0 (meV)	685	660	653

The conduction band non-parabolicity is introduced by using Eq. 6.5. The integration takes place in reciprocal space (k) in the whole BZ. Figure 6.6(a) and (b) show the IR-SE measured (dashed black line) and fitted (solid red line) Ψ data for samples A1 and B0, respectively. Figure 6.7 displays the fitted ε_2 around the band gap with indicated E_{F} positions for samples A1 and B0, demonstrating a good agreement. After solving the self-consistent problem, the quantities N_e, ω_p, E_{ren}, $\Delta E_{\mathrm{cv}}(k_{\mathrm{F}})$, Δ_{BGR}, and $m^*(N_{\mathrm{e}})$ are determined, as listed in Tab. 6.2. The transition energy at Fermi wave-vector is found from

$$E_{\mathrm{F}}(k_{\mathrm{F}}) = E_{\mathrm{ren}} + \Delta E_{\mathrm{cv}}(k_{\mathrm{F}}), \tag{6.11}$$

where $\Delta E_{\mathrm{cv}}(k_{\mathrm{F}}) = \Delta E_{\mathrm{c}}(k_{\mathrm{F}}) - \Delta E_{\mathrm{v}}(k_{\mathrm{F}})$ denotes the BMS with the CB and VB component, ΔE_{c} and ΔE_{v}, respectively. Figure 6.8 shows the transition energy values at the Fermi wave vector $E_{\mathrm{F}}(k_{\mathrm{F}})$ (determined by solving a self-consistent problem) for samples A1, A2, and B0 (denoted by open triangles) and the theoretically calculated $E_{\mathrm{ren}}{=}E_0{+}\Delta_{\mathrm{BGR}}$ (with E_0=0.675 eV [13]) and $\mathrm{E_F}{=}E_{\mathrm{ren}}{+}\Delta E_{\mathrm{cv}}(k_{\mathrm{F}})$ values as a function of carrier concentration. The obtained $E_{\mathrm{F}}(k_{\mathrm{F}})$ match well with the calculated values.

The determined carrier concentrations are 3.1×10^{19}, 3×10^{19} and 3.5×10^{18} cm^{-3} for samples A1, A2, and B0, respectively, as listed in Tab. 6.2. Positively charged nitrogen vacancies along dislocations [126] and point defects [127] are considered as sources of high carrier concentration in the InN material. Consistent with the Raman data (presented in section 6.2), a larger density of those defects for both InN films on Si substrate seems likely leading to the one order of magnitude higher electron concentration.

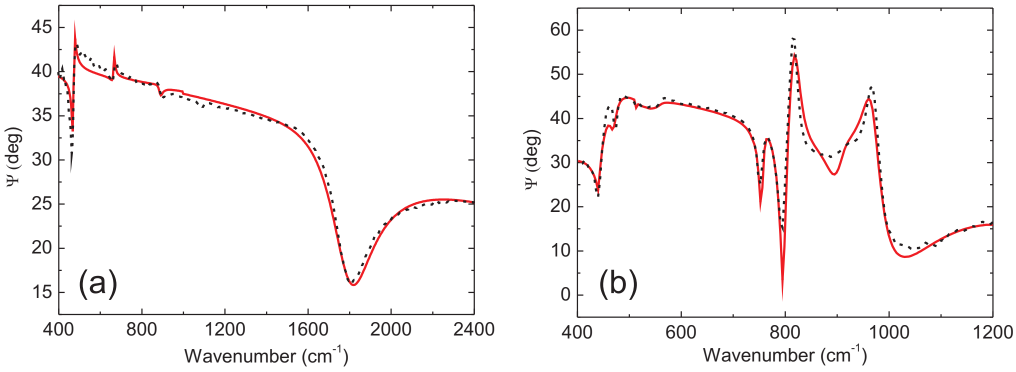

Figure 6.6: IR-SE experimental and fitted Ψ values for sample A1 (a) and sample B0 (b).

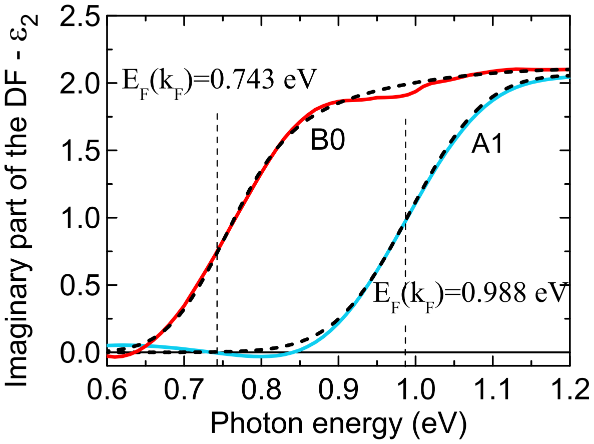

Figure 6.7: Fitted imaginary parts of the DF (ε_2) around the gap for samples A1 and B0.

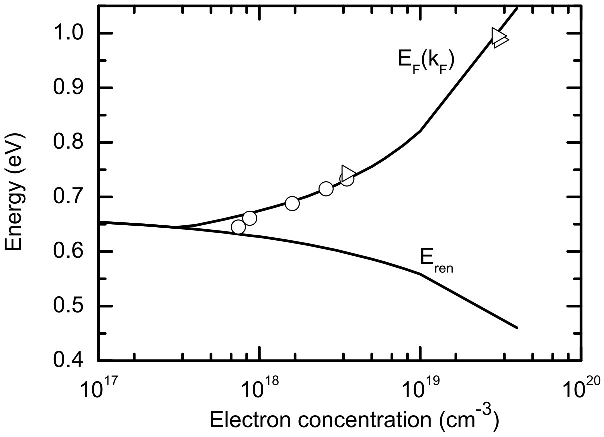

Figure 6.8: Calculated (black lines) $E_\mathrm{F}(k_\mathrm{F})$ and E_ren as a function of carrier concentration. Experimentally obtained $E_\mathrm{F}(k_\mathrm{F})$ values for the investigated unintentionally doped and carbon doped samples are denoted by open triangles and open circles, respectively.

The knowledge of E_{ren} and Δ_{BGR} allows now to estimate the intrinsic strain-free band gap that is given by

$$E_0 = E_{\text{ren}} - \Delta_{\text{BGR}} - \Delta E_{\text{strain}}, \tag{6.12}$$

The term ΔE_{strain} accounts for the band-gap energy shift due to the in-plain biaxial strain (ϵ_{xx}) and is calculated by applying the $\mathbf{k}\cdot\mathbf{p}$ model presented in Chapter 2. The obtained intrinsic strain-free band gaps are 685, 660, and 653 meV for samples A1, A2, and B0, respectively.

In addition to the gap structure, the characteristic features (peaks and shoulders) are resolved in the high-energy part of the DF, as observed in Fig. 6.3. This confirms a good crystalline quality of the InN films. Figure 6.9 compares the imaginary parts of the isotropic DFs of the investigated samples (represented by red curves) together with the imaginary part of the isotropic DF of the wurtzite structure InN sample (represented by dotted curve) from Ref. [121]. The vertical dashed lines indicate the positions of the critical points of the band structure (their energies amount to 4.81, 5.38, 6.12, 7.95, and 8.57 eV and are denoted as D, E_1, E_2, E_3, and E_4, respectively, as was determined in Ref. [121]). Despite the different strain present in the InN films, no pronounced shift of the characteristic features in the imaginary part of the DF (i.e., peaks or shoulders) is observed.

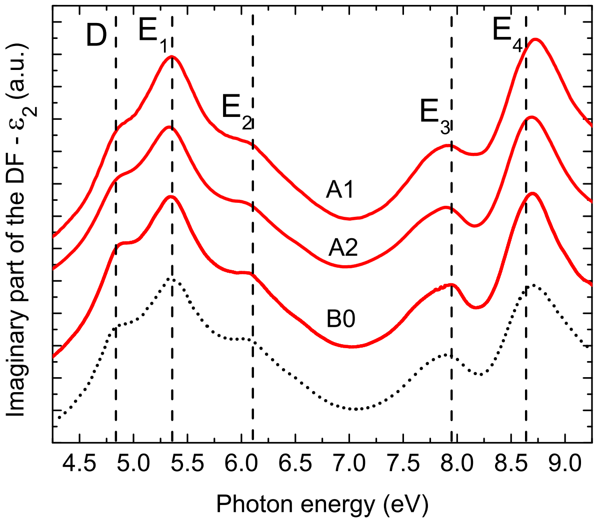

Figure 6.9: Imaginary part of the isotropic DFs in the high-energy range obtained for samples A1, A2 and B0. For comparison, the dotted curve represents the imaginary part of the isotropic DF for the wurtzite structure InN sample from Ref. [121]. The vertical dashed lines indicate the positions of the critical points of the band structure, as it was determined from Ref. [121]. For clarity, the curves are vertically shifted from each other.

6.4 Analysis of the carbon doped InN samples

Secondary ion mass spectroscopy (SIMS) and ion channeling characterizations were conducted at Evans Analytical Group to determine the carbon concentration (N_C) and the percentage of the substitutional carbon incorporation in the InN lattice, respectively. Table 6.3 lists the $\mathrm{CBr_4}$ pressure, the obtained carbon concentration and the content of the substitutional carbon in the InN lattice for samples C0, C1, C2, and C4. The SIMS results indicate that the increased $\mathrm{CBr_4}$ pressure increases a carbon concentration (N_C). For example, the sample C4 grown with $\mathrm{CBr_4}$ pressure of 80 mTorr has one order of magnitude larger carbon concentration compared to the sample C1 with $\mathrm{CBr_4}$ pressure of 20 mTorr. The ion channeling analysis has shown that $\sim$90% of carbon atoms are incorporated on substitutional InN lattice sites.

The isotropic DFs around the band gap for the investigated carbon doped samples are presented in Fig. 6.10(a). It is observed that for samples with increased carbon dopant source ($\mathrm{CBr_4}$) pressure, the absorption onset shifts to higher energies, indicating an increasing electron concentration. In addition, the SE ellipsometry measurements were performed in the extended energy range up to 17 eV for samples C0, C2, and C4 and their determined isotropic DFs are shown in Fig. 6.10(b). The shape of the DFs above the band gap for all samples have a similar character. The characteristic peaks and shoulders are observed in the imaginary part of the DF energy range 4-12 eV. These characteristic peaks and shoulders correspond to the critical points of the band structure denoted as D, E_1, E_2, E_3, E_4, E_5, and E_6 in Fig. 6.10(b). In the energy range above 12 eV, only a plateau with a decreasing slope is observed. The imaginary parts of the DFs (ε_2) in the range 4.5-9.5 eV for samples C0, C2, C4, and A1 (investigated in previous section) are compared in Fig. 6.11. The vertical dashed lines in Fig. 6.11 indicate the positions of the critical points D, E_1, E_2, E_3, and E_4, as determined in Ref. [121]. No significant shift of the characteristic peaks in the imaginary part of the DF is observed for different samples.

Sample	$\mathrm{CBr_4}$ pressure (mTorr)	N_C ($\mathrm{cm^{-3}}$)	Substitutional carbon (%)
C0	0	$3\text{-}4\times10^{17}$	88
C1	20	$4\text{-}5\times10^{17}$	92
C2	50	$1\text{-}2\times10^{18}$	92
C4	80	$3\text{-}4\times10^{18}$	93

Table 6.3: Carbon bulk concentration N_C and the percentage of carbon substitutionals in the InN matrix obtained for carbon doped InN samples C0, C1, C2, and C4.

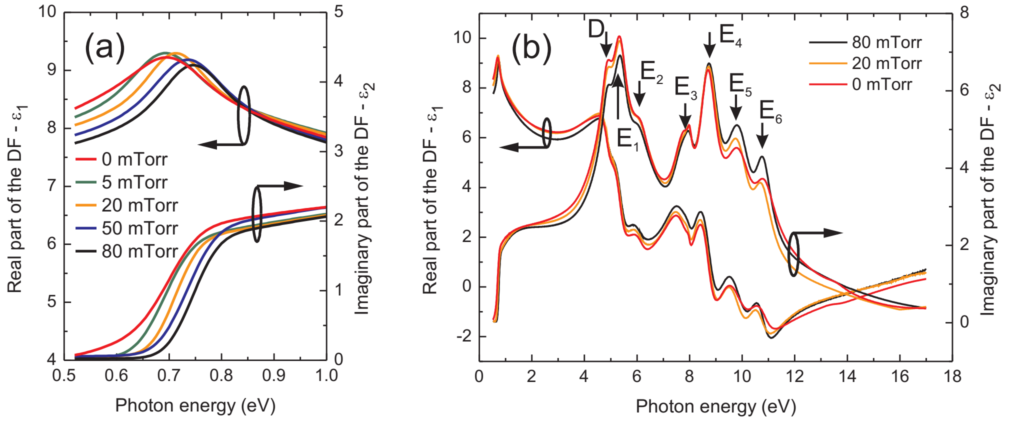

Figure 6.10: Isotropic DFs near the band-gap region (a) and in the extended energy range up to 17 eV (b) extracted for the carbon doped InN samples.

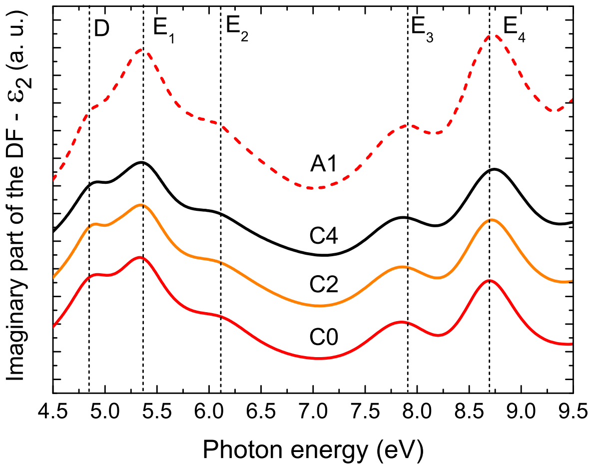

Figure 6.11: Imaginary parts of the DFs for C0, C2, and C4 samples together with the sample A1 used for comparison. For clarity, the DFs were shifted in the vertical direction. The vertical dashed lines indicate the positions of the critical points of the band structure determined in Ref. [121].

After solving the self-consistent problem (as presented in previous section), the electron concentration and the intrinsic strain-free band-gap values (listed in Tab. 6.4) were estimated for the investigated carbon doped samples. According to the summarized results in Tab. 6.4, the electron plasma frequency (ω_p) and the electron concentration (N_e) increase for samples with increasing carbon dopant source (CBr_4) pressure during the growth process. As it was explained in previous section, the self-consistent problem consists of the IR-SE and the absorption onset (ε_2 around the band gap) analysis. Figures 6.12(a)-(e) show the IR-SE measured experimental (dashed black curve) and fitted (solid red curve) Ψ data. Figures 6.12(f)-(j) depict the calculated (solid red curve) and

Table 6.4: Obtained parameters for the investigated carbon doped InN samples.

Parameter	Sample C0	Sample C1	Sample C2	Sample C3	Sample C4
CBr_4 (mTorr)	0	5	20	50	80
ω_p (cm^{-1})	363	391	519	677	783
N_e (cm^{-3})	7.4×10^{17}	8.7×10^{17}	1.6×10^{18}	2.6×10^{18}	3.5×10^{18}
$\varepsilon_\infty(N_e)$	7.64	7.63	7.60	7.40	7.28
$m^*(N_e)/m_0$	0.066	0.067	0.068	0.070	0.071
$E_\mathrm{F}(k_\mathrm{F})$ (meV)	645	661	688	715	733
$\Delta E_\mathrm{cv}(k_\mathrm{F})$ (meV)	35	42	73	110	135
E_ren (meV)	610	619	615	605	598
ΔE_strain (meV)	19	22	17	18	27
Δ_BGR (meV)	-43	-45	-56	-70	-77
E_0 (meV)	634	642	654	657	648

experimental (dashed black curve) ε_2. Fig 6.13 shows an electron concentration as a function of CBr_4 pressure. One can observe a linear increase of the electron concentration by increasing the CBr_4 pressure. Refering to the SIMS data presented in Tab. 6.3, one can conclude that the carbon doping in the InN material causes an increase of electron concentration. This experimental result contradicts the results obtained in the theoretical studies from Ramos *et al* [115] and Duan and Stampfl [116].

In analogy to the InN samples investigated in the previous section, the transition energies at the Fermi wave-vector $E_\mathrm{F}(k_\mathrm{F})$ obtained from the self-consistent problem solution and denoted by open circles are compared with the calculated $E_\mathrm{F}(k_\mathrm{F})$ values in Fig. 6.8. One can observe that sample C0 has smaller $E_\mathrm{F}(k_\mathrm{F})$ value and deviates from the theoretically calculated curve. If one compares the absorption onsets for all samples in Fig. 6.10(a), one can see that the absorption onset is much broader for sample C0. In Chapter 4 the ellipsometric data modelling example was presented for sample C0. It was shown that a good ellipsometric data modelling for sample C0 was obtained by using a multilayer optical model with an interlayer containing the Drude oscillator that accounts for the effects of an interface electron accumulation layer. Perhaps, the sample with a very low bulk electron concentration and with the present high carrier concentration at the surface or interface prohibits to obtain an accurate absorption onset leading to lower E_F values and, consequently, to lower intrinsic band-gap E_0. The intrinsic strain-free band gap values were evaluated to be 634, 642, 654, 657, and 648 meV, for samples C0, C1, C2, C3, and C4, respectively.

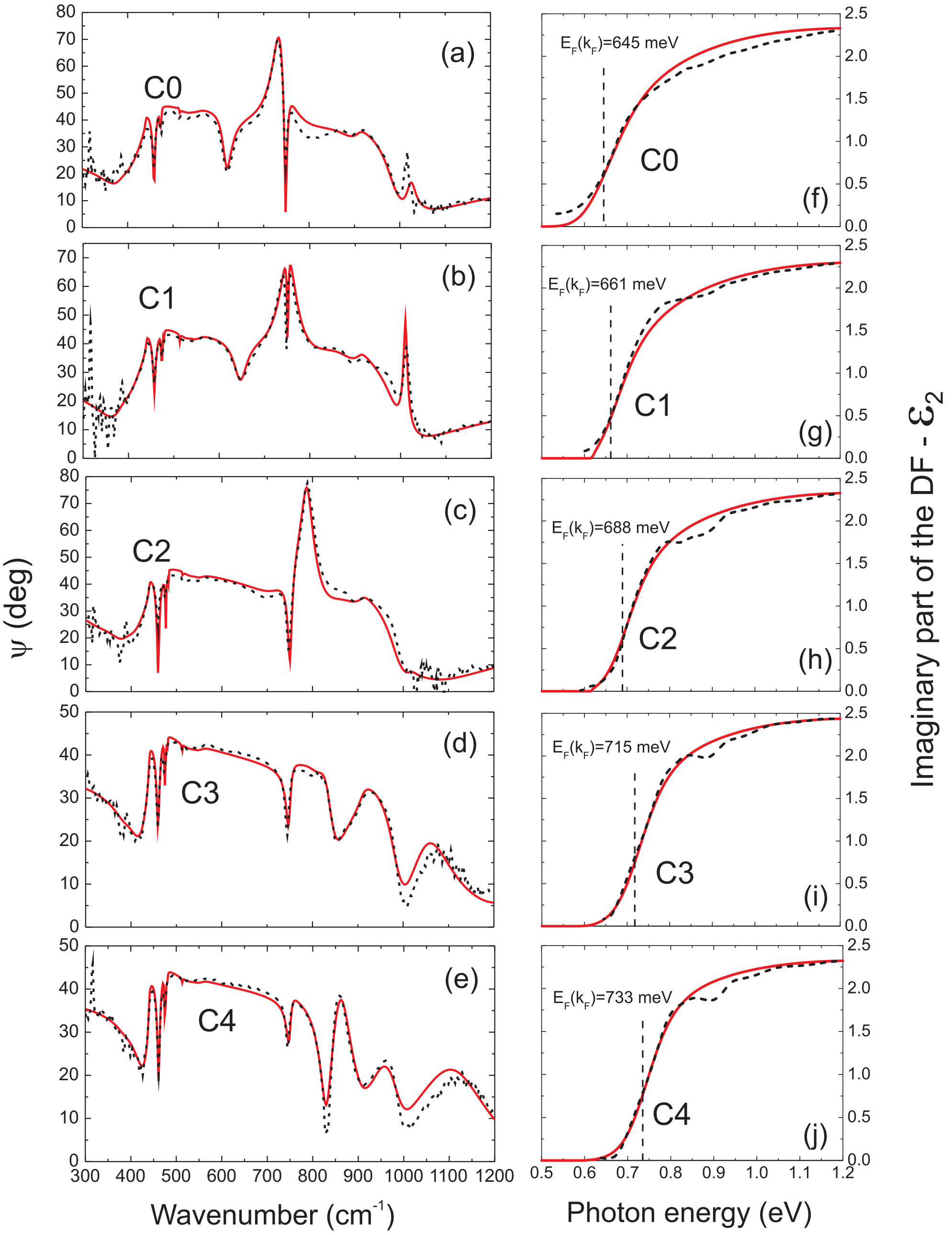

Figure 6.12: IR-SE measured (dashed black curve) and fitted (solid red curve) Ψ data (a)-(e) for samples C0-C4, respectively. Measured at angle of incidence of 65.2 deg. Experimental (dashed black curve) and calculated (solid red curve) imaginary part of the DF - ε_2 (f)-(j) for samples C0-C4, respectively

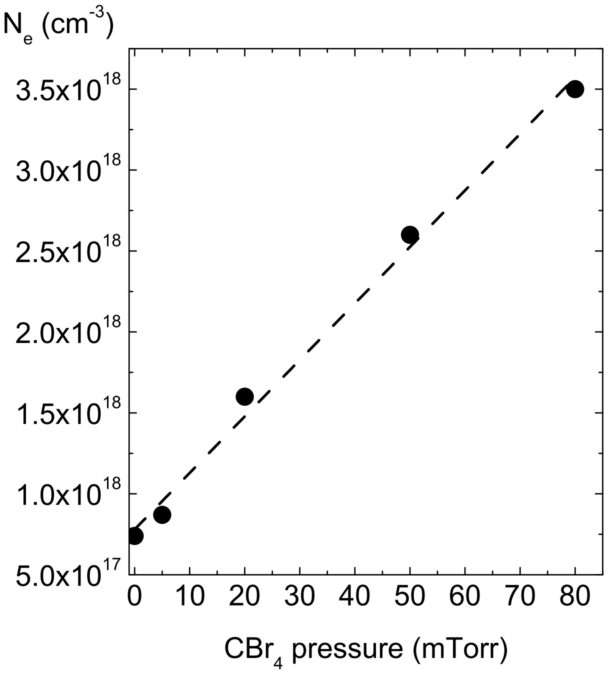

Figure 6.13: Electron concentration as a function of CBr_4 pressure. The dashed line represents a linear fit of the experimental data.

6.5 Summary of Chapter 6

The (0001)-oriented InN films sample series grown on Si(111) substrate and carbon doped InN sample series were investigated by IR-SE and SE. After solving the self-consistent problem that includes the IR-SE data analysis and the absorption onset fitting, the carrier concentrations were determined in the investigated samples. Taking into account the effects of the Burstein-Moss shift and the band-gap renormalization as well as a strain influence, the strain-free intrinsic band gap of InN was evaluated to be $\sim$0.65 eV. It was shown that by increasing the carbon dopant CBr_4 pressure during the MBE growth process and, consequently, the carbon concentration in the InN material, the electron concentration increases.

7 Optical properties of InGaN alloys

In this chapter, two sets of the (0001)-oriented $\mathrm{In}_x\mathrm{Ga}_{1-x}\mathrm{N}$ samples with $0.15<x<0.19$ grown by MBE and MOVPE will be investigated. The isotropic DFs are determined in the energy range from 1 up to 10 eV and the analytical forms of the DFs are presented. Moreover, the sample with an In content of x=15.2% will be investigated in the extended photon energy up to 18 eV. The band gaps of the investigated InGaN films are estimated from the fit of the analytical model to the experimental DFs. The strain induced shift is claculated by applying the $\mathbf{k}\cdot\mathbf{p}$ formalism. In the previous studies of Schley *et al* [121], the band gaps were determined for In-rich InGaN alloys and the band-gap bowing parameter of 1.72 eV was estimated. By combining the latter results and the results obtained in this work for the Ga-rich samples, the strain-free band gap and high-energy inter-band transition bowing parameters will be proposed. The obtained experimental bowing curve is in a good agreement with the *ab initio* data [128].

Fig. 7.3 and Fig. 7.5 in this chapter are reprinted with permission from Sakalauskas *et al*, Physica Status Solidi B, Vol. 249, Page 485, (2012). Copyright 2012, John Wiley & Sons, Inc.

7.1 Description of the investigated InGaN samples

The MOVPE grown InGaN samples provided by Ö. Tuna (AIXTRON SE) are denoted as SX1 and SX2. The InGaN films were deposited on a GaN/sapphire template at 600 mbar pressure with TMIn/TMGa ratio of 3 at 740 C° and 726 C° for samples SX1 and SX2, respectively. The RF-MBE grown InGaN samples provided by A. Kraus (TU Braunschweig) are denoted as SB1 and SB2. A sapphire substrate is used with the MOVPE grown GaN and $\mathrm{Al}_{0.05}\mathrm{Ga}_{0.95}\mathrm{N}$ buffer layers, with thicknesses of 2 μm and 1.2 μm, respectively. Prior to the InGaN epitaxy, a GaN buffer layer of approximately 15 nm thickness was deposited in order to prepare a reproducible surface. The growth details for SB series samples can be found elsewhere [9]. The InGaN layer thicknesses are 47 nm, 49 nm, 56 nm, and 50 nm for samples SX1, SX2, SB1, and SB2, respectively, as determined by SE. The in-plane lattice parameters obtained from XRD measurements are a=3.2249 Å and a=3.2311 Å for sample SX1 and SX2, respectively. The GaN buffer lattice parameter is a^{GaN}=3.186 Å, which yields a partial relaxation of 10% and 12% for samples SX1 and SX2, respectively. The InGaN layers for samples SB1 and SB2, with a=3.1847 Å and a=3.1844 Å, respectively, are almost fully strained on GaN buffer with a^{GaN}=3.185 Å. The In content in the InGaN alloys was estimated from the HRXRD measurements. A schematic representation of the investigated samples is demonstrated in Fig. 7.1.

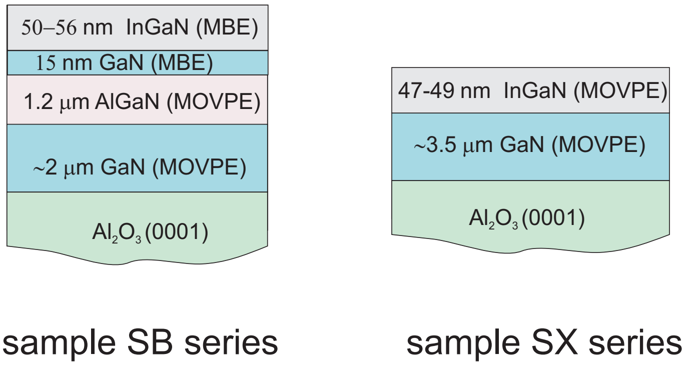

Figure 7.1: Schematic representation of the investigated InGaN samples.

7.2 InGaN dielectric function and its analytical representation

Figure 7.2(a) and (b) show real and imaginary parts of the isotropic DF, respectively, obtained in the photon energy range 1-18 eV at RT for sample SB1 (15.2% In content) together with a GaN ordinary DF (used for comparison). An absorption onset (imaginary part of the DF around the band gap) for the SB1 sample is red shifted with respect to a GaN. Due to the Kramers-Kronig relation, the ε_1 peak also shifts to lower energies and, therefore, the ε_1 values below the band gap (or refractive index $n = \sqrt{\varepsilon_1}$) are higher in comparison with GaN. At higher photon energies the characteristic peaks in the imaginary part of the DF are observed and they are denoted as E_1, E_2, E_3, E_4, and E_5, at the photon energy positions 6.6, 7.6, 8.7, 10.8, and 12.6 eV, respectively. As it was already mentioned in Chapter 2, the energetic positions of the characteristic peaks correspond to the inter-band transitions occurring near the van Hove singularities in the JDOS. The high-energy inter-band transitions E_1, E_2, and E_3 are red shifted, while E_4 and E_5 remain almost at the same position with respect to GaN.

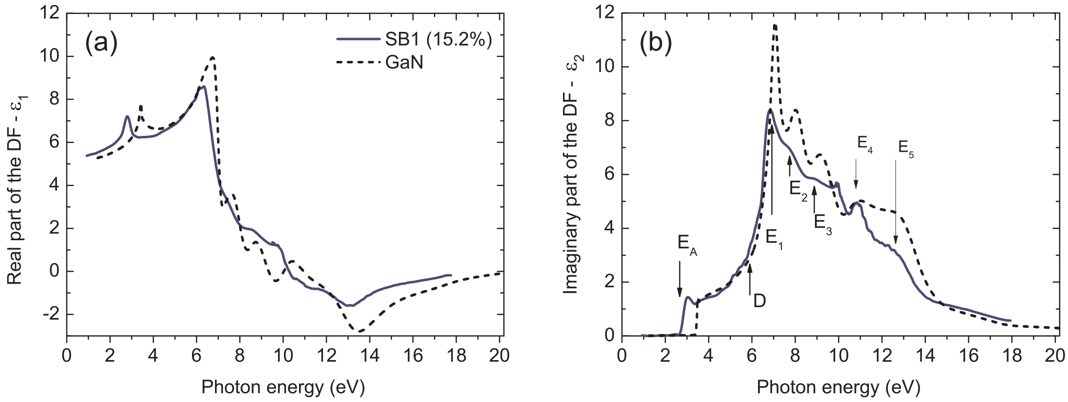

Figure 7.2: Real (a) and imaginary (b) parts of the isotropic DF for sample SB1. The GaN DF [98] (dashed black lines) is shown for comparison.

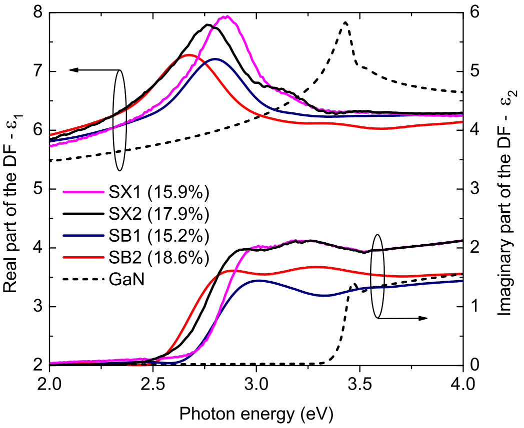

Figure 7.3: DFs around the band gap for the investigated samples.

Figure 7.3 shows the DFs around the band gap for the investigated InGaN samples and GaN for comparison. The absorption onset red shifts with increasing In content. By fitting the obtained experimental DFs with the analytical model (described by Eq. 3.18 and Eq. 3.21 in Chapter 3.2), the band-gap values E_A of the investigated samples were estimated. The obtained band-gap values E_A (energy splitting between the uppermost valence band with Γ_v^9 symmetry and the Γ_c^7 conduction band) are listed in Table 7.2. The analytical form of the InGaN DFs together with the experimental DFs are plotted in Figure 7.4(a) and (b) for samples SB1 and SB2, respectively. The DF analytical model parameters are listed in Table 7.1.

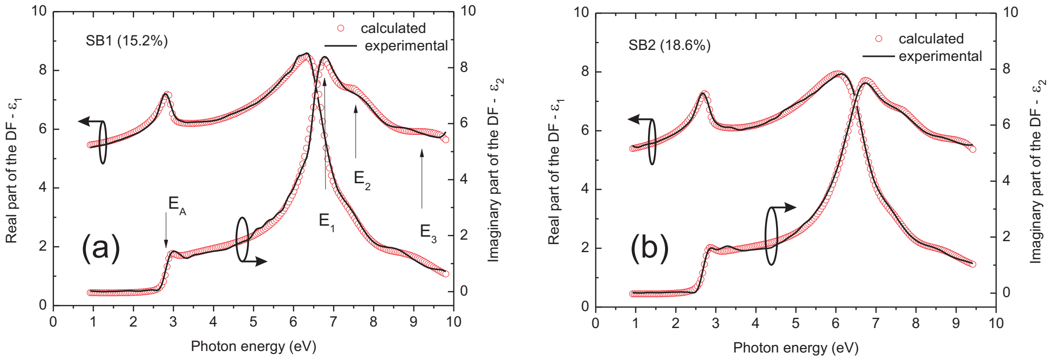

Figure 7.4: Experimental DFs (black lines) together with the analytical forms of the DFs (red circles) for samples SB1 (a) and SB2 (b).

Table 7.1: Fitting parameters for the DF analytical model.

Parameter	SB1 (15.2 %)	SB2 (18.6 %)
A_0	1.21	1.42
A_1 (eV^2)	17.49	44.69
A_2 (eV^2)	73.73	32.50
A_3 (eV^2)	135.14	90.66
$A_{\rm BS}$ (eV^2)	0.30	0.38
$A_{\rm CS}$ (eV)	0.65	0.75
$A_{\rm P}$ (eV)	102.4	100.02
E_1 (eV)	6.71	6.69
E_2 (eV)	7.45	7.70
E_3 (eV)	9.67	9.24
$E_{\rm A}$ (eV)	2.91	2.79
$E_{\rm B}$ (eV)	E_A+0.013	E_A+0.013
$E_{\rm P}$ (eV)	14.25	13.38
Γ_0 (eV)	0.047	0.058
Γ_1 (eV)	0.74	1.41
Γ_2 (eV)	2.37	1.77
Γ_3 (eV)	3.96	3.05
$\Gamma_{\rm BS}$(eV)	0.25	0.29
$\Gamma_{\rm CS}$ (eV)	0.13	0.13
R (meV)	12	15
b	-1.38	-1.17

7.3 InGaN band-gap and high-energy inter-band transition bowing parameters

First of all, the strain influence on the band gap must be taken into consideration before evaluating the bowing parameter. The $\mathbf{k} \cdot \mathbf{p}$ method (described in Chapter 2) was used to calculate the strain induced band-gap shift $\Delta E_{\mathrm{A}}^{\mathrm{strain}}$. The SE measured InGaN layer thickness d_{thick}, the estimated in-plane strain values ϵ_{xx}, the calculated strain induced energy shift $\Delta E_{\mathrm{A}}^{\mathrm{strain}}$, and strain-free band-gap values $E_{\mathrm{A}}^{\mathrm{relax}}$ are listed in Table 7.2. The large in-plane strain values ϵ_{xx} and, consequently, large strain induced band-gap shifts ($\Delta E_{\mathrm{A}}^{\mathrm{strain}}$) are obtained for fully pseudomorphically grown SB sample series. Figure 7.5(a) shows the extracted $E_{\mathrm{A}}^{\mathrm{relax}}$ values for the investigated InGaN samples in this work together with the experimental data for In-rich InGaN from Ref. [121]. Employing the end-point values of $\mathrm{E}_{\mathrm{A}}^{\mathrm{InN}}$=0.675 eV [13] and $\mathrm{E}_{\mathrm{A}}^{\mathrm{GaN}}$=3.435 eV [24], the compositional dependence can be represented by a strain-free band-gap bowing parameter of 1.65±0.07 eV. In addition, the obtained experimental strain-corrected band-gap values are compared with the strain-corrected band-gap values from the work of Mc-

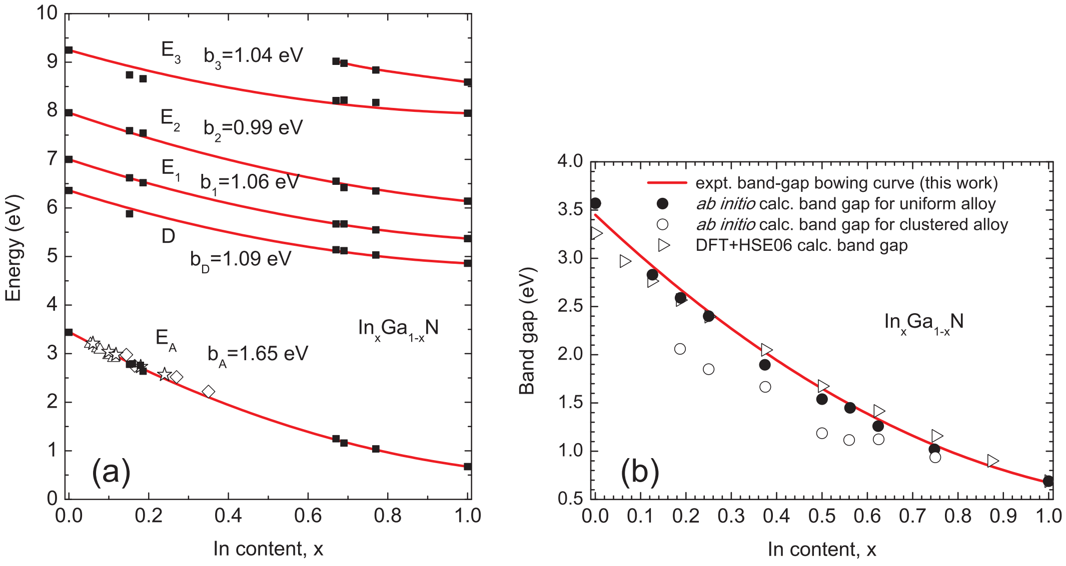

Figure 7.5: (a) Experimentally determined band-gap and high-energy inter-band transition energies (full squares) as a function of In content (x). The data points for In-rich InGaN alloys were taken from Ref. [121]. For comparison, the experimental band-gap values for 0.05<x<0.36 were taken from the Ref. [129] (triangles), Ref. [130] (stars), and Ref. [131] (diamonds). (b) the experimental band-gap bowing curve is compared with the *ab initio* data for uniform (full circles) and clustered (open circles) alloy from Ref. [128] as well as with the DFT+HSE06 calculated band gap (open trinagles) from Ref. [132].

Cluskey *et al.* [129], Pereira *et al.* [130], and Kudrawiec *et al.* [131], as it is indicated in Fig. 7.5(a) by triangle, star, and diamond symbols, respectively. All the compared experimental data show good agreement with the obtained experimental bowing curve.

The experimental bowing curve determined in this work is consistent with the *ab initio* calculated band-gap values for uniform (not clustered) InGaN alloys [128], as demonstrated in Fig. 7.5(b) (full circles). The calculated values for clustered materials (indicated with open circles in Fig. 7.5) are always much lower than for an uniform distribution. In addition, the band-gap values (expressed with respect to the average valence band) from the the work of Moses *et al.* [132], obtained by using the density functional theory (DFT) calculations with the HSE06 hybrid exchange-correlation functional, are presented by triangles in Figure 7.5. The DFT+HSE06 calculations show good agreement in the In-rich region, while in the Ga-rich region the theoretical values are slightly below the experimental bowing curve, since the GaN band gap of 3.23 eV was used in the DFT calculations. Moses *et al.* [132] proposed to use a compositional dependent bowing parameter and made calculations at *specific* alloy compositions: b=2.29 eV for x=6.125% and b=1.79 eV at x=12.5%. If one calculates the band-gap values for the same alloy compositions x=6.125% and x=12.5%, by employing the mentioned theoretically calculated bowing parameters (b=2.29 eV and b=1.79 eV) and using the end-point values of $\mathrm{E}_{\mathrm{A}}^{\mathrm{InN}}$=0.675 eV [13] and $\mathrm{E}_{\mathrm{A}}^{\mathrm{GaN}}$=3.435 eV [24], and compares the values calculated with the experimental bowing parameter 1.65 eV, one can observe that the diffence between the latter is only 37 meV and 15 meV, respectively. With the knowledge that GaN exciton binding energy is ~20 meV [133], one can make an error within 20 meV for Ga-rich InGaN alloy by estimating experimentally the excitonic transition and not the band-to-band transition. The composition estimation in the alloy, the strain-correction estimation of the band gap can also contribute to the experimental error of several mili-electronvolts.

However, very often the InGaN epilayers are grown fully-strained on the GaN. Therefore, it is useful to know the band gap for the fully strained material. Assum-

Sample	d_{thick} nm	ϵ_{xx} $\times10^{-2}$	E_{A} (eV)	$\Delta E_{\text{A}}^{\text{strain}}$ (meV)	$E_{\text{A}}^{\text{relax}}$ (eV)
SX1 (15.9%)	47	-0.61	2.84	46	2.79
SX2 (17.9%)	49	-0.64	2.81	47	2.76
SB1 (15.2%)	56	-1.77	2.91	132	2.78
SB2 (18.6%)	50	-2.08	2.79	154	2.64

Table 7.2: InGaN sample layer thickness in-plane strain ϵ_{xx}, band gap E_{A} determined by SE, strain induced energy shift $\Delta E_{\text{A}}^{\text{strain}}$, and strain-free band-gap value $E_{\text{A}}^{\text{relax}}$.

ing that GaN buffer layer is fully relaxed (a_0^{GaN}=3.1894 Å [74]) and InGaN epilayer with $0 < x < 0.2$ is fully strained on the GaN, the band gap is calculated as

$$E_{\mathrm{A}}^{\mathrm{strain}} = E_{\mathrm{A}}^{\mathrm{relax}} + 0.79 \times x, \tag{7.1}$$

where $E_{\mathrm{A}}^{\mathrm{relax}} = 0.675 \times x + 3.435 \times (1 - x) - 1.65 \times x \times (1 - x)$.

The high-energy inter-band transitions were evaluated by using the third derivative method as described in Ref. [134]. Figure 7.6 shows experimental (solid lines) and fitted (open circles) third derivative of $\varepsilon_1 \times E^2$, $\varepsilon_2 \times E^2$ for sample SB1. The high-energy inter-band transitions obtained from the third derivative method for sample SB1(SB2) were obtained to be 6.62 eV(6.52 eV), 7.59 eV(7.54 eV), and 8.74 eV(8.66 eV) for transitions E_1, E_2, and E_3, respectively. In addition, the transition D for sample SB1 was obtained to be 5.88 eV. The transition energies E_1 and E_2 obtained from the third derivative method are in a good agreement with a values obtained from the DF model fitting (listed in Tab. 7.1). The high-energy inter-band transitions bowing parameters were estimated to be 1.09, 1.06, 0.99, and 1.04 eV for transitions D, E_1, E_2, and E_3, respectively. As it was demonstrated in Chapter 6 for the InN material, no strain induced shift is observed on the high-energy inter-band transitions.

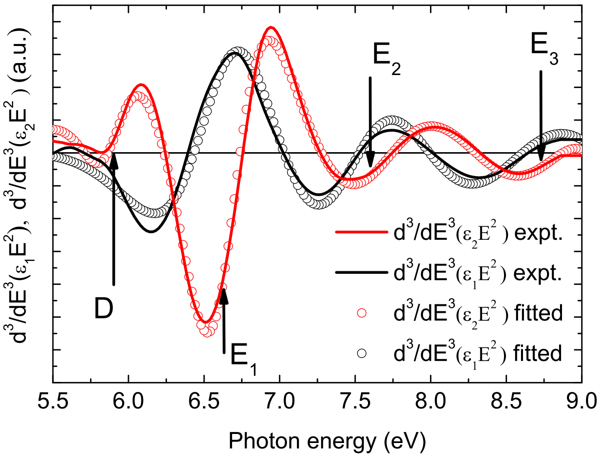

Figure 7.6: Experimental (solid lines) and fitted (open circles) third derivative of $\varepsilon_1 \times E^2$ and $\varepsilon_2 \times E^2$ for sample SB1.

Moreover, the PL measurements were conducted by using an excitation wavelength of 337.1 nm and excitation power of 200 kW/cm^2 on the samples SX1 and SX2 at room temperature. The PL data were provided by the research group of prof. G.P. Yablonskii from Stepanov Institute of Physics, National Academy of Science Belarus. The PL intensities of the investigated samples as a function of photon energy are shown in

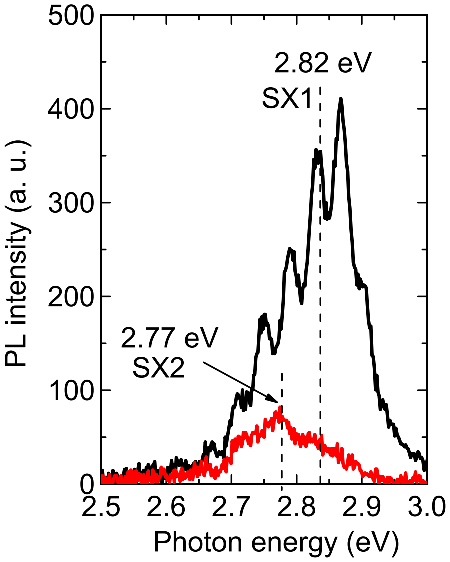

Figure 7.7: The PL intensities obtained at room temperature for samples SX1 (black line) and SX2 (red line) as a function of photon energy. The dashed lines represent the PL peak energy (E_{PL}) positions.

Fig. 7.7. One can observe that PL intensity is weaker and the PL curve is broader for sample SX2 with respect to the sample SX1. The PL peak values (E_{PL}) were determined to be of 2.82 eV and 2.77 eV, respectively. According to the optical selection rules for wurtzite structure semiconductors with a positive crystal-field splitting energy ($\Delta_{\mathrm{cf}}>0$), a transition from the topmost valence band (Γ_9^{v}) to the conduction band (Γ_7^{c}) is strongly allowed for configuration $\mathbf{E}\perp\mathbf{c}$, as it is shown in Fig. 7.8. Therefore, if the PL peak value corresponds to the band-to-band transition from the conduction band to the topmost valence band, the transition energies obtained from the SE and PL should be the same (if where is no strong compositional fluctuation in the alloy). Indeed, the obtained E_{A} (listed in Tab. 7.2) and E_{PL} values for samples SX1 and SX2 are very close to each other.

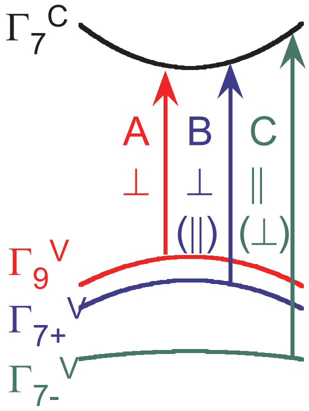

Figure 7.8: Simplified scheme of transitions A, B, and C (for $\Delta_{\mathrm{cf}} > 0$). Symbols ⊥ and ‖ indicate strong transition probability, meanwhile symbols (⊥) and (‖) indicate weak transition probability for the respective polarization states.

In addition, the sample SX1 was investigated by using a confocal scanning laser microscopy. The confocal microscopy is useful technique to investigate the submicron-scale spatial inhomogeneities of PL intensity and spectra that allow to observe band edge inhomogeneities of InGaN alloys [135, 136]. The spatial inhomogeneities of optical properties are caused by fluctuations of the In content in the InGaN alloy [137–139] and the carriers created by a photo-excitation or an electron injection are localized in the In-rich areas [140, 141]. Fig. 7.9(a) and (b) show the spectral-integrated PL intensity mapping and the peak wavelength mapping, respectively, obtained by using a confocal scanning laser microscopy for sample SX1. It is observed that bright peaks corresponding to a higher intensity in Fig. 7.9(a) correlates well with the longest wavelength (red-yellow areas) in Fig. 7.9(b). The separate PL peak intensities at positions 1 and 2 (as denoted in Fig. 7.9) are shown in Fig. 7.10. The PL peak position at point 1 is at ~510 nm, while the peak position at point 2 is at ~480 nm.

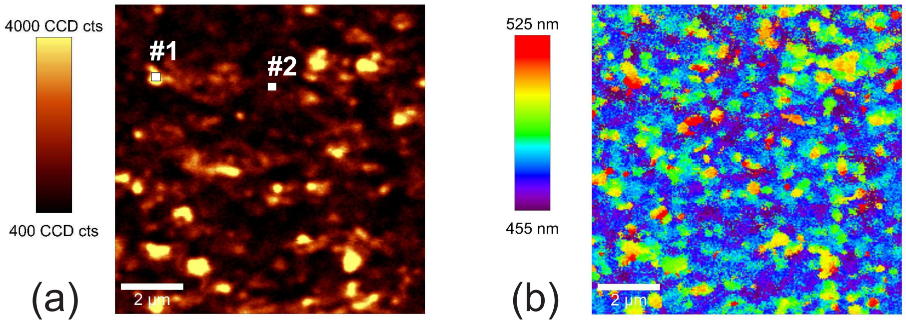

Figure 7.9: Spectral-integrated PL intensity mapping (a) and peak wavelength mapping (b) obtained by confocal scanning laser microscopy for sample SX1.

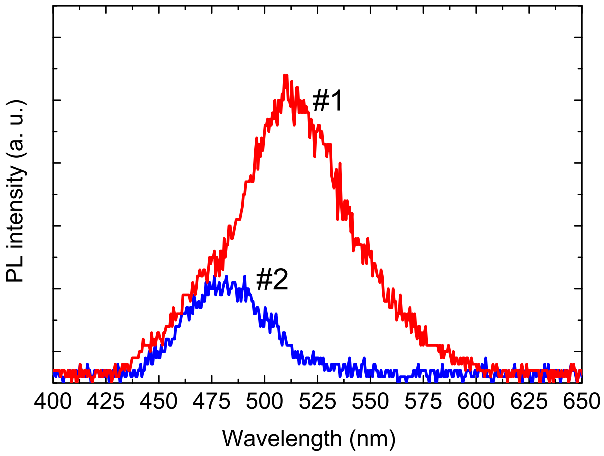

Figure 7.10: PL intensities at point 1 and 2 for sample SX1.

7.4 Summary of Chapter 7

The (0001)-oriented $In_xGa_{1-x}N$ samples with $0.15<x<0.19$ were investigated and the isotropic DFs were determined in the energy range 1-10 eV. Moreover, the $In_xGa_{1-x}N$ sample with an In content of 15.2% was investigated in the extended energy range 10-18 eV and the critical points of the band structure were observed. The analytical form of the DFs in the energy range 1-10 eV was presented. The band-gap and the high energy inter-band transitions were determined from the fit of the analytical model to the experimental DF. The strain influence on the band gap was calculated using the $\mathbf{k}\cdot\mathbf{p}$ method. The strain-free band gap bowing parameter was evaluated to be 1.65 eV and the high-energy inter-band transitions were estimated to be $\sim$1 eV. The obtained experimental band-gap values from the SE measurements were supported with the *ab initio* data.

8 Optical properties of AlInN alloys

In this chapter, the AlInN alloy films nearly lattice matched to GaN will be investigated. The isotropic DFs and their analytical representations of the investigated samples are obtained in the photon energy range 1-10 eV. The band-gap values and high-energy interband transitions are estimated from the fit of the analytical model to the experimental DFs. In previous studies of the In-rich AlInN alloys, Goldhahn *et al* [142] determined the band-gap values, which are in excellent agreement with the values from the work of Jones *et al* [143], and estimated the bowing parameter of 4 eV. By combining the latter results and results obtained in this work, the composition dependent bowing parameter permitting to describe the AlInN band gap in the whole compositional range will be presented. The extension of the studies towards higher energies (above 10 eV) is also of strong interest. Cobet *et al* [98] determined the DFs of hexagonal GaN up to 20 eV by applying the SE with synchrotron radiation (BESSY II) and detected the features attributed to the critical points (CPs) of the band structure above 10 eV. Schley *et al* [7] analysed the hexagonal InN in the photon energy range 0.56-15 eV and also observed several CPs in the range above 10 eV. Therefore, it is expected to detect CPs for the investigated AlInN alloys above 10 eV. The determination and interpretation of the DF in the range extended up to 18 eV is presented. In the last section an a-plane AlInN sample will be investigated. The c-axis of the non-polar sample is on the surface plane, therefore, by measuring the sample by SE at two different configurations (i.e., the c-axis perpendicular to the plane of incidence and c-axis parallel to the plane of incidence), both ordinary and extraordinary DFs can be extracted.

Figures 8.2, 8.3, 8.4, 8.6, and 8.13 as well as Tables 8.2 and 8.4 are reprinted with permission from Sakalauskas *et al*, Journal of Physics D: Applied Physics, Vol. 43, Page 365102, (2010). Copyright 2010, IOP Publishing Ltd. Figure 8.5 is reprinted with permission from Sakalauskas *et al*, Physica Status Solidi A, Vol. 208, Page 1517, (2011). Copyright 2011, John Wiley & Sons, Inc. Figures 8.14 and 8.15 as well as Table 8.5 are reprinted with permission from Sakalauskas *et al*, Physica Status Solidi A, Vol. 209, Page 29, (2012). Copyright 2012, John Wiley & Sons, Inc.

8.1 Description of the investigated AlInN samples

Two sets of AlInN samples are investigated. The first set provided by H. Behmenburg (AIXTRON SE) consists of samples labeled as SA1, SA2, SA3, and SA4 with 14.3%, 17.5%, 19.0%, and 22.8% In content, respectively. The hexagonal (0001)-oriented AlInN epilayers were deposited by MOVPE on sapphire substrates with 3.5 μm GaN buffer layer by varying the temperature from 715 °C to 795 °C. The measured AlInN layer thicknesses by SE and XRD ranges from 73 to 80 nm.

The second set provided by M. Wieneke (OvGU Magdeburg) consists of samples labeled SI1 and SI2. The AlInN epilayers were grown by MOVPE on Si(111) substrate. The MOVPE growth started as follows: an AlN seed layer, a high-temperature AlN layer, a GaN buffer layer, a low-temperature AlN layer dedicated for strain compensation, a 900 nm thick GaN buffer, and finally an AlInN layer. The growth conditions of the alloys are described in detail in Ref. [144]. The layer thicknesses amount to 48 and 54 nm, as determined by SE.

In addition, the non-polar AlInN sample provided by M. Wieneke (OvGU Magdeburg), denoted as SN, was grown by MOVPE on r-plane sapphire substrate leading to an a-plane ([11-20]) orientation of nitride films. Before growing the GaN buffer layer, a ~65 nm thickness AlGaN nucleation layer was deposited on the substrate at 1145 °C with TMGa and TMAl flows of 5 and 15 sccm, respectively. The GaN buffer layer was grown at 1065 °C with TMGa flow of 25 sccm. The epitaxy of AlInN layer was carried out at 780 °C with TMAl and TMIn flows of 80 and 400 sccm, respectively. The NH_3 flow was kept constant at 500 sccm during all growth processes. The AlInN layer and the GaN buffer layer thicknesses were determined by SE to be 49 nm and 2 μm, respectively. The scanning electron microscopy characterization was performed and the AlInN layer thickness of ~45 nm was estimated which is in good agreement with the value determined by SE.

The schematic representation of the investigated samples is sketched in Figure 8.1.

8.2 Structural properties of the investigated AlInN samples

The structural properties of the films were examined by a high-resolution X-ray diffraction (HRXRD). Detailed XRD measurements (symetric diffraction of (0002) planes and grazing incidence in-plane diffraction of (10-10) planes) were performed by the growth groups in order to determine the lattice constants and mosaicity of both the AlInN

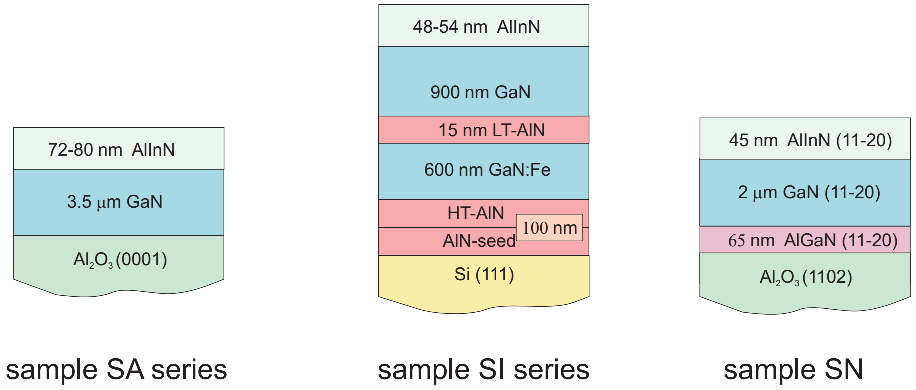

Figure 8.1: Schematic representation of the investigated AlInN samples.

films and the GaN buffer layer for sample SA and SI series. Figure 8.2(a) shows the experimental and simulated data of symmetric diffraction (0002) for sample SA1. The reciprocal space maps of the (10-15) reflection for the SA sample series are shown in Figure 8.2(b). The AlInN and GaN peaks are aligned in the Q_z axis, indicating that AlInN is pseudomorphically grown on a GaN buffer.

The XRD measurements were used for an In content determination. The Vegard's law is assumed for alloys lattice parameter interpolation. The GaN lattice parameters of a=3.183 Å and c=5.189 Å are found for the films on a sapphire substrate indicating a slight compressive in-plane strain which is typical for the growth on this substrate. Mosaic twist and tilt amount to less than 0.1° emphasizing good quality of the layers. The films on Si(111) exhibit, in contrast, a weak tensile strain as indicated by the lattice parameters of a=3.193 Å and c=5.182 Å.

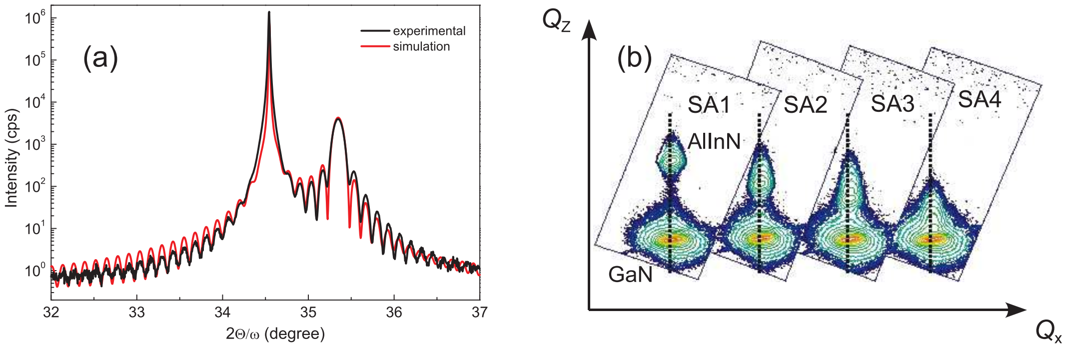

Figure 8.2: (a) Experimental and simulated data of symmetric diffraction (0002) for sample SA1 (14.3%); (b) Reciprocal space maps of the (10-15) reflection for SA sample series.

The In content in the non-polar $Al_{1-x}In_xN$ sample SN was also evaluated from X-ray diffraction measurements. The measured GaN buffer layer lattice parameters were $a^{\mathrm{GaN}} = 3.1922$ Å, $m^{\mathrm{GaN}} = 2.7572$ Å, and $c^{\mathrm{GaN}} = 5.1782$ Å, while the strain-free lattice parameters are $a_0^{\mathrm{GaN}} = 3.189$ Å and c_0^{GaN}=5.185 Å [145]. The measured AlInN lattice parameters were a^{AlInN}=3.1934 Å, m^{AlInN}=2.7588 Å, and c^{AlInN}=5.1758 Å as determined by high resolution X-ray diffraction at the symmetric (11-20) Bragg reflection, and grazing incidence in-plane X-ray diffraction at the (1-100), and (0002) Bragg reflections, respectively. The strain-free AlInN lattice parameters a_0^{AlInN} and c_0^{AlInN} are extrapolated linearly from the binary InN and AlN lattice parameters: $a_0^{\mathrm{AlInN}} = a_0^{\mathrm{InN}} \cdot x + a_0^{\mathrm{AlN}} \cdot (1-x)$ and $c_0^{\mathrm{AlInN}} = c_0^{\mathrm{InN}} \cdot x + c_0^{\mathrm{AlN}} \cdot (1-x)$. The strain free-lattice parameters for InN and AlN: a_0^{InN}=3.537 Å [146] and c_0^{InN}=5.703 Å [146], a_0^{AlN}=3.112 Å [145] and c_0^{AlN}=4.982 Å [145]. The elastic stiffness constants $\mathrm{C}_{ij}^{\mathrm{AlInN}}$ (i=1,2,3; j=1,2,3) for AlInN alloy are also derived linearly from the binary InN and AlN elastic stiffness constants. The InN elastic stiffness constants $\mathrm{C}_{11}^{\mathrm{InN}} = 223$ GPa, $\mathrm{C}_{12}^{\mathrm{InN}} = 115$ GPa, $\mathrm{C}_{13}^{\mathrm{InN}} = 92$ GPa, and $\mathrm{C}_{33}^{\mathrm{InN}} = 224$ GPa were taken from Ref. [146, 147], while AlN elastic stiffness constants $\mathrm{C}_{11}^{\mathrm{AlN}} = 411$ GPa, $\mathrm{C}_{12}^{\mathrm{AlN}} = 149$ GPa, $\mathrm{C}_{13}^{\mathrm{AlN}} = 99$ GPa, and $\mathrm{C}_{33}^{\mathrm{AlN}} = 389$ GPa were taken from Ref. [148].

The strain in the AlInN layer is evaluated by using the following equations:

$$\epsilon_{xx} = \epsilon_a = \frac{a^{\mathrm{AlInN}} - a_0^{\mathrm{AlInN}}}{a_0^{\mathrm{AlInN}}} \tag{8.1}$$

$$\epsilon_{yy} = \epsilon_m = \frac{m^{\mathrm{AlInN}} - m_0^{\mathrm{AlInN}}}{m_0^{\mathrm{AlInN}}} \tag{8.2}$$

$$\epsilon_{zz} = \epsilon_c = \frac{c^{\mathrm{AlInN}} - c_0^{\mathrm{AlInN}}}{c_0^{\mathrm{AlInN}}} \tag{8.3}$$

Assuming that the stress σ_{xx}=0 in the growth direction and solving the equation:

$$\sigma_{xx} = C_{11}^{\mathrm{AlInN}} \cdot \epsilon_{xx} + C_{12}^{\mathrm{AlInN}} \cdot \epsilon_{yy} + C_{13}^{\mathrm{AlInN}} \cdot \epsilon_{zz}, \tag{8.4}$$

the In content $x \approx 20\%$ was obtained. The obtained strain in the growth direction (out-of-plane) is $\epsilon_{xx} = -1.1 \times 10^{-3}$, while the in-plane strain mounts to $\epsilon_{yy} = -3.6 \times 10^{-3}$, and $\epsilon_{zz} = 9.6 \times 10^{-3}$ with x, y, and z being parallel to the [11-20], [1-100], and [0002] directions, respectively.

A smooth surface morphology, which is essential for the accuracy of the SE results, was revealed by AFM measurements (provided by the growth groups). Scans of 5×5 μm^2 area for the first set of samples and 10×10 μm^2 for the second set of samples were

Sample	surface roughness (nm)		alloy thickness (nm)	
	AFM	SE	XRD	SE
SA1 (14.3%)	1.1	2.0	72	73
SA2 (17.5%)	1.2	2.2	75	74
SA3 (19.0%)	1.4	2.4	78	77
SA4 (22.8%)	1.4	3.6	80	80
SI1 (17.4%)	2.1	6.2	47	48
SI2 (24.2%)	1.4	1.9	55	54
SN (20.0%)	2.5	4.2	-	45

Table 8.1: Values for the surface roughness and the AlInN layer thickness as determined by AFM, SE, and XRD.

performed. The root-mean square (rms) roughness values are summarized in Tab. 8.1. They range typically between 1.1 and 1.4 nm, only sample SI1 showed a slightly higher value of 2.1 nm which is not critical for the ellipsometry studies. The surface roughness for SN sample was obtained to be 2.5 nm. In addition, the surface roughness obtained from SE simulations together with the AlInN epilayer thickness determined from XRD and SE are listed in Table 8.1. The obtained layer thickness from both characterisation techniques are in excellent agreement.

8.3 AlInN dielectric function and its analytical representation

First of all, optical selection rules will be considered prior to the interpretation of the DF. It starts from the VB ordering around the Γ point of the Brillouin zone and the symmetry of the wave functions. As it was discussed in Chapter 2, crystal field (Δ_{cf}) and spin-orbit interaction (Δ_{so}) split the VB maximum into three two-fold-degenerate VBs with Γ_9^{v}, Γ_{7-}^{v}, and Γ_{7+}^{v} symmetry. The energy difference $\Gamma_7^{\mathrm{c}} - \Gamma_9^{\mathrm{v}} = E_{\mathrm{A}}$ for strain-free material is used as a reference point for the analysis of inter-band absorption. This definition is essential, because the compositional dependence of transition energies is considered. InN has a spin-orbit energy of 5 meV and crystal-field splitting energy of 19 meV [149]. The AlN has a slightly larger spin-orbit energy of 16 meV and a large negative crystal-field splitting energy of -212 meV [30]. It is important to emphasize that the sign of crystal field energy inverts the valence band ordering as it was shown in Chapter 2, in Fig. 2.2. Therefore, the band crossing will occur for $\mathrm{In}_x\mathrm{Al}_{1-x}\mathrm{N}$ alloy at Δ_{cf}=0 eV (approximately at x=0.92, if a linear crystal-field splitting energy interpolation is used). The transitions from Γ_9^{v} valence band to the Γ_7^{c} conduction band (labeled A) and from Γ_{7-}^{v} to Γ_7^{c} (labeled C) exhibit strong relative oscillator strengths only for the configuration $\boldsymbol{E}\perp\boldsymbol{c}$. Thus, by measuring c-plane AlInN samples with an ellipsometer (almost $\boldsymbol{E}\perp\boldsymbol{c}$), these transitions will dominate the optical response. In contrast, the transition from Γ_{7+}^{v} to Γ_7^{c} (labeled B) is strongly allowed only for the configuration $\boldsymbol{E}\|\boldsymbol{c}$. The transition B stems from the topmost valence band, but its oscillator strength is weak for the configuration $\boldsymbol{E}\perp\boldsymbol{c}$.

The obtained isotropic DFs of samples SA1, SA2, SA3, and SA4 in the spectral range from 1 to 10 eV are shown in Fig. 8.3. Pronounced features attributed to the critical points of the band structure are found in the high-energy range of ε_2. They have a strong impact on the dispersion of ε_1 at lower energies. For the second set of samples (AlInN/Si(111)), data are only available for the range from 1 to 6.42 eV. Figure 8.4(a) and (b) show the results around the band gap for the AlInN/sapphire and AlInN/Si(111) samples, respectively. It is clearly seen that with increasing In content, the absorption onset (imaginary part of the dielectric function - ε_2) redshifts. Following the Kramers-Kronig relation, the ε_1 peak also shifts to the lower energies. Fig. 8.4(b) also shows the DF of AlN for comparison. The $\mathrm{In}_x\mathrm{Al}_{1-x}\mathrm{N}$ sample SA1 with In content of 14.3% was investigated in the extended energy range. The isotropic DF of sample SA1 in the range 1-18 eV is shown in Figure 8.5(b). The appearing features (e.g., peaks or shoulders) in the shape of the DF components ε_1 and ε_2 are related to the inter-band transitions due to the peculiarities of the joint density of states in the vicinity of CPs of the band structure [150]. Three critical points are observed in the 7-10 eV range. In the 10-14 eV

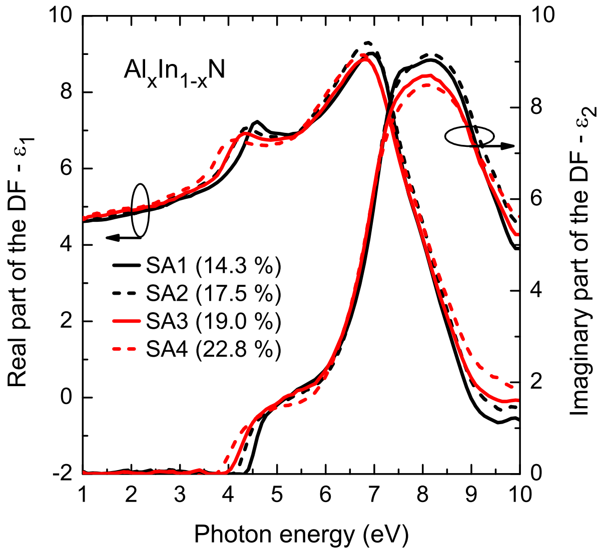

Figure 8.3: Real and imaginary parts of the isotropic DFs for the SA sample series.

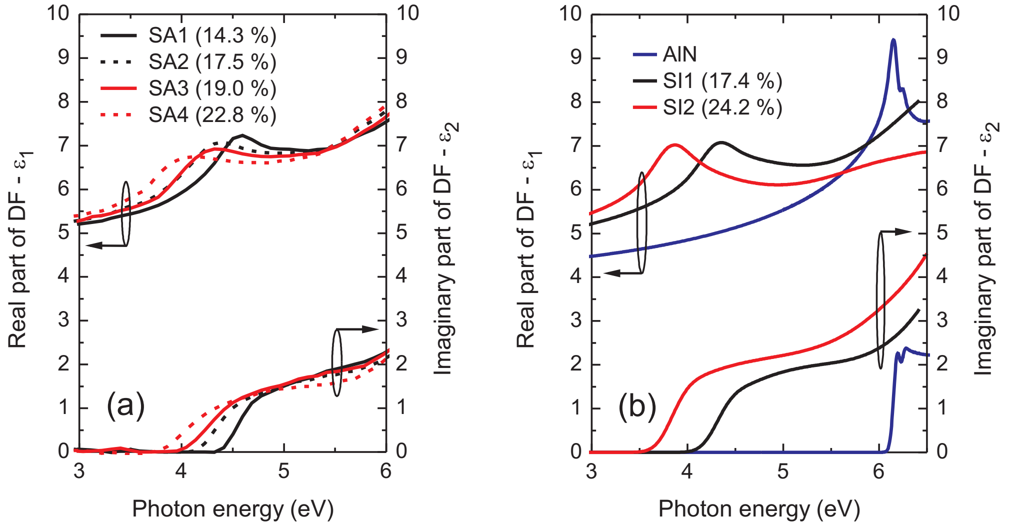

Figure 8.4: Isotropic DFs of AlInN around the band gap: for AlInN/sapphire samples (a) and AlInN/Si(111) samples together with data for AlN (b). Ordinary DF of AlN used for comparison is taken from Ref. [77].

range, the broad shoulder in ε_2 and broad peak in ε_1 are observed and in the 14-18 eV range, the decreasing plateau in ε_2 and broad shoulder in ε_1 are observed. Following the method as presented in [134] the CPs denoted E_4, E_5, and E_6 were evaluated to be ~10.6 eV, ~12.5 eV, and ~14.2 eV, respectively. For comparison purpose, the isotropic DF of InN and ordinary DF of AlN [77] are also provided in Fig. 8.5(a) and Fig. 8.5(c), respectively. The CPs of the band structure for the InN are present in the range from 4-12 eV, as it is indicated by arrows in Figure 8.5(a). In the AlN case, three CPs are observed in ε_2 below 10 eV. Above 10 eV, the theoretical ε_2 data [151] calculated using a first-principle technique, which includes the electron-hole interaction, is provided.

By fitting simultaneously experimentally obtained real and imaginary parts of the DF with the analytical expressions (Eqs. 3.18-3.21, described in Chapter 3.2), it is possible to determine the band-gap energies E_A and high-energy inter-band transitions E_1, E_2 and E_3. The fitting parameters for Eq. 3.18 and Eq. 3.21 are listed in Tab. 8.2. The difference between transition energy E_A and E_C was kept fixed at 13 meV, which corresponds to the linearly interpolated spin-orbit splitting energy at x=0.18. The critical point energies E_1, E_2, and E_3 obtained by fitting the analytical DF model are

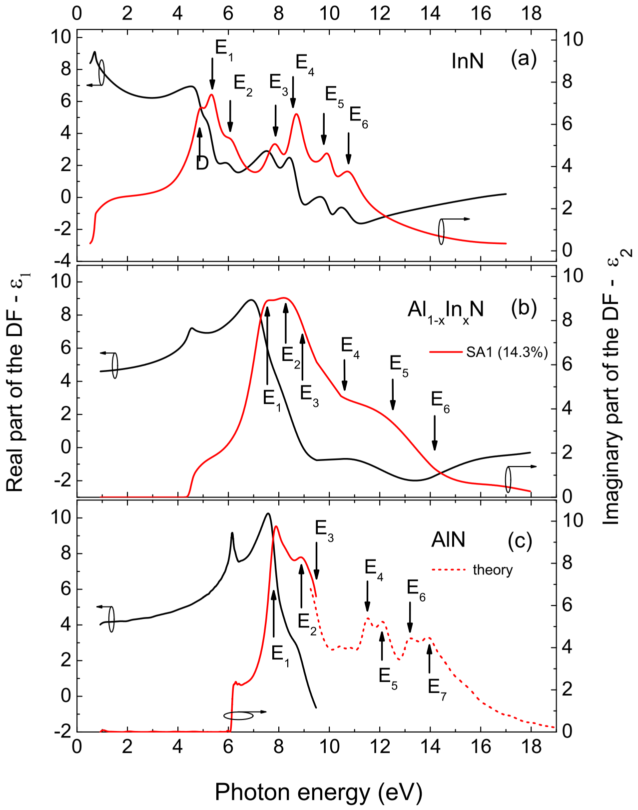

Figure 8.5: Isotropic DFs for (a) InN and (b) $\mathrm{Al}_{1-x}\mathrm{In}_x\mathrm{N}$ alloy with x=14.3% (solid line) as well as (c) ordinary DF for AlN (1-10 eV) [77] together with the theoretical ε_2 in the extended energy range 9-18 eV [151]. Arrows indicate the CPs of the band structure.

in good agreement with the energies determined from the third derivative method [134] (summarized in Tab. 8.3 for the AlInN/sapphire sample set). The experimental and calculated (using the Eq. 3.18 and Eq. 3.21 and parameters from Tab. 8.2) complex DF as well as complex index of refraction for sample SA1 are shown in Fig. 8.6(a) and (b), respectively.

SE measurements for the AlInN/Si(111) sample set were conducted only up to 6.4 eV. The transition energy E_A (transition from Γ_9^v valence band to the Γ_7^c conduction band) values of 4.34 eV and 3.85 eV were determined for samples SI1 and SI2, respectively.

8.3.1 Strain influence on the band gap energy

The strain influence on the band gap must be taken into consideration before evaluating the bowing parameter for the AlInN alloys. A six-band $\mathbf{k}\cdot\mathbf{p}$ model [70] is used to calculate the strain influence. The $\mathbf{k}\cdot\mathbf{p}$ parameters used for the calculations are presented in Chapter 2, in Table 2.1.

Table 8.2: Fitting parameters for the DF analytical model.

Sample	SA1 (14.3%)	SA2 (17.5%)	SA3 (19.0%)	SA4 (22.8%)
A_0	1.24	1.08	1.05	0.99
A_1 (eV^2)	44.85	43.63	42.74	43.31
A_2 (eV^2)	37.01	50.13	47.84	55.82
A_3 (eV^2)	70.76	79.52	74.84	82.98
A_{BS}(eV^2)	5.8×10^{-3}	1.5×10^{-2}	9.2×10^{-3}	0.46
A_{CS}(eV)	1.5	1.26	1.33	0.78
A_{P} (eV)	158.05	189.02	172.88	270.09
E_1 (eV)	7.42	7.37	7.33	7.30
E_2 (eV)	8.20	8.20	8.17	8.20
E_3 (eV)	8.94	9.06	9.07	9.21
E_{A} (eV)	4.57	4.35	4.30	4.04
E_{C} (eV)	E_A+0.013	E_A+0.013	E_A+0.013	E_A+0.013
E_{P} (eV)	15.54	15.33	15.45	16.27
Γ_0 (eV)	4.4×10^{-2}	4.4×10^{-2}	5.2×10^{-2}	5.4×10^{-2}
Γ_1 (eV)	1.21	1.27	1.33	1.41
Γ_2 (eV)	1.31	1.47	1.52	1.65
Γ_3 (eV)	1.89	2.07	2.15	2.33
Γ_{BS}(eV)	3.3×10^{-2}	0.13	0.13	2.78
Γ_{CS} (eV)	0.1824	0.20	0.28	0.19
R (meV)	29	31	35	17
b	-1.9	-2.7	-2.2	-4.18

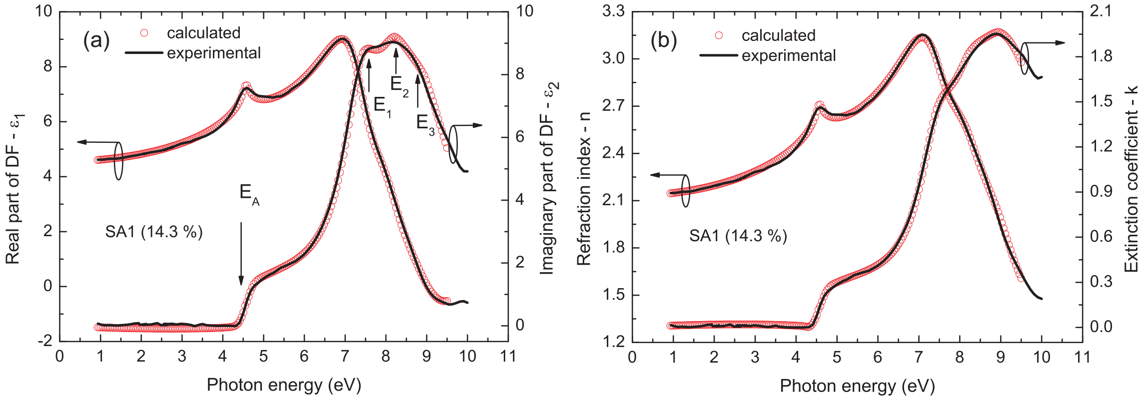

Figure 8.6: Experimental and calculated complex DF (a) and complex index of refraction (b) of sample SA1 (In content 14.3 %).

The strain-induced band-gap energy shifts $\Delta E_A^{\mathrm{strain}}$ calculated from the $\mathbf{k}\cdot\mathbf{p}$ model around the Γ point of the Brillouin zone, transition energies E_{A} obtained from the DF

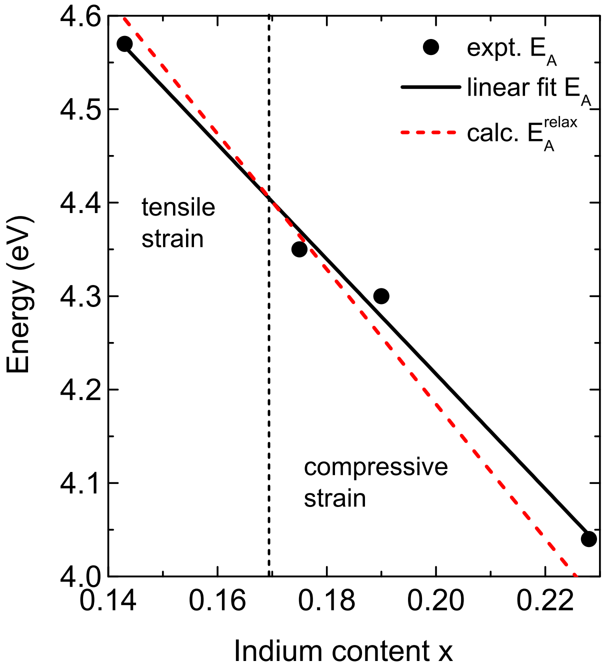

Figure 8.7: Experimental band-gap E_A values (full circles) obtained from SE for SA sample series. The black solid line represents the linear fit of the experimental data values, while the red dashed line represents the calculated strain-free band-gap values.

(influenced by strain), and strain-corrected band-gap $E_A^\mathrm{relax} = E_A - \Delta E_A^\mathrm{strain}$ values are summarized in Table 8.3. The following should be noticed. Pseudomorphic AlInN films with low In-content experience tensile strain leading to a red-shift of the experimental data for the E_A transition. For high In-content, a strain-induced blue shift is found to be up to ∼65 meV for the layers studied here. It is obvious that this effect has to be taken into account for determining the strain-free band-gap bowing parameters. Figure 8.7 shows the experimental band-gap E_A values (full circles) determined by SE for sample SA series. The solid black line is a linear fit of the experimental values. The red dashed line represents the calculated band-gap values for the relaxed material. For

Sample	E_A (eV)	$\Delta E_\mathrm{A}^\mathrm{strain}$ (meV)	$E_\mathrm{A}^\mathrm{relax}$ (eV)	E_1 (eV)	E_2 (eV)	E_3 (eV)
SA1 (14.3%)	4.57	-26	4.60	7.40	8.11	8.81
SA2 (17.5%)	4.35	9	4.34	7.31	8.15	8.80
SA3 (19.0%)	4.30	25	4.27	7.28	8.12	8.80
SA4 (22.8%)	4.04	65	3.98	7.18	8.08	8.79
SI1 (17.4%)	4.34	-18	4.36	-	-	-
SI2 (24.2%)	3.85	54	3.80	-	-	-

Table 8.3: Estimated band gap E_A, calculated strain induced band-gap shift $\Delta E_\mathrm{A}^\mathrm{strain}$, strain-free band gap $E_\mathrm{A}^\mathrm{relax}$ and estimated critical point energies E_1, E_2, and E_3 (from third derivative method).

the SA sample series with a GaN buffer layer having a lattice constant of a=3.183 Å, the AlInN layer would be lattice matched at ∼17%. Below or above 17% the layer becomes tensile or compressive strained, respectively. In the tensile (compressive) strain region measured experimental band-gap values are smaller (larger) in comparison with the values for the relaxed material.

8.3.2 AlInN alloy band-gap and high-energy inter-band transition bowing parameters

In order to evaluate accurately a band-gap E_A (transition $\Gamma_9^\mathrm{v} \longrightarrow \Gamma_7^\mathrm{c}$) bowing parameter, experimental data in a wider compositional range are needed. In addition, the data determined by SE from the work of Goldhahn *et al* [142] for the In-rich AlInN alloys and AlN were employed. The strain-corrected band-gap values $E_\mathrm{A}^\mathrm{relax}$ for AlInN samples together with the experimental data points obtained for the AlN, the InN and the In-rich AlInN alloys [142] are shown in Fig. 8.8(a). The fitted bowing parameter (b_A)

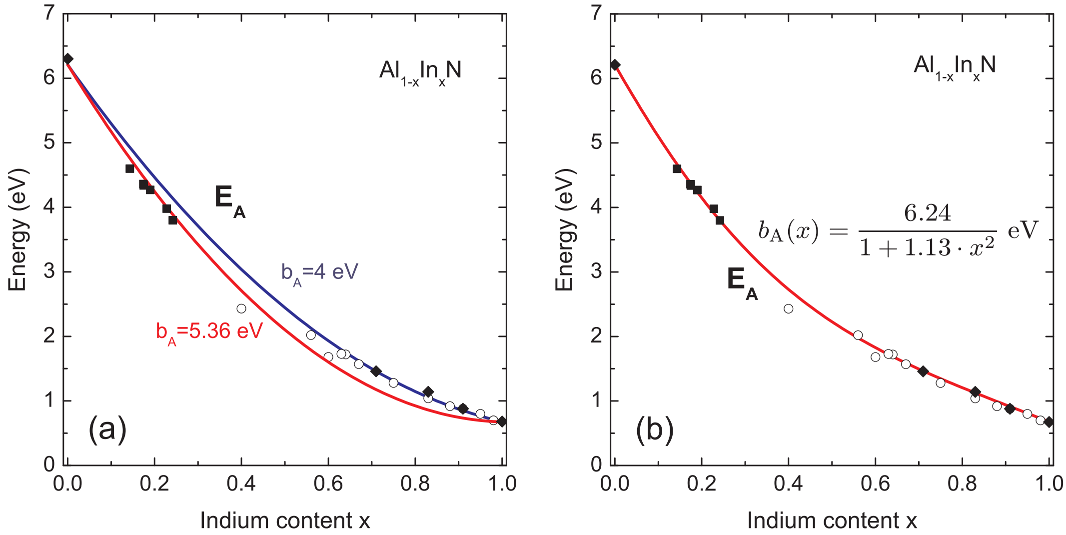

Figure 8.8: Experimental band-gap energies of $\mathrm{Al_{1-x}In_xN}$ as a function of In content: (a) The blue solid curve represents the bowing curve with a bowing parameter of 4 eV obtained for In-rich AlInN alloys from the work of Goldhahn *et al* [142], while the red solid curve represents the bowing curve with a bowing parameter of 5.36 eV by fitting all data points, i.e., obtained in this work (quadrates) and in the work of Goldhahn *et al* [142] (diamonds); (b) bowing curve obtained by fitting the experimental data (denoted by quadrates and diamonds) with a compositional dependent bowing parameter $b_\mathrm{A}(x)$. The data points for InN and AlN were taken from Ref. [142] (denoted by diamond symbols). For comparison, the experimental data points from the work of Jones *et al* [143] for In-rich AlInN alloys were also included (denoted by open circles).

for the transition energy E_A yields a value of 5.36 ± 0.36 eV (with endpoint energies of $E^{\mathrm{InN}} = 0.675$ eV for InN [13] and $E^{\mathrm{AlN}} = 6.24$ eV [30] for AlN). This obtained value is consistent with the value of 5.3 eV obtained in Ref. [152] and the value of 4.96 ± 0.28 eV obtained in Ref. [153] within the error interval. Goldhahn *et al* [142] fitted the data points in the In-rich region and obtained the bowing parameter of 4 eV (the bowing curve for b_{A}=4 eV represented with a blue line in Fig. 8.8). For comparison, the transition energy E_{A} values from the work of Jones *et al* [143] obtained by modeling optical absorption data for the high quality AlInN samples are represented with the open circles in Fig. 8.8(a).

One can observe that the fitted band-gap curve with a bowing parameter of 5.36 eV does not describe well the experimental data points in Fig. 8.8(a). Therefore, to have a better agreement between the experimental band-gap data and fitted bowing curve, a new empirical expression is proposed:

$$E_{\mathrm{A}}^{\mathrm{AlInN}} = E_{\mathrm{A}}^{\mathrm{InN}} \cdot x + E_{A}^{\mathrm{AlN}} \cdot (1-x) - b_{\mathrm{A}} \cdot (1-x) \cdot x, \tag{8.5}$$

where a bowing parameter b_{A} is expressed as a non-linear function of In content (x):

$$b_{\mathrm{A}} = b_{\mathrm{A}}(x) = \frac{A}{1 + C \cdot x^2}. \tag{8.6}$$

The fitted Eq. 8.5 to the experimental strain-corrected band-gap data points (E_{A}) yielded the parameters A=6.24±0.13 eV and C=1.13±0.14. As it is clearly seen in Fig. 8.8(b), the composition dependent bowing parameter describes much better the experimental band-gap values E_{A}. The experimental AlInN band-gap bowing curve together with the calculated *ab initio* data for uniform (not clustered) AlInN alloys from the work of Gorczyca *et al* [128] are compared in Fig. 8.9. The obtained bowing parameter $b_{\mathrm{A}}(x)$ ranges from 2.93 to 6.24 eV and yields the value of 4.87 eV for x=0.5, which is in good agreement with the *ab initio* calculated bowing parameter for the uniform (not clustered) AlInN case, which ranges from 2.1 to 6.2 eV, and is equal to 4.4 eV for x=0.5 [128].

Moreover, the PL measurements were conducted by the research group of prof. G.P. Yablonskii (Stepanov Institute of Physics, National Academy of Science Belarus) on the AlInN/sapphire sample series with slightly different In contents (13.5%, 16.7%, and 19.2%). PL measurements were conducted at RT by using 5^{th} harmonic of Nd:YAG laser with λ_{exc}=213 nm and I_{exc}=1.7 MW/cm^2. Additionally, the PL data for the $\mathrm{In}_x\mathrm{Al}_{1-x}\mathrm{N}$ samples with x=0 and for x>0.7 are employed from the work of Kamimura *et al* [154].

The PL peak energies from Kamimura work were obtained from the AlInN columns, therefore no residual strain was present. The AlInN films with 13.5%, 16.7%, and 19.2% were pseudomorhically grown on GaN/sapphire substrates, therefore, the strain correction must be done. After **k·p** calculations, it was found that a strain induced shift for transition B ($\Delta E_{\mathrm{B}}^{\mathrm{strain}}$) is -92 meV, ~0 meV, and 72 meV, for samples with In composition 13.5%, 16.7%, and 19.2%, respectively. Using the expresion $E_{\mathrm{PL}}^{\mathrm{relax}}=E_{\mathrm{PL}}-\Delta E_{\mathrm{B}}^{\mathrm{strain}}$ the strain corrected PL peak values were obtained and presented in Fig. 8.10 together with the strain-free band-gap values (E_{A}) obtained from SE. One can note that PL values are slightly below SE values. Refering to the valence band splitting, ordering and optical selection rules in the wurtzite structure semiconductors, as it was disscused in Chapter 2, and assuming that PL peak corresponts to the band-to-band transition from the conduction band to the topmost valence band, a simple schematic representation of the transitions for AlInN with a negative crystal field splitting energy ($\Delta_{\mathrm{cf}} < 0$) can be done, as it is shown in Figure 8.11. One must note that from the SE measurements, the transition energy is evaluated from the absorption onset, therefore the determined transition value for the alloy (which normally possesses the composition fluctuations) will correspond to the average value. Here, the investigated samples are (0001)-oriented, therefore, only the transition A and C will be detected from the SE measurements. If the alloy composition fluctuations are not very large, one can expect that the PL band-to-band peak value should be very close to the transition B. The difference between transitions A and B is denoted as ΔE_{AB}. In previous studies, the

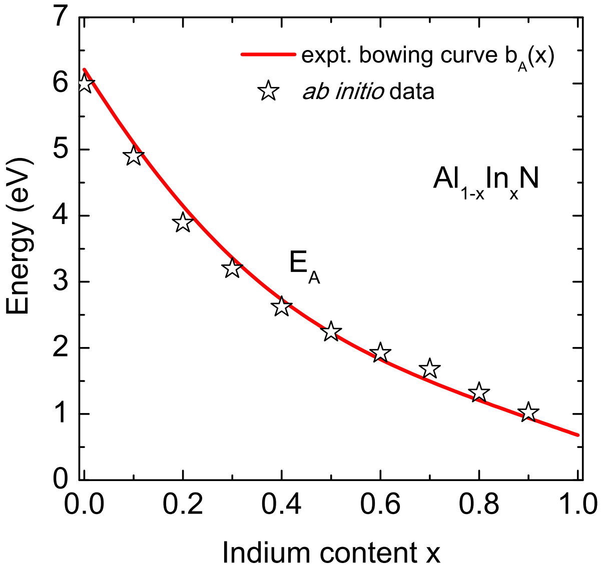

Figure 8.9: AlInN band-gap experimental values and experimental band-gap bowing curve with a composition dependent bowing parameter $b_{\mathrm{A}}(x)$ compared with the *ab initio* calculated data for uniform AlInN alloy from the work of Gorczyca *et al* [128].

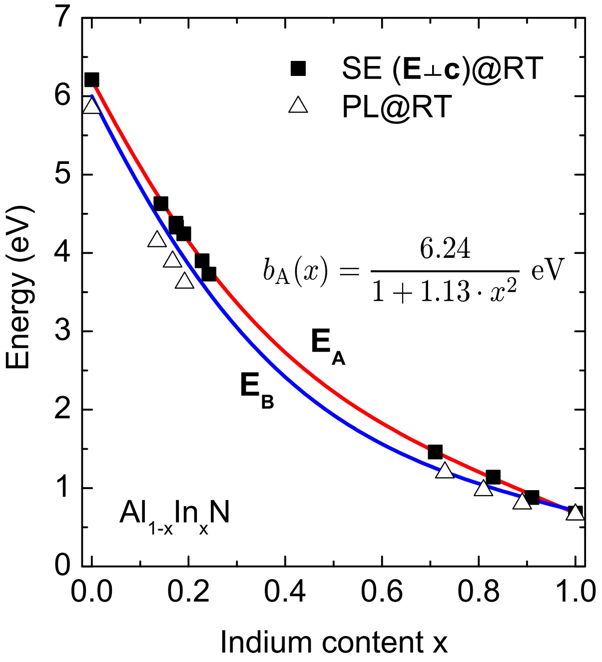

Figure 8.10: PL peak values (triangles) together with the band gap values obtained from SE (squares) obtained at RT as a function of In content (x). The red solid line represents the calculated transition E_A and the blue solid line represents the calculated transition E_B. The SE and PL experimental data for In-rich AlInN and AlN were employed from Ref. [142] and Ref. [154], respectively.

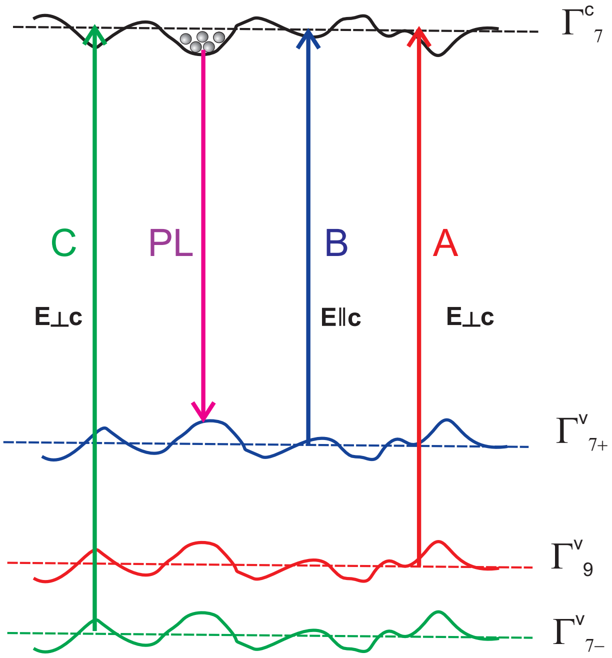

Figure 8.11: Schematic representation of the transition energies for the wurtzite semiconductor with negative crystal-field splitting energy $\Delta_{cf}<0$. Transitions A, B and C represent the transitions allowed for the configurations $\boldsymbol{E}\perp\boldsymbol{c}$, $\boldsymbol{E}\|\boldsymbol{c}$, and$\boldsymbol{E}\perp\boldsymbol{c}$, respectively. Transition PL indicates the band-to-band transition from the CB to the topmost VB. The horizontal dashed lines represent the average level of the CB or VBs for the alloy with a compositional fluctuations.

optical anisotropy was investigated and the splitting between the transitions A and B were determined to be ∼−210 meV [30, 77] and ∼25 meV [68], for AlN and InN, respectively. By using the interpolation for the determined splitting values for AlN and

InN and introducing the bowing factor of 0.83 eV [5], it is possible to determine the ΔE_{AB} in the whole compositional range. Now, the transition E_{B} can be expressed as

$$E_{\mathrm{B}}^{\mathrm{AlInN}} = E_{\mathrm{A}}^{\mathrm{AlInN}} + \Delta E_{\mathrm{AB}}^{\mathrm{AlInN}} \tag{8.7}$$

where $E_{\mathrm{A}}^{\mathrm{AlInN}}$ is expressed by Eq. 8.5 and $\Delta E_{\mathrm{AB}}^{\mathrm{AlInN}} = -0.21 \times (1-x) + 0.03 \times x - 0.83 \times x \times (1-x)$. The calculated curve of the transition E_{B} is shown in Fig. 8.10 and describes well the PL data from Kamimura *et al* [154]. However, the PL data for the pseudomorphically grown AlInN films are slightly below this curve (possibly due to strong composition fluctuations in the alloy; no spacial resolution PL studies were performed on these samples).

By using the determined high-energy transitions from the work of Goldhahn *et al* [142] for In-rich AlInN alloys together with the values obtained in this work, the bowing factors b_1, b_2, and b_3 for the high-energy critical points E_1, E_2, and E_3 were found to be 1.59 ± 0.07 eV, 2.52 ± 0.26 eV, and ~0, respectively. The high-energy inter-band transitions together with the band-gap values as a function of In content are depicted in Figure 8.12.

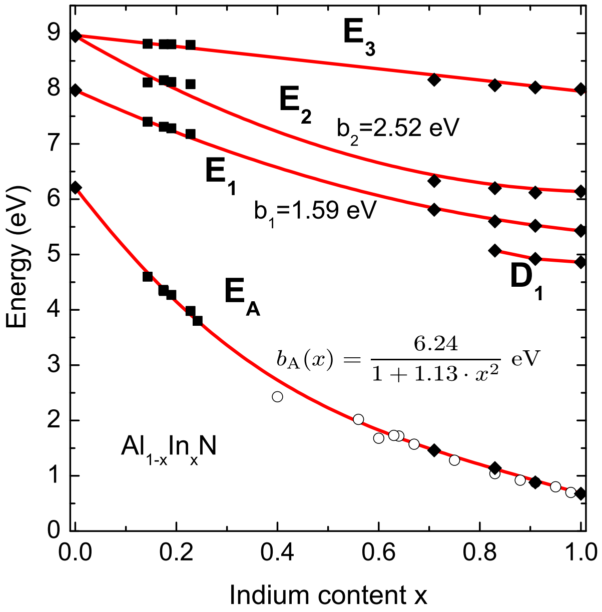

Figure 8.12: AlInN alloy band-gap and high-energy inter-band transitions as a function of In content.

8.3.3 Dispersion below the band gap and high-frequency dielectric constant

In this section, the real part of the isotropic DF below the band gap for the investigated SA and SI sample series will be presented in the analytical form as well as the values of high-frequency dielectric constants ε_∞ and its linear interpolation will be deduced.

The dispersion of ε_1 for AlInN samples in the transparent region (below the band gap) can be presented in the analytical form by using a simplified analytical expression (3.22) from Chapter 3.2. The high-frequency dielectric constants (ε_∞) are obtained by fitting experimentally obtained ε_1 below the band gap with the analytical expression (3.22) and by extrapolating this expression to zero photon energy ($\hbar\omega \to 0$). Their values together with the fitted parameters are listed in Tab. 8.4. By extrapolating obtained ε_∞ values for x<0.2, the following expression of high frequency dielectric constant as a function of In content for AlInN alloys is obtained:

$$\varepsilon_\infty = 2.78 \times x + 4.12 \tag{8.8}$$

By employing the parameters from Tab. 8.4 and applying the Eq. 3.22, ε_1 values below the band gap are generated, as it is shown in Fig. 8.13 together with the AlN and GaN ε_1 values used for comparison. The precise ε_1 (or refractive index $n_1 = \sqrt{\varepsilon_1}$) values below the band gap are needed for the optoelectronic device development.

Sample	ε_∞	A_G	E_G (eV)	A_H (eV)	E_H (eV)
AlN	4.11	2.91	6.16	34.90	10.26
SA1 (14.3%)	4.54	1.53	4.52	40.01	8.81
SA2 (17.5%)	4.61	1.82	4.38	38.85	8.82
SA3 (19.0%)	4.65	1.47	4.21	41.15	8.87
SA4 (22.8%)	4.71	1.40	4.02	41.63	8.82
SI1 (17.4%)	4.61	2.47	4.37	36.71	10.43
SI2 (24.2%)	4.67	2.34	3.85	36.73	11.31

Table 8.4: High-frequency dielectric constant for the investigated (0001)-oriented AlInN samples and fitted parameters of Eq. (3.22).

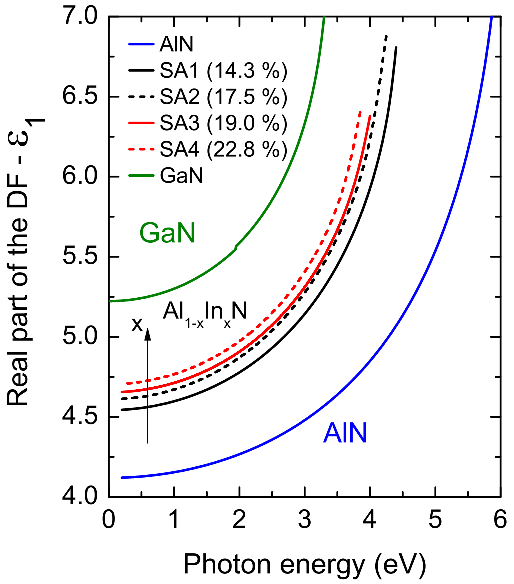

Figure 8.13: Generated real part of the DF (ε_1) values in the transparent region (below the band gap) for sample SA series. The dotted lines shows the real part of the DF (ε_1) for GaN and AlN used for comparison.

8.4 Optical anisotropy of a-plane $Al_{0.8}In_{0.2}N$

In previous section 8.3, the isotropic DFs of the AlInN alloys were determined in the energy range 1-10 eV and the extended energy range up to 18 eV. In these studies, however, c-plane samples were investigated by ellipsometry (almost a configuration $\boldsymbol{E}\perp\boldsymbol{c}$) and, thus, only so called isotropic DFs were determined. Now, by investigating an a-plane $Al_{0.8}In_{0.2}N$ sample SN and measuring it by ellipsometry at two configurations (i.e., the c-axis is perpendicular and parallel to the plane of incidence), it is possible to determine both ordinary and extraordinary DFs.

The following notations indicate the transitions from VBs to CB are used: A ($\Gamma_9^v \rightarrow \Gamma_7^c$), B ($\Gamma_{7+}^v \rightarrow \Gamma_7^c$) and C ($\Gamma_{7-}^v \rightarrow \Gamma_7^c$). According to the optical selection rules for an unstrained material with $\Delta_{cf}<0$, the transitions A and C are dominated for configuration $\boldsymbol{E}\perp\boldsymbol{c}$, while transition B is dominated for configuration $\boldsymbol{E}\|\boldsymbol{c}$.

The complex ordinary and extraordinary DFs obtained for a non-polar sample SN are shown in Figure 8.14. A pronounced optical anisotropy is observed in the whole investigated photon energy range 1-6 eV. If one looks closer near the band gap region, one can notice that the absorption onset for the extraordinary imaginary part of the DF is red-shifted with respect to absorption onset of the ordinary imaginary part of the DF. This is fully consistent with the VB ordering for the materials with a negative crystal field splitting energy $\Delta_{cf}<0$ such as in AlN [77] but opposite to the polarization anisotropy of InN [7] with $\Delta_{cf}>0$. The difference between transition energies E_A and E_C is very small

∼13 meV, therefore, it is not resolved. From the fit of the analytical model (described by Eqs. 3.21-3.18 in Chapter 3.2) to the ordinary and extraordinary experimental DFs, the inter-band transitions E_{A}=4.44 eV and E_{B}=4.24 eV (fundamental band gap) are determined, which correspond to the transition energies A and B, respectively. The difference between transition E_{A} and E_{B} amounts to $\Delta E_{\mathrm{AB}}=E_{\mathrm{B}}$-$E_{\mathrm{A}}=\sim-200$ meV.

The ordinary and extraordinary DFs describe the optical response of the material for configurations $\boldsymbol{E}\perp\boldsymbol{c}$ and $\boldsymbol{E}\|\boldsymbol{c}$, respectively. According to the optical selection rules for unstrained Al-rich AlInN alloy the transition A is allowed for configuration $\boldsymbol{E}\perp\boldsymbol{c}$, while transition B for $\boldsymbol{E}\|\boldsymbol{c}$. By using the **k·p** method [70] and employing the parameters from Tab. 2.1 in Chap. 2, the relative oscillator strengths for the strained AlInN layer are evaluated: for configuration $\boldsymbol{E}\|\boldsymbol{x}$ $\mathrm{f}_x^{\mathrm{A}}$=0.89, $\mathrm{f}_x^{\mathrm{B}}$=0.01, and $\mathrm{f}_x^{\mathrm{C}}$=0.10; for configuration $\boldsymbol{E}\|\boldsymbol{y}$ $\mathrm{f}_y^{\mathrm{A}}$=0.10, $\mathrm{f}_y^{\mathrm{B}}$=0.01, and $\mathrm{f}_y^{\mathrm{C}}$=0.89; for configuration $\boldsymbol{E}\|\boldsymbol{z}$ $\mathrm{f}_z^{\mathrm{A}}$=0, $\mathrm{f}_z^{\mathrm{B}}$=0.99, and $\mathrm{f}_z^{\mathrm{C}}$=0.01. The calculated relative oscillator strengths indicate that for the configuration $\boldsymbol{E}\perp\boldsymbol{c}$ (i.e. $\boldsymbol{E}\|\boldsymbol{x}$ or $\boldsymbol{E}\|\boldsymbol{y}$) the transition B probability is almost zero, while for the configuration $\boldsymbol{E}\|\boldsymbol{c}$ (i.e. $\boldsymbol{E}\|\boldsymbol{z}$) the transition B probability is almost 1. The strain-free energy difference $\Delta E_{\mathrm{AB}}^{\mathrm{relax}}$ was evaluated to be ~-296 meV. By using a linear interpolation for the determined splitting values for AlN of ~-210 meV [77] and InN of ∼25 meV [68], the ΔE_{AB} is obtained to be -163 meV at x=20%. Only, by introducing a bowing factor of 0.83 eV, the splitting value of -296 meV is obtained.

The analytical forms of the real part of the ordinary and extraordinary DFs ($\varepsilon_{1,o}$ and $\varepsilon_{1,e}$) in the transparent region (below the band gap) are needed for optoelectronic

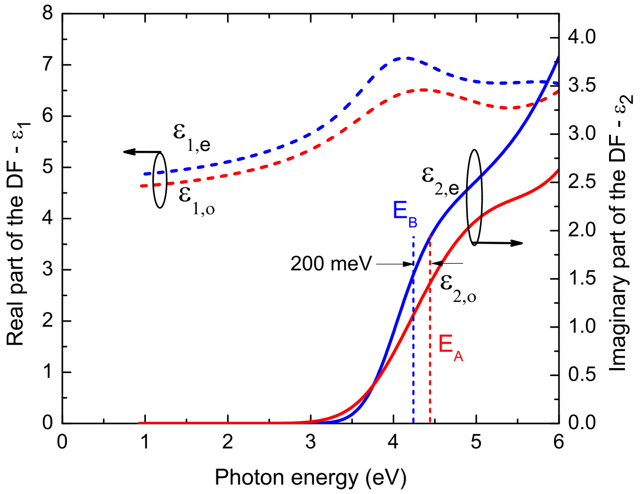

Figure 8.14: Complex ordinary and extraordinary DFs for $\mathrm{Al}_{0.8}\mathrm{In}_{0.2}\mathrm{N}$ alloy.

DF	ε_∞	A_G	E_G (eV)	A_H (eV)	E_H (eV)
$\varepsilon_{1,o}$	4.57	3.04	4.13	28.56	11.79
$\varepsilon_{1,e}$	4.80	3.16	4.01	29.64	12.48

Table 8.5: Ordinary and extraordinary high-energy dielectric constants for sample SN and fitting parameters of Eq. (3.22).

device design. The dispersion of ε_1 for non-polar AlInN sample in the transparent region (below the band gap) is expressed by the Eq. 3.22, as it was described in Chapter 3.2.

The ordinary and extraordinary high-frequency dielectric constants ($\varepsilon_{\infty,o}$ and $\varepsilon_{\infty,e}$) values together with the model parameters are represented in Tab. 8.5. By using the expression $n_{1,j} = \sqrt{\varepsilon_{1,j}}$ (j=e,o) (which is valid in the transparent region) and Eq. (3.22), we present the refractive indices $n_{1,o}$ and $n_{1,e}$ for $Al_{0.8}In_{0.2}N$ as a function of photon energy together with GaN and AlN for comparison in Fig. 8.15. The extraordinary refractive indices for AlInN as well as for GaN and AlN have a higher values in the transparent region, indicating the positive birefringence. The difference n_e-n_o for $Al_{0.8}In_{0.2}N$ was found to be 0.068 at photon energy of 3 eV. The GaN extraordinary and ordinary refractive indices cross approaching the band gap, while the indices for AlInN alloy diverge, as it can be observed in Fig. 8.15.

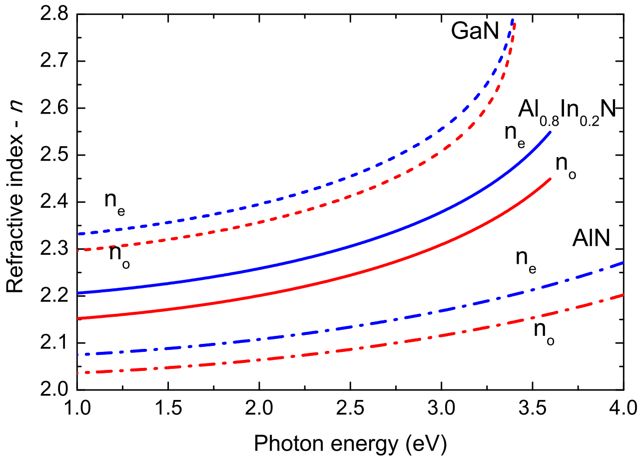

Figure 8.15: Ordinary and extraordinary refractive indices dispersion for $Al_{0.8}In_{0.2}N$ alloy. For comparison, dashed and dash dotted lines show the refractive indices for GaN [155] and AlN [77], respectively.

8.5 Summary of Chapter 8

The optical properties of the AlInN films nearly lattice matched to a GaN were investigated. The isotropic DFs and their analytical representations were demonstrated in the photon energy range 1-10 eV. The isotropic DF was also measured in the extended energy range up to 18 eV for InAnN sample with 14.3% In content. The critical points of the band structure were observed in the high-ernergy range. The fit of the analytical model to the experimental DFs allowed to estimate the band gap E_A, i.e., the transition from Γ_9^v valence band to the Γ_7^c conduction band. The strain-corrected band-gap values were obtained after applying the $\mathbf{k{\cdot}p}$ method. The strain-free band-gap E_A bowing parameter was found to be composition dependent and is expressed as b_A=6.24/(1+1.13$\cdot x^2$), where x is an In content. The investigation of an a-plane AlInN sample with In content of 20% gave an access to both ordinary and extraordinary DFs. The strong optical anisotropy was observed for the a-plane sample in the whole investigated range 1-6 eV. The difference between the estimated band gaps for two configurations $\boldsymbol{E}\perp\boldsymbol{c}$ and $\boldsymbol{E}\|\boldsymbol{c}$ was found to be ∼200 meV.

9 Optical properties of quaternary AlInGaN alloys

In previous Chapters, the strain-free band-gap bowing parameters, which allow to determine the band gap in the whole compositional range, were determined for the ternarnary InGaN and AlInN alloys. Now, the question arises: is it possible to find a band-gap bowing parameter for the quaternary alloy? The $\mathrm{Al}_x\mathrm{In}_y\mathrm{Ga}_{1-x-y}\mathrm{N}$ band gap can be tuned with a higher degree of freedom by changing the Al, In, or Ga content. Moreover, the composition determination in the quaternary alloy becomes more complicated by applying HRXRD. Alternative characterization techniques are needed (e.g., Rutherford backscattering spectroscopy analysis). In this Chapter, the isotropic DFs and their analytical representations of the (0001)-oriented AlInGaN films will be presented in the energy range from 1 eV up to 10 eV. By employing the known bowing parameters of the ternary alloys, the empirical expression will be developed that allows to calculate the band-gap and high-energy inter-band transitions for the quaternary AlInGaN alloys in the whole compositional range. The calculated AlInGaN band-gap values will be compared with both experimental data obtained by SE and the *ab initio* calculated data for uniform alloy.

Figures 9.1-9.7, 9.9 and Tables 9.2-9.4, 9.9 are reprinted with permission from Sakalauskas *et al*, Journal of Applied Physics, Vol. 110, Page 013102, (2011). Copyright 2011, American Institute of Physics.

9.1 Description of the investigated samples

The MOVPE was used to grow (0001)-oriented $\mathrm{Al}_x\mathrm{In}_y\mathrm{Ga}_{1-x-y}\mathrm{N}$ samples with Al content 0.23<x<0.64 and In content 0.02<y<0.13. The samples are denoted as S1 to S6 representing increasing Al content in this ordering. Samples S2, S4, and S6 provided by L. Rahimzadeh Khoshroo (RWTH Aachen University) were grown on c-plane sapphire substrate with 350 nm AlN buffer, 3.5 μm thick GaN buffer, and 1 nm AlN interlayer, as follows. Samples S1, S3, and S5 provided by B. Reuters (RWTH Aachen University) were grown analogically, except that GaN buffer thickness amounts to 3 μm and AlN interlayer is not applied. The AlInGaN layer thickness varies from 77.5 to 140.6 nm as determined by SE. The HRXRD measurements revealed pseudomorphic growth of the AlInGaN films on GaN/sapphire templates. Lattice parameters of GaN buffer layers, as determined by HRXRD, were evaluated to be a=3.182 Å and c=5.190 Å. The Rutherford backscattering spectroscopy (RBS) analysis was performed to determine the alloy composition (x, y), as listed in Tab. 9.1. The growth details of these studied samples can be found elsewhere [10, 156].

9.2 Optical selection rules for quaternary AlInGaN alloys

Before interpreting the DF, optical selection rules for quaternary AlInGaN material will be considered. First of all, the VB ordering around the Γ point of the Brillouin zone will be discussed. The valence band maximum (VBM) is splitted by the crystal field (Δ_{cf}) and spin-orbit interaction (Δ_{so}) into three two-fold-degenerate VBs with Γ_9^{v}, Γ_{7-}^{v}, and Γ_{7+}^{v} symmetry, as it was discussed in Chapter 2.

Because the Δ_{so} values for the binaries are almost identical, only special attention should be paid to the crystal field. Valence band crossing for the $\mathrm{Al}_x\mathrm{In}_y\mathrm{Ga}_{1-x-y}\mathrm{N}$ alloy occurs at Δ_{cf}=0 eV. Assuming that the $\mathrm{Al}_x\mathrm{In}_y\mathrm{Ga}_{1-x-y}\mathrm{N}$ crystal-field splitting energy is interpolated by using the following expression:

$$Q_{\mathrm{AlInGaN}}(x,y) = (1-x-y)\cdot Q_{\mathrm{GaN}} + x\cdot Q_{\mathrm{AlN}} + y\cdot Q_{\mathrm{InN}}, \tag{9.1}$$

where Q_{InN}, Q_{GaN}, and Q_{AlN} correspond to InN, GaN, and AlN crystal-field splitting energies, respectively, the crystal-field splitting energy is obtained -144 meV<Δ_{cf}<-28 meV, as indicated with dashed lines in Fig. 9.1(a) for the investigated samples ($0.23 < x < 0.64$ and $0.02 < y < 0.13$). The band ordering for the alloys studied here is the same as for AlN, i.e., the uppermost VB is characterized by Γ_{7+}^{v} symmetry as shown in Fig. 9.1(b).

By applying the **k·p** method, it is possible to calculate the relative valence band energy and the oscillator strengths for AlInGaN alloys. All parameters used in the calculations are interpolated from Eq. 9.1 by using the GaN, AlN, and InN endpoint values. The **k·p** method is described in Chapter 2 and the parameters for **k·p** calculations are employed from Table 2.1 in Chapter 2.

For the investigated AlInGaN samples, the transitions from the Γ_9^{v} valence band to the Γ_7^{c} conduction band (labeled A) and from Γ_{7-}^{v} to Γ_7^{c} (labeled C) exhibit strong

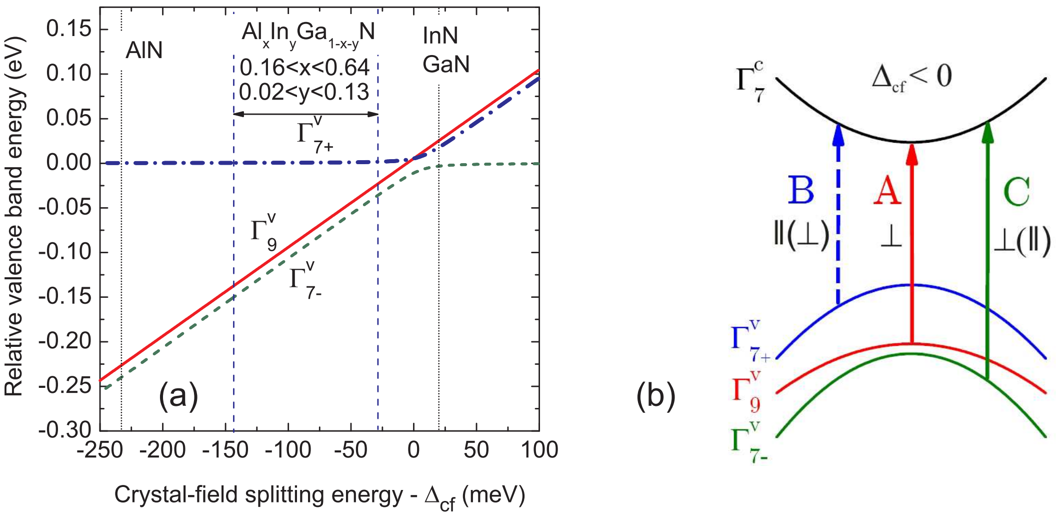

Figure 9.1: VB ordering for the AlInGaN alloy system as a function of crystal-field splitting energy (Δ_{so}=13 meV). The dashed lines indicate the calculated crystal-field splitting energy range for studied AlInGaN samples (a); Simplified scheme of transitions A, B, and C (for $\Delta_{\mathrm{cf}} < 0$). Symbols $\perp$ and $\|$ indicate strong transition probability, meanwhile symbols $(\perp)$ and $(\|)$ indicate weak transition probability for the respective polarization states (b).

relative oscillator strengths only for the configuration $\boldsymbol{E}\perp\boldsymbol{c}$. Thus, by measuring c-plane AlInGaN samples with an ellipsometer (almost $\boldsymbol{E}\perp\boldsymbol{c}$), these transitions dominate the optical response. In contrast, the transition from Γ^{v}_{7+} to Γ^{c}_{7} (labeled B) is strongly allowed only for the configuration $\boldsymbol{E}\|\boldsymbol{c}$. The simplified valence band ordering scheme sketched in Fig. 9.1(b) shows that transition B stems from the topmost valence band, but its oscillator strength is weak, thus, it is hardly detectable in the ordinary and isotropic DFs.

It is important to mention that an in-plane strain in the AlInGaN films can also induce VB order and oscillator strength changes. Figure 9.2(a) shows the deduced relative valence band ordering as a function of in-plane strain ϵ_{xx} for sample S2. The VB crossing occurs at an in-plane strain of ≈-0.005. By increasing a compressive strain, the relative oscillator strength for transition C decreases, while it increases for the transition B as presented in Figure 9.2(b).

The in-plane strain values (ϵ_{xx}) are listed in Table 9.1. The determined ϵ_{xx} values vary from -9.82×10^{-4} to 8.08×10^{-3}. According to the assumption that the parameters used in $\mathbf{k}\cdot\mathbf{p}$ calculations were interpolated using the Eq. 9.1 and considering the evaluated in-plane strain values, one can postulate that for the investigated samples the transition A and C will dominate the optical response detected by SE.

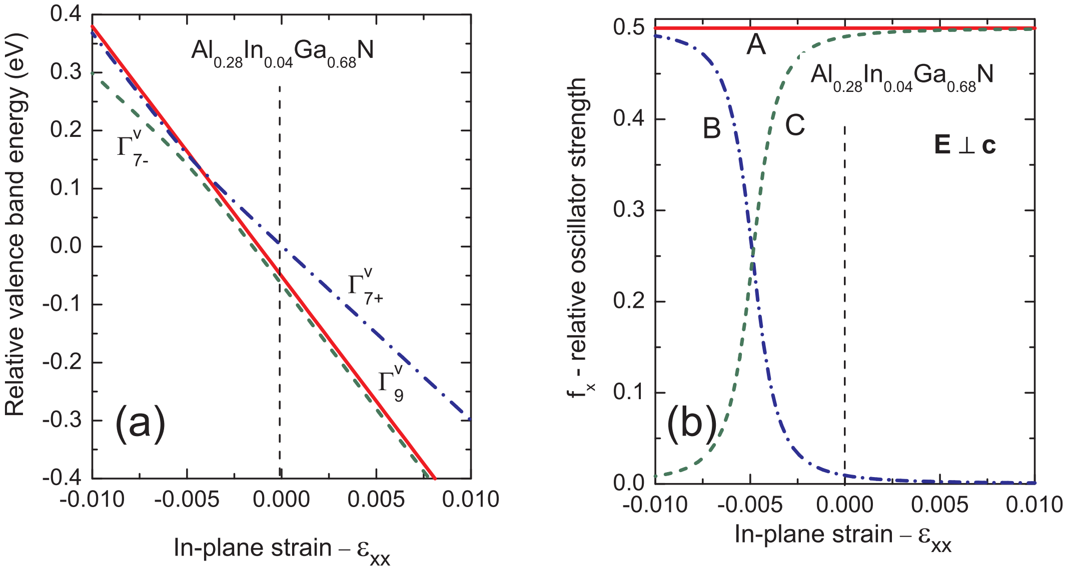

Figure 9.2: Relative VB ordering (a) and oscillator strength for configuration $\boldsymbol{E} \perp \boldsymbol{c}$ (b) as a function of in-plane strain (sample S2).

9.3 AlInGaN dielectric function and its analytical representation

The obtained isotropic DFs for samples S1, S3, and S5 are presented in Fig. 9.3. Pronounced features attributed to critical points of the band structure are found in the high-energy range of ε_2. They have a strong impact on the dispersion of ε_1 at lower energies. It is clearly seen in Fig. 9.3 that with decreasing Al content in the AlInGaN alloy, the absorption onset (imaginary part of the dielectric function - ε_2) redshifts. Following the Kramers-Kronig relation, the ε_1 peak also shifts to the lower energies.

Accurate analytical form of the DF is necessary for device modeling and analysis of the material optical properties. In this section, it will be shown that the DFs of

Sample	x/y (RBS)	ϵ_{xx}
S1	0.23/0.02	$1.08{\cdot}10^{-3}$
S2	0.28/0.04	$1.09{\cdot}10^{-4}$
S3	0.41/0.03	$4.39{\cdot}10^{-3}$
S4	0.41/0.05	$2.20{\cdot}10^{-3}$
S5	0.56/0.03	$8.08{\cdot}10^{-3}$
S6	0.64/0.13	$-9.82{\cdot}10^{-4}$

Table 9.1: Al/In composition values (x/y) evaluated by RBS as well as calculated in-plane strain values.

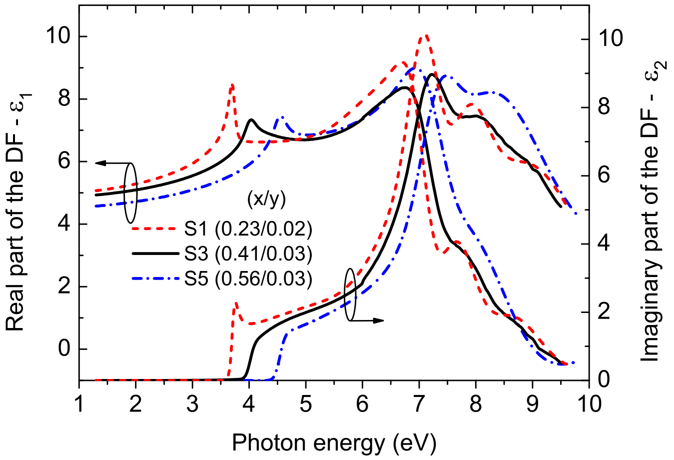

Figure 9.3: Isotropic DFs for samples S1, S3, and S5.

AlInGaN can be represented analytically by using the analytical model presented in Chapter 3.2 (as it was already demonstrated in previous chapters for ternary AlInN and InGaN alloys).

The analytical expressions (Eq. 3.18 and Eq. 3.21 in Chapter 3.2) were fitted simultaneously with the experimentally obtained AlInGaN real and imaginary parts of the DF using the least square method. By fitting the analytical model to the experimental DF, the band-gap (E_A) and high-energy inter-band transitions (E_1, E_2, and E_3) were obtained. The parameter E_C was fixed to be $E_A + 0.013$ eV. The fitting parameters are listed in Tab. 9.2. The experimental complex DF and its analytical form for sample S3 are represented in Fig. 9.4.

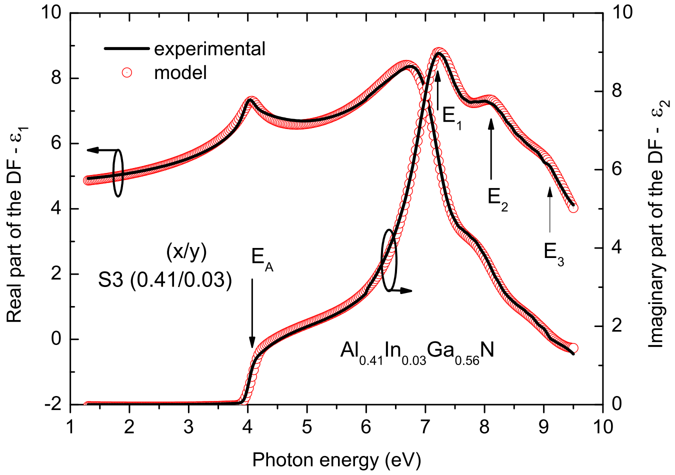

Figure 9.4: Experimental and calculated DF for sample S3.

Table 9.2: Fitting parameters for the DF analytical model.

Fitting parameter	Sample S1	S2	S3	S4	S5	S6
A_0	1.73	1.21	1.86	1.14	1.43	0.53
A_1 (eV^2)	45.90	44.09	46.02	39.86	42.93	39.18
A_2 (eV^2)	22.26	47.69	32.39	46.45	38.77	70.38
A_3 (eV^2)	65.26	87.32	46.44	91.90	58.97	91.16
A_{BS} eV^2)	$2.7{\cdot}10^{-1}$	$6{\cdot}10^{-2}$	$2{\cdot}10^{-4}$	$2.5{\cdot}10^{-1}$	$5.8{\cdot}10^{-2}$	$6.5{\cdot}10^{-1}$
A_{CS} (eV)	1.17	1.07	1.20	1.05	1.68	0.61
A_P (eV)	216.52	176.32	154.81	208.28	231.45	273.86
E_1 (eV)	7.06	7.09	7.20	7.17	7.39	7.49
E_2 (eV)	7.99	7.99	8.12	8.03	8.25	8.40
E_3 (eV)	9.05	9.12	9.05	9.09	9.03	9.48
E_{A} (eV)	3.74	3.74	4.06	3.95	4.56	4.27
E_{C} (eV)	E_A+0.013	E_A+0.013	E_A+0.013	E_A+0.013	E_A+0.013	E_A+0.013
E_{P} (eV)	19.61	15.38	17.14	16.28	18.40	16.46
Γ_0 (eV)	$2.6{\cdot}10^{-2}$	$4.2{\cdot}10^{-2}$	0.11	$5.5{\cdot}10^{-2}$	$3.7{\cdot}10^{-2}$	$1.5{\cdot}10^{-2}$
Γ_1 (eV)	0.92	0.89	1.11	0.94	1.07	1.18
Γ_2 (eV)	0.84	1.32	1.29	1.40	1.33	1.65
Γ_3 (eV)	1.99	2.11	1.81	2.30	1.91	2.46
Γ_{BS}(eV)	0.09	0.07	1.72	1.66	6.84	1.63
Γ_{CS}(eV)	0.05	0.14	0.12	0.21	0.12	0.12
R (meV)	12	19	12	19	29	23
b	-2.43	-2.45	-1.79	-2.85	-2.84	-4.05

9.3.1 Compositional dependence of the characteristic transition energies

In this section, the empirical expression, which allows to describe the band-gap E_{A} and high-energy inter-band transitions E_1, E_2, and E_3 of quaternary AlInGaN alloys in the whole composition range (x, y), will be proposed. By employing the ternary alloy bowing parameters and binary endpoint values, determined in previous studies (listed in Tab. 9.3 and 9.4, respectively), and applying the following expressions [57]:

$$\begin{aligned} E_{\mathrm{j=A,1,2,3}}^{\mathrm{AlInGaN}} &= (1-x-y)\cdot E_{\mathrm{j}}^{\mathrm{GaN}} + x\cdot E_{\mathrm{j}}^{\mathrm{AlN}} \\ &\quad +y\cdot E_{\mathrm{j}}^{\mathrm{InN}} - b_{\mathrm{j}}^{\mathrm{AlGaN}}\cdot x\cdot(1-x) \\ &\quad -b_{\mathrm{j}}^{\mathrm{InGaN}}\cdot y\cdot(1-y) - b_{\mathrm{xy}}\cdot x\cdot y, \end{aligned} \tag{9.2}$$

$$b_{\mathrm{xy}} = b_{\mathrm{j}}^{\mathrm{AlInN}} - b_{\mathrm{j}}^{\mathrm{AlGaN}} - b_{\mathrm{j}}^{\mathrm{InGaN}}, \tag{9.3}$$

the band-gap (E_{A}) and high-energy transition energies (E_1, E_2 and E_3) are calculated.

9.3.1.1 Band gap

The studied AlInGaN films were pseudomorphically grown on GaN buffer layers, therefore, they experience compressive or tensile strain (depending on the alloy composition) which causes the strain induced band-gap shift $\Delta E_{\mathrm{A}}^{\mathrm{strain}}$. The strain induced band-gap shift $\Delta E_{\mathrm{A}}^{\mathrm{strain}}$ is calculated by applying **k·p** method, as it was described in Chapter 2. All $\mathrm{Al}_x\mathrm{In}_y\mathrm{Ga}_{1-x-y}\mathrm{N}$ parameters (spin-orbit, crystal-field splitting energy, deformation potentials, lattice parameters, and elastic stiffness constants) used for **k·p** calculations are deduced from InN, GaN and AlN parameters by using a linear interpolation according to Eq. 9.1.

The strain-induced energy shift $\Delta E_{\mathrm{A}}^{\mathrm{strain}}$ calculated from the **k·p** model around the Γ point of the Brillouin zone, transition energy E_{A} obtained from the DF (influenced by strain), and derived unstrained transition energy $E_{\mathrm{A}}^{\mathrm{relax}} = E_{\mathrm{A}} - \Delta E_{\mathrm{A}}^{\mathrm{strain}}$ values are summarized in Table 9.5.

Now, the band-gap values will be calculated from Eq. 9.2 and will be compared with both *ab initio* and experimental data. The transition E_{A} endpoint values are 0.675 eV,

	b_A (eV)	b_1 (eV)	b_2 (eV)	b_3 (eV)
InGaN	1.65	1.06	0.99	1.04
AlGaN	0.9 [84]	0.2 [84]	0.1 [84]	0.5 [84]
AlInN	$b_A(x)=\frac{A}{1+C\cdot\ x^2}$ A=6.24; C=1.13	1.59	2.52	0

Table 9.3: Bowing parameters for ternary alloys.

Table 9.4: Endpoint values.

	E_{A} (eV)	E_1 (eV)	E_2 (eV)	E_3 (eV)
InN	0.675 [121]	5.38 [121]	6.12 [121]	7.95 [121]
GaN	3.435 [24]	6.99 [84]	7.96 [84]	9.25 [84]
AlN	6.24 [30]	7.97 [84]	8.95 [84]	8.84 [84]

Table 9.5: Experimental and calculated transition energies E_{A}.

Sample	expt. E_{A} (eV)	$\Delta E_{\mathrm{A}}^{\mathrm{strain}}$ (eV)	$E_{\mathrm{A}}^{\mathrm{relax}}$ (eV)	calc. E_{A} (eV)
S1 (0.23/0.02)	3.74	-0.01	3.75	3.82
S2 (0.28/0.04)	3.74	∼0	3.74	3.83
S3 (0.41/0.03)	4.06	-0.04	4.10	4.20
S4 (0.41/0.05)	3.95	-0.02	3.97	4.09
S5 (0.56/0.03)	4.56	-0.06	4.62	4.61
S6 (0.64/0.13)	4.27	0.01	4.26	4.32

3.435 eV, and 6.24 eV for InN, GaN, and AlN, respectively, as listed in Tab. 9.4. The bowing parameter values (b_{A}) for ternary alloys are employed from Tab. 9.3. By using E_{A} endpoint values and ternary alloy bowing parameters (b_{A}) in Eq. 9.2, it is possible to generate the band-gap values in the whole compositional range (x, y), as shown in Figure 9.5.

The calculated AlInGaN band-gap values from Eq. 9.2 together with the experimentally determined band-gap values are summarized in Table 9.5. The calculated and experimental values are in good agreement. Figure 9.6 shows the band gap as a function of x and y in colour map. The black circles indicate the experimentally determined values from SE.

The *ab initio* calculated band-gap values for the uniform (not clustered) $\mathrm{Al}_{0.62-y}\mathrm{In}_y$ $\mathrm{Ga}_{0.38}\mathrm{N}$ alloy in the work of Gorczyca *et al.* [128] are also in good agreement with the generated values from Eq. 9.2, as shown in Figure 9.7.

Table 9.6: Experimental PL peak values E_{PL}, band-gap values determined from ellipsometry E_{A}, calculated difference $E_{\mathrm{A}}^{\mathrm{relax}}$, and calculated difference $\Delta \mathrm{E}_{AB}$ from ical expression (9.4).

Sample	E_{PL} (eV)	$E_{\mathrm{PL}}^{\mathrm{relax}}$ (eV)	$E_{\mathrm{PL}}^{\mathrm{relax}}$-$E_{\mathrm{A}}^{\mathrm{relax}}$ (eV)	ΔE_{AB} (Eq. 9.4) (eV)
S1(0.23/0.02)	3.69	3.71	-0.04	-0.044
S3(0.41/0.03)	3.96	4.05	-0.05	-0.090
S5(0.56/0.03)	4.32	4.49	-0.13	-0.127

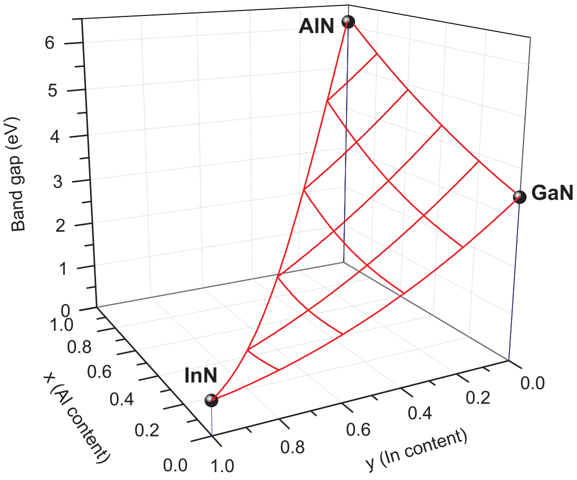

Figure 9.5: AlInGaN band gap as a function of Al content (x) and In content (y) generated using Eq. 9.2.

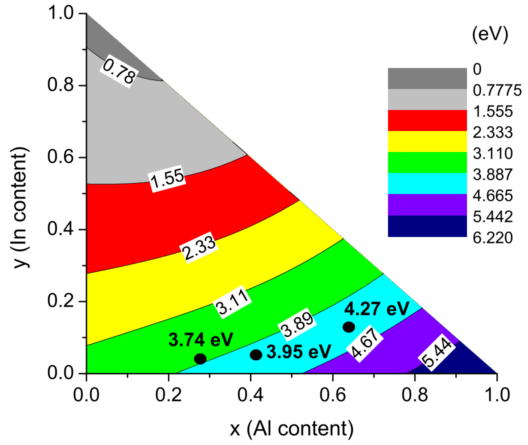

Figure 9.6: Colour map of the AlInGaN band gap as a function of Al content (x) and In content (y) generated using Eq. 9.2. Black circles indicate the experimental data points determined from SE for samples S2, S4, and S6.

Additionally, the PL measurements were performed by the research group of prof. G.P. Yablonskii (Stepanov Institute of Physics, National Academy of Science Belarus) at RT for samples S1, S3, and S5 by using an excitation wavelength λ=213 nm and excitation power of ~300 kW/cm^3. Fig. 9.8 shows the PL peak values obtained at RT (indicated by triangles) together with the band-gap values determined from SE at RT (indicated with squares) as a function of lattice parameter a. In order to have a better comparison, PL peak values (E_{PL}) and strain-corrected PL values ($E_{\mathrm{PL}}^{\mathrm{relax}}$) together with the calculated difference ($E_{\mathrm{PL}}^{\mathrm{relax}}$-$E_{\mathrm{A}}^{\mathrm{relax}}$)) are listed in Table 9.6. One can observe the difference between PL and SE values, it even mounts up to -130 meV for sample S5 with the highest Al content. To understand this difference between PL and SE values, the same explanation will be taken as it was done for AlInN samples in Chapter 8, section

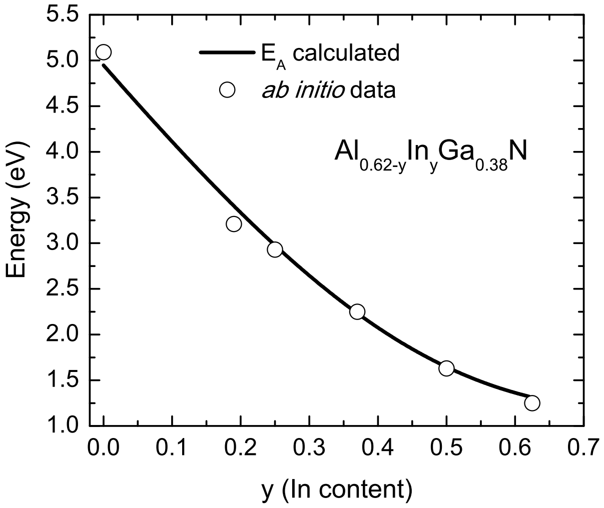

Figure 9.7: Band gap calculated from Eq. 9.2 as a function of In content (y) for $Al_{0.62-y}In_yGa_{0.38}N$. The open circles indicate the *ab initio* calculated band-gap values [128].

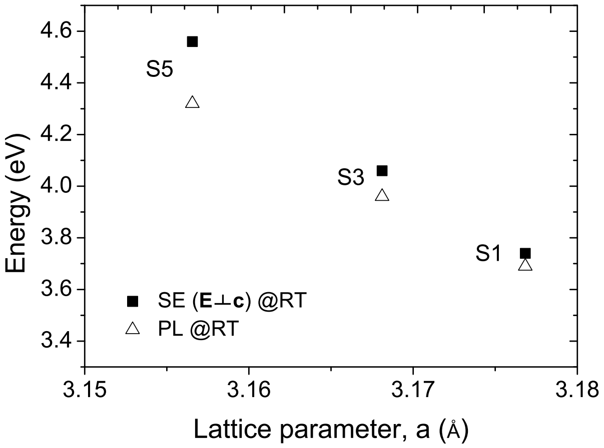

Figure 9.8: Experimental PL peak values E_{PL} (triangles) together with the band-gap values E_{A} obtained from SE (squares) at RT as a function of lattice parameter a.

8.3.2. It is assumed that the PL peak value corresponds to the band-to-band transition from the conduction band to the topmost valence band. For the investigated AlInGaN alloys the crystal-field splitting energy is negative $\Delta_{\mathrm{cf}} < 0$. The topmost valence band is Γ^{v}_{7+}. The following expression to calculate the difference between the transitions A and B ($\Delta E_{\mathrm{AB}} = E_{\mathrm{B}} - E_{\mathrm{A}}$) is proposed:

$$\Delta E_{\mathrm{AB}}(x,y) = 0.01 \cdot (1 - x - y) + (-0.21) \cdot x + 0.03 \cdot y - 0.83 \cdot x \cdot y. \tag{9.4}$$

Here, the ΔE_{AB} bowing parameter of 0.83 eV for the AlInN alloy is employed, as it was determined from Chapter 8, section 8.4. The endpoint ΔE_{AB} values of ~0.01 eV [155], ~-0.21 [30, 77], and ~0.03 [68] are used for binary GaN, AlN, and InN. Table 9.6

x/y	E_{PL}@RT (eV)	calc. E_{A} (Eq. 9.2) (eV)
0.08/0.01	3.61 [157]	3.56
0.08/0.02	3.48 [157]	3.51
0.08/0.015	∼3.54 [157]	3.53
0.05/0.01	3.508 [158]	3.499
0.075/0.04	3.39 [159]	3.41
0.06/0.15	2.90 [160]	2.90
0.01/0.08	3.20 [160]	3.12
0.1/0.001	3.55 [160]	3.64
0.02/0.08	3.14 [161]	3.14

Table 9.7: Experimental PL peak values measured at RT by different groups and calculated transition energies E_{A} from Eq. 9.2.

compares the calculated ΔE_{AB} with the $E_{\mathrm{PL}}^{\mathrm{relax}}$-$E_{\mathrm{A}}^{\mathrm{relax}}$ values and good agreement is found for samples S1 and S5.

Moreover, several band-to-band PL peak data for $\mathrm{Al}_x\mathrm{In}_y\mathrm{Ga}_{1-x-y}\mathrm{N}$ with x<0.1 (measured at RT by other research groups) were collected and listed in Table 9.7. Since Al content in these samples is low (x<0.1), thus, the crystal-field splitting energy will be small for these samples. Consequently, the PL peak value is expected to be very close to the transition E_{A}. Table 9.7 compares the PL peak values with the calculated transition energy E_{A} values. Indeed, the PL peak values are very close to the calculated E_{A} values. It is important to mention that for the PL peak values presented in Tab. 9.7, the strain influence was not taken into consideration.

9.3.1.2 High-energy inter-band transitions

In this section, the experimentally determined high-energy inter-band transitions (E_1, E_2, and E_3), which correspond to the CPs of the band structure, will be compared with the calculated values from Eq. 9.2. It is worth to emphasize that in previous ellipsometry studies conducted on binary nitrides [1,68], the strain influence on the high-energy inter-band transitions was not noticed. Therefore, we assume that the high-energy inter-band transitions for quaternary alloys will not be influenced by strain.

By employing the transition energies E_1, E_2, and E_3 endpoint values (listed in Tab. 9.4) and the bowing parameters of ternary alloys (listed in Tab. 9.3) in Eq. 9.2, it is possible to describe the transition energies in the whole composition range (x, y). The calculated values are in good agreement with the experimental values (summarized in Table 9.8).

Table 9.8: Experimental (obtained from the DF modelling) and calculated (from Eq. 9.2) high-energy inter-band transition energies E_1, E_2, and E_3.

Sample	expt. E_1 (eV)	calc. E_1 (eV)	expt. E_2 (eV)	calc. E_2 (eV)	expt. E_3 (eV)	calc. E_3 (eV)
S1 (0.23/0.02)	7.06	7.13	7.99	8.11	9.05	9.03
S2 (0.28/0.04)	7.09	7.11	7.99	8.09	9.12	8.96
S3 (0.41/0.03)	7.20	7.26	8.12	8.24	9.05	8.91
S4 (0.41/0.05)	7.17	7.20	8.03	8.17	9.09	8.88
S5 (0.56/0.03)	7.39	7.40	8.25	8.38	9.03	8.85
S6 (0.64/0.13)	7.49	7.21	8.40	8.10	9.48	8.71

9.3.2 Dispersion below the band gap and high-frequency dielectric constant

In this section, the high-frequency dielectric constants ε_∞ will be derived for the investigated AlInGaN samples. The dispersion of ε_1 for AlInGaN samples in the transparent region (below the band gap) is expressed by the analytical expression as described in Chapter 3.2 by Eq. 3.22.

The high-frequency dielectric constants together with the fitted parameters of Eq. 3.22 are represented in Tab. 9.9. In Figure 9.9, the ε_1 values are presented as a function of photon energy for AlInGaN samples together with AlN and GaN for comparison. The precise ε_1 (or refractive index - n) values are needed for optoelectronic device development.

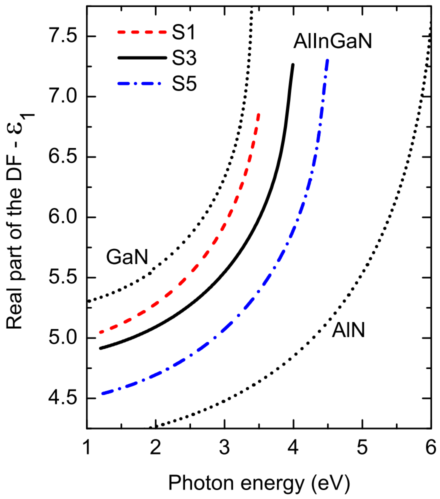

Figure 9.9: Real part of the DF (ε_1) for samples S1, S3, and S5 in the transparent region (below the band gap).

Sample	ε_∞	A_G	E_G (eV)	A_H (eV)	E_H (eV)
S1	4.93	1.89	3.67	38.74	8.42
S2	4.90	2.20	3.76	38.05	9.08
S3	4.82	1.96	4.07	41.72	9.68
S4	4.85	1.49	3.87	41.80	8.60
S5	4.46	2.04	4.57	36.35	8.96
S6	4.55	2.25	4.47	39.12	11.01

Table 9.9: High-frequency dielectric constant and fitted parameters.

9.4 Summary of Chapter 9

The isotropic DFs and their analytical representations were presented for the (0001)-oriented quaternary AlInGaN alloys in the photon energy range 1-10 eV. Critical points of the band structure E_1, E_2, and E_3 were observed in the high-energy range. With the knowledge of the ternary InGaN, AlInN, and AlGaN alloy band-gap bowing parameters, the empirical expression was developed that allows to calculate the band-gap and high-energy inter-band transitions for the quaternary AlInGaN alloy. The band-gap values calculated from this empirical expression are in good agreemnent with both experimental SE and the *ab initio* data.

10 Summary

In this work, optical properties of wurtzite structure InN and related alloys were investigated. The spectroscopic ellipsometer (SE) was used as the main characterization tool for the analysis of the optical properties. The mid-IR range (300 - 2000 cm^{-1}) was investigated by applying an IR-SE. A commercial variable angle ellipsometer together with a synchrotron ellipsometer allowed to cover the spectral range from the near IR up to VUV (0.56 - 18 eV).

The dielectric functions (DFs) as well as the layer thicknesses of the investigated samples were obtained by applying the multilayer optical model. The so called ellipsometric parameters Ψ and Δ obtained from the SE measurements are fitted by using a multilayer model. A multilayer model includes a substrate and buffer layers with the known optical constants. The surface or interface roughness is taken into consideration by applying an effective-medium approximation. By analyzing the polar sample (i.e., c-axis is perpendicular to the sample's surface plane), the so called *isotropic* DF is obtained that is very close to the ordinary DF [78]. For non-polar samples (i.e., the c-axis is parallel to the sample's surface plane) it is possible to extract both *ordinary* and *extraordinary* DFs.

The DF reflects optical properties of the investigated sample, e.g., a band gap and critical points (CPs) of the band structure (high-energy inter-band transitions). However, a band gap, can not be extracted directly from the absorption onset (imaginary part of the DF around the gap). For example, an InN material is a low band gap degenerate semiconductor with the Fermi level above the conduction band minimum. The effects, such as the band-gap renormalization and the Burstein-Moss shift, must be taken into consideration. The optical selection rules also must be considered. The crystal field and spin-orbit interaction split the valence band maximum into three two-fold-degenerate valence bands with Γ^{v}_{7+}, Γ^{v}_{7-}, and Γ^{v}_{9} symmetry. For instance, by measuring a polar sample by SE, the configuration is almost $\mathbf{E}\perp\mathbf{c}$. Therefore, only transitions allowed for this configuration are determined for polar samples. Meanwhile, by measuring the non-polar sample, one can determine the transitions allowed for both configurations

E⊥**c** and **E**||**c**. And finally, the strain influence on the band gap must be accounted for. The investigated InN and In(Al,Ga)N samples are grown on the different substrates and different buffer layers. Due to a lattice mismatch and different thermal expansion coefficients, the grown epilayer experience compressive or tensile strain. A **k**·**p** method is used to calculate the strain induced band-gap shift.

Moreover, the analytical DF model developed by Goldhahn *et al* [162] was successfully applied for the ternary InGaN and AlInN alloys as well as for the quaternary AlInGaN alloys in the energy range from 1 eV up to 10 eV. The fit of the analytical model to the experimental DFs allows to determine the band gap (E_A, E_B) as well as the high-energy inter-band transitions (E_1, E_2, and E_3). The estimated high-energy inter-band transition energies are in good agreement with the values determined from the third-derivative method developed by Aspnes [134]. For the analytical representation of the DF in the transparent range and the high-frequency dielectric constant estimation, the analytical model developed by Shokhovets *et al* [85] is applied.

The intrinsic band gap and the carrier concentration for the unintentionally and carbon doped (0001)-oriented InN samples are evaluated by solving a self-consistent problem that includes the IR-SE ellipsometry data analysis and the imaginary DF around the band gap calculation, as it was proposed by Schley *et al* [121]. The intrinsic strain-free fundamental band gap for the investigated InN samples was evaluated to be ∼0.65 eV. From the analysis, it was shown that for the carbon doped samples the electron concentration increases linearly by increasing the CBr_4 dopant pressure during the MBE growth process. For the unintenionally doped InN samples the isotropic DFs were extracted up to 9.5 eV. Characteristic peaks of the band structure denoted as D, E_1, E_2, E_3 and E_4 were observed. For the selected carbon doped InN samples, the isotropic DFs were determined in the extended range up to 17 eV. The additional CPs of the band-structure E_5 and E_6 were observed in the extended energy range. Despite the different in-plane strain in the different InN epilayers, no shift of the energetic positions of the CPs were observed.

For the (0001)-oriented $In_xGa_{1-x}N$ samples with $0.15<x<0.19$, the isotropic DFs were obtained in the range 1-10 eV. From the fit of the analytical model to the experimental DFs, the fundamental band gaps were estimated. The band gap values were strain corrected by applying the **k**·**p** formalism. Combining the results for In-rich InGaN samples obtained in the work of Schley *et al* [121], the strain-free band-gap bowing parameter was estimated to be 1.65±0.07 eV. The high-energy inter-band transitions E_1, E_2, E_3 were also obtained from the analytical model fit and the bowing parameters were evaluated to be ~1 eV. Moreover, the sample with In content of 15.2% was measured by SE in the extended energy range up to 17 eV and the critical points E_4 and E_5 were observed at energies of 10.8 eV and 12.6 eV, respectively.

An attention must be paid for the optical selection rules of the Al-rich AlInN and AlInGaN alloys. Since the AlN has a huge negative crystal-field splitting energy of Δ_{cf}=-212 meV [30], it is expected that the Al-rich AlInN and AlInGaN alloys will have a large splitting between Γ^{v}_{7+} and Γ^{v}_{9}, Γ^{v}_{7-} VBs at the Γ point. For the material with a negative crystal field energy, the transition from the top-most valence band $\Gamma^{\mathrm{v}}_{7}+$ to the conduction band Γ^{c}_{7} (denoted as E_{B}) is strongly allowed for a configuration $\mathbf{E}\|\mathbf{c}$. While the transitions from the VBs Γ^{v}_{9} and Γ^{v}_{7-} to the conduction band Γ^{c}_{7} (denoted as E_{A} and E_{C}, respectively) are strongly allowed for a configuration $\mathbf{E}\perp\mathbf{c}$. The splitting between Γ^{v}_{9} and Γ^{v}_{7-} caused by a spin orbit-interaction is very small, therefore it is not resolved in the spectroscopic ellipsometry measurements and only a transition E_{A} can be probed.

For the series of polar Al-rich AlInN films nearly lattice matched to GaN, the transitions E_{A} ($\Gamma^{\mathrm{v}}_{9} \longrightarrow \Gamma^{\mathrm{c}}_{7}$) are determined from the fit of the analytical model to the experimental isotropic DF. The strain induced band gap shift was calculated by using the $\mathbf{k}\cdot\mathbf{p}$ method. By combining the latter data and the data obtained for In-rich AlInN alloys from the work of Goldhahn *et al* [142], the strain-free band gap (E_{A}) bowing parameter was obtained to be 5.36±0.36 eV. However, it was noticed that the bowing curve with a bowing parameter of 5.36 eV does not describe well the experimental data points in the whole compositional range. Therefore, the new composition dependent bowing parameter $b_{\mathrm{A}} = b_{\mathrm{A}}(x) = 6.24/(1 + 1.13 \times x^2)$ was proposed. The composition dependent bowing parameter $b_{\mathrm{A}}(x)$ describes very well the experimental data points and is in a good agrrement with the *ab initio* calculated band gap values from the work of Gorczyca *et al* [128]. The high-energy inter-band transitions were also determined from the fit of the analytical model. The bowing parameters for high-energy transitions E_1, E_2, and E_3 were obtained to be 1.59 eV, 2.52 eV, and 0 eV, respectively. One AlInN sample with In content of 14.3% was measured in the extended energy range up to 18 eV, and the CPs E_4, E_5 and E_6 were observed at ~10.6 eV, ~12.5 eV, and ~14.2 eV, respectively.

In addition, a non-polar (11-20)-oriented $\mathrm{Al_{0.8}In_{0.2}N}$ was investigated and the ordinary and extraordinary DFs were determined in the spectral range between 1 eV and 6 eV. The strong optical anisotropy was observed in the whole investigated range. The extraordinary refractive indices for AlInN have a higher values in the transparent region, indicating a positive birefringence. The difference n_e-n_o for $\mathrm{Al_{0.8}In_{0.2}N}$ was found to be 0.068 at photon energy of 3 eV. The transitions E_A and E_B (fundamental band gap) were determined to be 4.44 eV and 4.24 eV, respectively. The difference between the transition E_A and E_B was estimated to be ΔE_AB=E_B-E_A=-200 meV, as it was expected for an Al-rich alloy due to the large negative crystal-field splitting energy of AlN [30].

Analogously as for the ternary alloys, the strain-free transition energies E_A and high-energy inter-band transitions E_1, E_2, and E_3 were determined for the (0001)-oriented quaternary $\mathrm{Al}_x\mathrm{In}_y\mathrm{Ga}_{1-x-y}\mathrm{N}$ alloys with $0.16<x<0.64$ and $0.02<y<0.13$. With the knowledge of the bowing parameters of ternary alloys InGaN, AlInN, and AlGaN [84], it was possible to develop an empirical equation that allows to determine the transition energy E_A as well as the high-energy inter-band transitions E_1, E_2, and E_3.

Bibliography

[1] E. Sakalauskas, P. Schley, J. Räthel, T. A. Klar, R. Müller, J. Pezoldt, K. Tonisch, J. Grandal, M. A. Sánchez-García, E. Calleja, A. Vilalta-Clemente, P. Ruterana, R. Goldhahn, *Optical properties of InN grown on Si(111) substrate*, Phys. Status Solidi A **207**, 1066 (2010).

[2] E. Sakalauskas, H. Behmenburg, C. Hums, P. Schley, G. Rossbach, C. Giesen, M. Heuken, H. Kalisch, R. H. Jansen, J. Bläsing, A. Dadgar, A. Krost, R. Goldhahn, *Dielectric function and optical properties of Al-rich AlInN alloys pseudomorphically grown on GaN*, J. Phys. D: Appl. Phys. **43**, 365102 (2010).

[3] E. Sakalauskas, H. Behmenburg, P. Schley, G. Gobsch, C. Giesen, H. Kalisch, R.H. Jansen, M. Heuken, R. Goldhahn, *Dielectric function of Al-rich AlInN in the range 1-18 eV*, Phys. Satus Solidi A **208**, 1517 (2011).

[4] E. Sakalauskas, B. Reuters, L. Rahimzadeh Khoshroo, H. Kalisch, M. Heuken, A. Vescan, M. Röppischer, C. Cobet, G. Gobsch, R. Goldhahn, *Dielectric function and optical properties of quaternary AlInGaN alloys*, J. Appl. Phys. **110**, 013102 (2011).

[5] E. Sakalauskas, M. Wieneke, A. Dadgar, G. Gobsch, A. Krost, R. Goldhahn, *Optical anisotropy of a-plane $Al_{0.8}In_{0.2}N$ grown on an a-plane GaN pseudosubstrate*, Phys. Status Solidi A **209**, 29 (2012).

[6] E. Sakalauskas, Ö Tuna, A. Kraus, H. Bremers, U. Rossow, C. Giesen, M. Heuken, A. Hangleiter, G. Gobsch, R. Goldhahn, *Dielectric function and bowing parameters of InGaN alloys*, Phys. Status Solidi B **249**, 485 (2012).

[7] P. Schley, J. Räthel, E. Sakalauskas, G. Gobsch, M. Wieneke, J. Bläsing, A. Krost, G. Koblmüller, J. S. Speck, R. Goldhahn, *Optical anisotropy of A- and M-plane InN grown on free-standing GaN substrates*, Phys. Status Solidi A **207**, 1062 (2010).

[8] I. Hotovy, J. Pezoldt, M. Kadlecikova, T. Kups, L. Spiess, J. Breza, E. Sakalauskas, R. Goldhahn, V. Rehacek, *Structural characterization of sputtered indium oxide films deposited at room temperature*, Thin Solid Films **518**, 4508 (2010).

[9] A. Kraus, S. Hammadi, J. Hisek, R. Buß, H. Jönen, H. Bremers, U. Rossow, E. Sakalauskas, R. Goldhahn, A. Hangleiter, *Growth and characterization of InGaN by*

RF-MBE, J. Cryst. Growth **324**, 72 (2011).

[10] B. Reuters, A. Wille, B. Holländer, E. Sakalauskas, N. Ketteniss, C. Mauder, R. Goldhahn, M. Heuken, H. Kalisch, A. Vescan, *Growth studies on quaternary AlInGaN layers for HEMT application*, J. Electron. Mater. (submitted).

[11] J. Wu, W. Walukiewicz, W. Shan, K. M. Yu, J. W. Ager, E. E. Haller, H. Lu, W. J. Schaff, *Effects of the narrow band gap on the properties of InN*, Phys. Rev. B **66**, 201403 (2002).

[12] J. Wu, W. Walukiewicz, W. Shan, K. M. Yu, J. W. Ager, S. X. Li, E. E. Haller, H. Lu, W. J. Schaff, *Temperature dependence of the fundamental band gap of InN*, J. Appl. Phys. **94**, 4457 (2003).

[13] P. Schley, R. Goldhahn, G. Gobsch, M. Feneberg, K. Thonke, X. Wang, A. Yoshikawa, *Influence of strain on the band gap energy of wurtzite InN*, Phys. Status Solidi B **246**, 1177 (2009).

[14] V. M. Polyakov, F. Schwierz, *Low-field electron mobility in wurtzite InN*, Appl. Phys. Lett. **88**, 032101 (2006).

[15] O. Kryliouk, *Pt-coated InN nanorods for selective detection of hydrogen at room temperature*, J. Vac. Sci. Technol. B **23**, 1891 (2005).

[16] Y.-S. Lu, C.-C. Huang, J. A. Yeh, C.-F. Chen, S. Gwo, *InN-based anion selective sensors in aqueous solutions*, Appl. Phys. Lett. **91**, 202109 (2007).

[17] V. Cimalla, B. Pradarutti, G. Matthäus, C. Brückner, S. Riehemann, G. Notni, S. Nolte, A. Tünnermann, V. Lebedev, O. Ambacher, *High efficient terahertz emission from InN surfaces*, Phys. Status Solidi B **244**, 1829 (2007).

[18] I. Wilke, R. Ascazubi, H. Lu, W. J. Schaff, *Terahertz emission from silicon and magnesium doped indium nitride*, Appl. Phys. Lett. **93**, 221113 (2008).

[19] W. Lim, J. S. Wright, B. P. Gila, S. J. Pearton, F. Ren, W.-T. Lai, L.-C. Chen, M.-S. Hu, K.-H. Chen, *Selective-hydrogen sensing at room temperature with Pt-coated InN nanobelts*, Appl. Phys. Lett. **93**, 202109 (2008).

[20] Y.-S. Lu, Y.-H. Chang, Y.-L. Hong, H.-M. Lee, S. Gwo, J. A. Yeh, *Investigation on -c-InN and a-InN:Mg field effect transistors under electrolyte gate bias*, Appl. Phys. Lett. **95**, 102104 (2009).

[21] N. Sofikiti, N. Chaniotakis, J. Grandal, M. Utrera, M. A. Sanchez-Garcia, E. Calleja, E. Iliopoulos, A. Georgakilas, *Direct immobilization of enzymes in GaN and InN nanocolumns: The urease case study*, Appl. Phys. Lett. **95**, 113701 (2009).

[22] V. M. Polyakov, V. Cimalla, V. Lebedev, F. Schwierz, *Impact of n-type doping on the terahertz surface emission from c-plane InN*, Phys. Status Solidi A **207**, 1353 (2010).

[23] Yuh-Hwa Chang, Yen-Sheng Lu, Yu-Liang Hong, Shangjr Gwo, J.A. Yeh, *Highly Sensitive pH Sensing Using an Indium Nitride Ion-Sensitive Field-Effect Transistor*, IEEE Sens. J. **11**, 1157 (2011).

[24] B. Monemar, P. P. Paskov, J. P. Bergman, A. A. Toropov, T. V. Shubina, T. Malinauskas, A. Usui, *Recombination of free and bound excitons in GaN*, Phys. Status Solidi B **245**, 1723 (2008).

[25] O. Jani, I. Ferguson, C. Honsberg, S. Kurtz, *Design and characterization of GaN/InGaN solar cells*, Appl. Phys. Lett. **91**, 132117 (2007).

[26] C. J. Neufeld, N. G. Toledo, S. C. Cruz, M. Iza, S. P. Denbaars, U. K. Mishra, *High quantum efficiency InGaN/GaN solar cells with 2.95 eV band gap*, Appl. Phys. Lett. **93**, 143502 (2008).

[27] X. Chen, K. D. Matthews, D. Hao, W. J. Schaff, L. F. Eastman, *Growth, fabrication, and characterization of InGaN solar cells*, Phys. Status Solidi A **205**, 1103 (2008).

[28] X.-M. Cai, S.-W. Zeng, B.-P. Zhang, *Fabrication and characterization of InGaN p-i-n homojunction solar cell*, Appl. Phys. Lett. **95**, 173504 (2009).

[29] R. Dahal, J. Li, K. Aryal, J. Y. Lin, H. X. Jiang, *InGaN/GaN multiple quantum well concentrator solar cells*, Appl. Phys. Lett. **97**, 073115 (2010).

[30] G. Rossbach, M. Feneberg, M. Röppischer, C. Werner, N. Esser, C. Cobet, T. Meisch, K. Thonke, A. Dadgar, J. Bläsing, A. Krost, R. Goldhahn, *Influence of exciton-phonon coupling and strain on the anisotropic optical response of wurtzite AlN around the band edge*, Phys. Rev. B **83**, 195202 (2011).

[31] J. Kuzmik, *Power electronics on InAlN/(In)GaN: Prospect for a record performance*, IEEE Electron Device Lett. **22**, 510 (2001).

[32] A. Dadgar, M. Neuburger, F. Schulze, J. Bläsing, A. Krtschil, I. Daumiller, M. Kunze, K.-M. Günther, H. Witte, A. Diez, E. Kohn, A. Krost, *High-current AlInN/GaN field effect transistors*, Phys. Status Solidi A **202**, 832 (2005).

[33] N. Sarazin, E. Morvan, M. A. di Forte Poisson, M. Oualli, C. Gaquiere, O. Jardel, O. Drisse, M. Tordjman, M. Magis, S. L. Delage, *AlInN/AlN/GaN HEMT Technology on SiC With 10-W/mm and 50% PAE at 10 GHz*, IEEE Electron Device Lett. **31**, 11 (2010).

[34] E. Feltin, J.-F. Carlin, J. Dorsaz, G. Christmann, R. Butté, M. Laügt, M. Ilegems, N. Grandjean, *Crack-free highly reflective AlInN/AlGaN Bragg mirrors for UV applications*, Appl. Phys. Lett. **88**, 051108 (2006).

[35] A. Altoukhov, J. Levrat, E. Feltin, J.-F. Carlin, A. Castiglia, R. Butté, N. Grandjean, *High reflectivity airgap distributed Bragg reflectors realized by wet etching of AlInN sacrificial layers*, Appl. Phys. Lett. **95**, 191102 (2009).

[36] H. Tong, J. Zhang, G. Liu, J. A. Herbsommer, G. S. Huang, N. Tansu, *Thermoelectric properties of lattice-matched AlInN alloy grown by metal organic chemical vapor deposition*, Appl. Phys. Lett. **97**, 112105 (2010).

[37] J. S. Kwak, T. Jang, K. K. Choi, Y. J. Sung, Y. H. Kim, S. Chae, S. N. Lee, K. H. Ha, O. H. Nam, Y. Park, *Fabrication of AlInGaN-based blue-violet laser diode with low input power*, Phys. Status Solidi A **201**, 2649 (2004).

[38] O. H. Nam, K. H. Ha, H. Y. Ryu, S. N. Lee, T. H. Chang, K. K. Choi, J. K. Son, J. H. Chae, S. H. Chae, H. S. Paek, Y. J. Sung, T. Sakong, H. G. Kim, H. S. Kim, Y. H. Kim, Y. J. Park, *High power AlInGaN-based blue-violet laser diodes*, in C. Mermelstein & D. P. Bour (*Hg.*), *SPIE Conference Series*, Band 6133 von *Presented at the Society of Photo-Optical Instrumentation Engineers (SPIE) Conference*, 137 (2006).

[39] S.-N. Lee, J. K. Son, H. S. Paek, Y. J. Sung, K. S. Kim, H. K. Kim, H. Kim, T. Sakong, Y. Park, K. H. Ha, O. H. Nam, *High-power AlInGaN-based violet laser diodes with InGaN optical confinement layers*, Appl. Phys. Lett. **93**, 091109 (2008).

[40] S. Masui, Y. Matsuyama, T. Yanamoto, T. Kozaki, S.-I. Nagahama, T. Mukai, *365 nm Ultraviolet Laser Diodes Composed of Quaternary AlInGaN Alloy*, Jpn. J. Appl. Phys. **42**, L1318 (2003).

[41] V. Adivarahan, A. Chitnis, J. P. Zhang, M. Shatalov, J. W. Yang, G. Simin, M. A. Khan, R. Gaska, M. S. Shur, *Ultraviolet light-emitting diodes at 340 nm using quaternary AlInGaN multiple quantum wells*, Appl. Phys. Lett. **79**, 4240 (2001).

[42] M. Shatalov, J. Zhang, A.S. Chitnis, V. Adivarahan, J. Yang, G. Simin, M.A. Khan, *Deep ultraviolet light-emitting diodes using quaternary AlInGaN multiple quantum wells*, IEEE J. Sel. Top. Quantum Electron. **8**, 302 (2002).

[43] J. P. Zhang, V. Adivarahan, H. M. Wang, Q. Fareed, E. Kuokstis, A. Chitnis, M. Shatalov, J. W. Yang, G. Simin, M. A. Khan, M. Shur, R. Gaska, *Quaternary AlInGaN Multiple Quantum Wells for Ultraviolet Light Emitting Diodes*, Jpn. J. Appl. Phys. **40**, L921 (2001).

[44] R. Gaska, J. Zhang, *Deep-UV LEDs: physics, performance, and applications*, in J.-C. Chiao, A. S. Dzurak, C. Jagadish, and D. V. Thiel (*Hg.*), *Society of Photo-Optical Instrumentation Engineers (SPIE) Conference Series*, Band 6037 von *Presented at the Society of Photo-Optical Instrumentation Engineers (SPIE) Conference*, 37 (2006).

[45] T.-C. Wang, H.-C. Kuo, Z.-H. Lee, C.-C. Chuo, M.-Y. Tsai, C.-E. Tsai, T.-D. Lee, T.-C. Lu, J. Chi, *Quaternary AlInGaN multiple quantum well 368 nm light-emitting diode*, J. Cryst. Growth **287**, 582 (2006).

[46] H. Hirayama, S. Fujikawa, N. Noguchi, J. Norimatsu, T. Takano, K. Tsubaki, N. Kamata, *222-282 nm AlGaN and InAlGaN-based deep-UV LEDs fabricated on high-quality AlN on sapphire*, Phys. Status Solidi A **206**, 1176 (2009).

[47] M.S. Shur, R. Gaska, *Deep-Ultraviolet Light-Emitting Diodes*, IEEE Trans. Electron Devices **57**, 12 (2010).

[48] S. Fujikawa, H. Hirayama, *284–300 nm Quaternary InAlGaN-Based Deep-Ultraviolet Light-Emitting Diodes on Si(111) Substrates*, Appl. Phys. Express **4**, 061002 (2011).

[49] Y.D. Jhou, S.J. Chang, Y.K. Su, C.H. Chen, H.C. Lee, C.H. Liu, Y.Y. Lee, *Quaternary AlInGaN-based photodetectors*, IET Optoelectron. **2**, 42 (2008).

[50] H. C. Lee, Y. K. Su, J. C. Lin, Y. C. Cheng, T. C. Li, K. J. Chang, *AlInGaN ultraviolet-C photodetectors with a Ni/Ir/Au multilayer metal contact*, Solid State Electron. **54**, 488 (2010).

[51] Y. Liu, T. Egawa, H. Jiang, B. Zhang, H. Ishikawa, *Novel Quaternary AlInGaN/GaN Heterostructure Field Effect Transistors on Sapphire Substrate*, Jpn. J. Appl. Phys. **45**, 5728 (2006).

[52] T. Lim, R. Aidam, P. Waltereit, T. Henkel, R. Quay, R. Lozar, T. Maier, L. Kirste, O. Ambacher, *GaN-Based Submicrometer HEMTs With Lattice-Matched InAlGaN Barrier Grown by MBE*, IEEE Electron Device Lett. **31**, 671 (2010).

[53] N. Ketteniss, L. Rahimzadeh Khoshroo, M. Eickelkamp, M. Heuken, H. Kalisch, R. H. Jansen, A. Vescan, *Study on quaternary AlInGaN/GaN HFETs grown on sapphire substrates*, Semicond. Sci. Technol. **25**, 075013 (2010).

[54] S.-N. Lee, H. S. Paek, H. Kim, K. K. Kim, Y. H. Cho, T. Jang, Y. Park, *Growth and characterization of the AlInGaN quaternary protective layer to suppress the thermal damage of InGaN multiple quantum wells*, J. Cryst. Growth **310**, 3881 (2008).

[55] G. Tamulaitis, K. Kazlauskas, S. Juršėnas, A. Žukauskas, M. A. Khan, J. W. Yang, J. Zhang, G. Simin, M. S. Shur, R. Gaska, *Optical bandgap formation in AlInGaN*

alloys, Appl. Phys. Lett. **77**, 2136 (2000).

[56] C. H. Chen, L. Y. Huang, Y. F. Chen, H. X. Jiang, J. Y. Lin, *Mechanism of enhanced luminescence in* $In_xAl_yGa_{1-x-y}N$ *quaternary alloys*, Appl. Phys. Lett. **80**, 1397 (2002).

[57] F. Wang, S.-S. Li, J.-B. Xia, H. X. Jiang, J. Y. Lin, J. Li, S.-H. Wei, *Effects of the wave function localization in AlInGaN quaternary alloys*, Appl. Phys. Lett. **91**, 061125 (2007).

[58] Hong He, Yongge Cao, Renli Fu, Hai Wang, Jiquan Huang, Changgang Huang, Meili Wang, Zhonghua Deng, *Structure and optical properties of InN and InAlN films grown by rf magnetron sputtering*, J. Mater. Sci. - Mater. Electron. **21**, 676 (2010).

[59] T. Aschenbrenner, H. Dartsch, C. Kruse, M. Anastasescu, M. Stoica, M. Gartner, A. Pretorius, A. Rosenauer, T. Wagner, D. Hommel, *Optical and structural characterization of AlInN layers for optoelectronic applications*, J. Appl. Phys. **108**, 063533 (2010).

[60] C. Stampfl, C. G. van de Walle, *Density-functional calculations for III-V nitrides using the local-density approximation and the generalized gradient approximation*, Phys. Rev. B **59**, 5521 (1999).

[61] F. Bechstedt, *Do we know the fundamental energy gap of InN?*, J. Cryst. Growth **246**, 315 (2002).

[62] J. Furthmüller, P. H. Hahn, F. Fuchs, F. Bechstedt, *Band structures and optical spectra of InN polymorphs: Influence of quasiparticle and excitonic effects*, Phys. Rev. B **72**, 205106 (2005).

[63] F. Bechstedt, J. Furthmüller, M. Ferhat, L. K. Teles, L. M. R. Scolfaro, J. R. Leite, V. Y. Davydov, O. Ambacher, R. Goldhahn, *Energy gap and optical properties of* $In_xGa_{1-x}N$, Phys. Status Solidi A **195**, 628 (2003).

[64] L. C. de Carvalho, A. Schleife, F. Bechstedt, *Influence of exchange and correlation on structural and electronic properties of AlN, GaN, and InN polytypes*, Phys. Rev. B **84**, 195105 (2011).

[65] W. Paszkowicz, R. Černý, S. Krukowski, *Rietveld refinement for indium nitride in the 105–295 K range*, Powder Diffr. **18**, 114 (2003).

[66] P. Misra, U. Behn, O. Brandt, H. T. Grahn, B. Imer, S. Nakamura, S. P. DenBaars, J. S. Speck, *Polarization anisotropy in GaN films for different nonpolar orientations studied by polarized photoreflectance spectroscopy*, Appl. Phys. Lett. **88**, 161920 (2006).

[67] M. Cardona, N. E. Christensen, *Spin orbit splittings in AlN, GaN and InN*, Solid State Commun. **116**, 421 (2000).

[68] R. Goldhahn, P. Schley, A. T. Winzer, M. Rakel, C. Cobet, N. Esser, H. Lu, W. J. Schaff, *Critical points of the band structure and valence band ordering at the* Γ *point of wurtzite InN*, J. Cryst. Growth **288**, 273 (2006).

[69] J.J. Hopfield, *Fine structure in the optical absorption edge of anisotropic crystals*, J. Phys. Chem. Solids **15**, 97 (1960).

[70] S. L. Chuang, C. S. Chang, $k\cdot p$ *method for strained wurtzite semiconductors*, Phys. Rev. B **54**, 2491 (1996).

[71] S. Ghosh, P. Waltereit, O. Brandt, H. T. Grahn, K. H. Ploog, *Electronic band structure of wurtzite GaN under biaxial strain in the M plane investigated with photoreflectance spectroscopy*, Phys. Rev. B **65**, 075202 (2002).

[72] A. Polian, M. Grimsditch, I. Grzegory, *Elastic constants of gallium nitride*, J. Appl. Phys. **79**, 3343 (1996).

[73] I. Vurgaftman, J. R. Meyer, *Band parameters for nitrogen-containing semiconductors*, J. Appl. Phys. **94**, 3675 (2003).

[74] W. Paszkowicz, S. Podsiadlo, R. Minikayev, *Rietveld-refinement study of aluminium and gallium nitrides*, J. Alloys Compd. **382**, 100 (2004).

[75] J. Bhattacharyya, S. Ghosh, H. T. Grahn, *Optical polarization properties of interband transitions in strained group-III-nitride alloy films on GaN substrates with nonpolar orientation*, Appl. Phys. Lett. **93**, 051913 (2008).

[76] I. Vurgaftman, J. R. Meyer, *Band parameters for nitrogen-containing semiconductors*, J. Appl. Phys. **94**, 3675 (2003).

[77] G. Rossbach, M. Röppischer, P. Schley, G. Gobsch, C. Werner, C. Cobet, N. Esser, A. Dadgar, M. Wieneke, A. Krost, R. Goldhahn, *Valence-band splitting and optical anisotropy of AlN*, Phys. Satus Solidi B **247**, 1679 (2010).

[78] S. Shokhovets, L. Spieß, G. Gobsch, *Spectroscopic ellipsometry of wurtzite ZnO and GaN: Examination of a special case*, J. Appl. Phys. **107**, 023509 (2010).

[79] S. Shokhovets, O. Ambacher, B. K. Meyer, G. Gobsch, *Anisotropy of the momentum matrix element, dichroism, and conduction-band dispersion relation of wurtzite semiconductors*, Phys. Rev. B **78**, 035207 (2008).

[80] Peter Y. Yu, Manuel Cardona, *Fundamentals of Semiconductors* (Springer, 2010), 4 Auflage.

[81] A Riefer, F Fuchs, C Roedl, A. Schleife, F Bechstedt, R. Goldhahn, *Interplay of excitonic effects and van Hove singularities in optical spectra: CaO and AlN polymorphs*, Phys. Rev. B **84**, 075218 (2011).

[82] R. J. Elliott, *Intensity of Optical Absorption by Excitons*, Phys. Rev. **108**, 1384 (1957).

[83] R. Goldhahn, C. Buchheim, P. Schley, A. T. Winzer, H. Wenzel, in J. Piprek (*Hg.*), *Nitride Semiconductor Devices: Principles and Simulation*, 95 (Wiley, Weinheim, 2007).

[84] C. Buchheim, R. Goldhahn, M. Rakel, C. Cobet, N. Esser, U. Rossow, D. Fuhrmann, A. Hangleiter, *Dielectric function and critical points of the band structure for AlGaN alloys*, Phys. Status Solidi B **242**, 2610 (2005).

[85] S. Shokhovets, R. Goldhahn, G. Gobsch, S. Piekh, R. Lantier, A. Rizzi, V. Lebedev, W. Richter, *Determination of the anisotropic dielectric function for wurtzite AlN and GaN by spectroscopic ellipsometry*, J. Appl. Phys. **94**, 307 (2003).

[86] M. Feneberg, R. A. R. Leute, B. Neuschl, K. Thonke, M. Bickermann, *High excitation and high resolution photoluminescence spectra of bulk AlN*, Phys. Rev. B **82**, 075208 (2010).

[87] V. Cimalla, M. Niebelschütz, G. Ecke, V. Lebedev, O. Ambacher, M. Himmerlich, S. Krischok, J. A. Schaefer, H. Lu, W. J. Schaff, *Surface band bending at nominally undoped and Mg-doped InN by Auger Electron Spectroscopy*, Phys. Status Solidi A **203**, 59 (2006).

[88] P. D. C. King, T. D. Veal, C. F. McConville, F. Fuchs, J. Furthmüller, F. Bechstedt, P. Schley, R. Goldhahn, J. Schörmann, D. J. As, K. Lischka, D. Muto, H. Naoi, Y. Nanishi, H. Lu, W. J. Schaff, *Universality of electron accumulation at wurtzite c- and a-plane and zinc-blende InN surfaces*, Appl. Phys. Lett. **91**, 092101 (2007).

[89] M. Himmerlich, S. Krischok, V. Lebedev, O. Ambacher, J. A. Schaefer, *Morphology and surface electronic structure of MBE grown InN*, J. Cryst. Growth **306**, 6 (2007).

[90] M. Himmerlich, A. Eisenhardt, J. A. Schaefer, S. Krischok, *PAMBE growth and in-situ characterisation of clean* (2×2) *and* $(\sqrt{3} \times \sqrt{3})$ $R30°$ *reconstructed InN(0001) thin films*, Phys. Status Solidi B **246**, 1173 (2009).

[91] A. Eisenhardt, S. Reiß, M. Himmerlich, J. A. Schaefer, S. Krischok, *Changes in the valence band structure of as-grown InN(0001)-*2×2 *surfaces upon exposure to oxygen and water*, Phys. Satus Solidi A **207**, 1037 (2010).

[92] W. M. Linhart, T. D. Veal, P. D. C. King, G. Koblmüller, C. S. Gallinat, J. S. Speck, C. F. McConville, *Surface, bulk, and interface electronic properties of non-*

polar InN, Appl. Phys. Lett. **97**, 112103 (2010).

[93] A. Belabbes, J. Furthmüller, F. Bechstedt, *Electronic properties of polar and nonpolar InN surfaces: A quasiparticle picture*, Phys. Rev. B **84**, 205304 (2011).

[94] A. Kasic, M. Schubert, Y. Saito, Y. Nanishi, G. Wagner, *Effective electron mass and phonon modes in n-type hexagonal InN*, Phys. Rev. B **65**, 115206 (2002).

[95] R. M. A. Azzam, N.M. Bashara, *Ellipsometry and polarized light* (Elsevier Science B.V., 1977).

[96] A. Röseler, *Infrared spectroscopic ellipsometry* (Akademie-Verlag, Berlin, 1990).

[97] C. Cobet, *Linear optical properties of III-nitride semiconductors between 3 and 30 eV*, Dissertation, Technische Universität Berlin (2005).

[98] C. Cobet, R. Goldhahn, W. Richter, N. Esser, *Identification of van Hove singularities in the GaN dielectric function: a comparison of the cubic and hexagonal phase*, Phys. Status Solidi B **246**, 1440 (2009).

[99] R. Goldhahn, *Dielectric function of nitride semiconductors: recent experimental results*, Acta Phys. Pol. A **104**, 123 (2003).

[100] D.A.G. Bruggeman, *Berechnung verschiedener physikalischer Konstanten von heterogenen Substanzen*, Ann. Phys. **24**, 636 (1935).

[101] T. D. Veal, L. F. J. Piper, I. Mahboob, H. Lu, W. J. Schaff, C. F. McConville, *Electron accumulation at InN/AlN and InN/GaN interfaces*, Phys. Status Solidi C **2**, 2246 (2005).

[102] C. Martin, K. S. A. Butcher, M. Wintrebert-Fouquet, A. Fernandes, T. Dabbs, P. P.-T. Chen, R. Carmen, *Modeling and experimental analysis of RPCVD based nitride film growth*, in *Society of Photo-Optical Instrumentation Engineers (SPIE) Conference Series*, Band 6894 von *Society of Photo-Optical Instrumentation Engineers (SPIE) Conference Series* (2008).

[103] R. Torres, *Performance of single use purifiers vs. regenerable purifiers for growth of high brightness gallium nitride LEDs*, J. Cryst. Growth **261**, 231 (2004).

[104] C. Y. Hwang, M. J. Schurman, W. E. Mayo, Y. C. Lu, R. A. Stall, T. Salagaj, *Effect of structural defects and chemical impurities on hall mobilities in low pressure MOCVD grown GaN*, J. Electron. Mater.. **26**, 243 (1997).

[105] A. Saxler, D. Walker, P. Kung, X. Zhang, M. Razeghi, J. Solomon, W. C. Mitchel, H. R. Vydyanath, *Comparison of trimethylgallium and triethylgallium for the growth of GaN*, Appl. Phys. Lett. **71**, 3272 (1997).

[106] A. Dadgar, J. Bläsing, A. Diez, A. Krost, *Crack-Free, Highly Conducting GaN Layers on Si Substrates by Ge Doping*, Appl. Phys. Express **4**, 011001 (2011).

[107] M. A. Herman, W. Richter, H. Sitter, *Physical Principles and Technical Implementation* (Springer, Berlin, 2004).

[108] K. Haberland, J.T. Mullins, T. Schenk, T. Trepk, L. Considine, A. Pakes, A. Taylor, J.-T. Zettler, *First real-time true wafer temperature and growth rate measurements in a closed-coupled showerhead MOVPE reactor during growth of InGa(AsP)*, in *Indium Phosphide and Related Materials, 2003. International Conference on*, 44 (2003).

[109] H. Hardtdegen, N. Kaluza, Z. Sofer, Y. S. Cho, R. Steins, H. L. Bay, Y. Dikme, H. Kalisch, R. H. Jansen, M. Heuken, A. Strittmatter, L. Reißmann, D. Bimberg, J.-T. Zettler, *New method for the in situ determination of $Al_xGa_{1-x}N$ composition in MOVPE by real-time optical reflectance*, Phys. Status Solidi A **203**, 1645 (2006).

[110] R. Steins, N. Kaluza, H. Hardtdegen, M. Zorn, K. Haberland, J.-T. Zettler, *Use of SiC band gap temperature dependence for absolute calibration of emissivity corrected pyrometers in III-nitride MOVPE*, J. Cryst. Growth **272**, 81 (2004).

[111] M. Drago, *MOVPE growth of InN analyzed by in-situ spectroscopic ellipsometry*, Dissertation, TU Berlin (2007).

[112] A. Knauer, T. Kolbe, S. Einfeldt, M. Weyers, M. Kneissl, T. Zettler, *Optimization of InGaN/(In,Al,Ga)N based near UV-LEDs by MQW strain balancing with in-situ wafer bow sensor*, Phys. Status Solidi A **206**, 211 (2009).

[113] A. Krost, F. Schulze, A. Dadgar, G. Strassburger, K. Haberland, T. Zettler, *Simultaneous measurement of wafer curvature and true temperature during metalorganic growth of group-III nitrides on silicon and sapphire*, Phys. Status Solidi B **242**, 2570 (2005).

[114] F. Brunner, V. Hoffmann, A. Knauer, E. Steimetz, T. Schenk, J.-T. Zettler, M. Weyers, *Growth optimization during III-nitride multiwafer MOVPE using real-time curvature, reflectance and true temperature measurements*, J. Cryst. Growth **298**, 202 (2007).

[115] L. E. Ramos, J. Furthmüller, L. M. R. Scolfaro, J. R. Leite, F. Bechstedt, *Substitutional carbon in group-III nitrides: Ab initio description of shallow and deep levels*, Phys. Rev. B **66**, 075209 (2002).

[116] X. M. Duan, C. Stampfl, *Defect complexes and cluster doping of InN: First-principles investigations*, Phys. Rev. B **79**, 035207 (2009).

[117] K. Wang, N. Miller, R. Iwamoto, T. Yamaguchi, M. A. Mayer, T. Araki, Y. Nanishi, K. M. Yu, E. E. Haller, W. Walukiewicz, J. W. Ager, *Mg doped InN and*

confirmation of free holes in InN, Appl. Phys. Lett. **98**, 042104 (2011).

[118] M. A. Mayer, S. Choi, O. Bierwagen, H. M. Smith, E. E. Haller, J. S. Speck, W. Walukiewicz, *Electrical and optical properties of p-type InN*, J. Appl. Phys. **110**, 123707 (2011).

[119] X. Wang, S.-B. Che, Y. Ishitani, A. Yoshikawa, *Experimental determination of strain-free Raman frequencies and deformation potentials for the* E_2 *high and* A_1*(LO) modes in hexagonal InN*, Appl. Phys. Lett. **89**, 171907 (2006).

[120] V. Y. Davydov, A. A. Klochikhin, *Electronic and vibrational states in InN and* In_xGa_{1-x} *N solid solutions*, Semiconductors **38**, 861 (2004).

[121] P. Schley, R. Goldhahn, A. T. Winzer, G. Gobsch, V. Cimalla, O. Ambacher, H. Lu, W. J. Schaff, M. Kurouchi, Y. Nanishi, M. Rakel, C. Cobet, N. Esser, *Dielectric function and Van Hove singularities for In-rich* $In_xGa_{1-x}N$ *alloys*: *Comparison of N- and metal-face materials*, Phys. Rev. B **75**, 205204 (2007).

[122] E. Burstein, *Anomalous Optical Absorption Limit in InSb*, Phys. Rev. **93**, 632 (1954).

[123] T. S. Moss, *The Interpretation of the Properties of Indium Antimonide*, Proc. Phys. Soc. London, Sect. B **67**, 775 (1954).

[124] M. P. Hasselbeck, P. M. Enders, *Electron-electron interactions in the nonparabolic conduction band of narrow-gap semiconductors*, Phys. Rev. B **57**, 9674 (1998).

[125] E. O. Kane, *Band structure of indium antimonide*, J. Phys. Chem. Solids **1**, 249 (1957).

[126] L. F. J. Piper, T. D. Veal, C. F. McConville, H. Lu, W. J. Schaff, *Origin of the n-type conductivity of InN: The role of positively charged dislocations*, Appl. Phys. Lett. **88**, 252109 (2006).

[127] V. Cimalla, V. Lebedev, F. M. Morales, R. Goldhahn, O. Ambacher, *Model for the thickness dependence of electron concentration in InN films*, Appl. Phys. Lett. **89**, 172109 (2006).

[128] I. Gorczyca, S. P. Łepkowski, T. Suski, N. E. Christensen, A. Svane, *Influence of indium clustering on the band structure of semiconducting ternary and quaternary nitride alloys*, Phys. Rev. B **80**, 075202 (2009).

[129] M. D. McCluskey, C. G. van de Walle, L. T. Romano, B. S. Krusor, N. M. Johnson, *Effect of composition on the band gap of strained* $In_xGa_{1-x}N$ *alloys*, J. Appl. Phys. **93**, 4340 (2003).

[130] S. Pereira, M. R. Correia, T. Monteiro, E. Pereira, E. Alves, A. D. Sequeira, N. Franco, *Compositional dependence of the strain-free optical band gap in* $In_xGa_{1-x}N$ *layers*, Appl. Phys. Lett. **78**, 2137 (2001).

[131] R. Kudrawiec, M. Siekacz, M. Kryśko, G. Cywiński, J. Misiewicz, C. Skierbiszewski, *Contactless electroreflectance of InGaN layers with indium content* $\leq$*=36%: The surface band bending, band gap bowing, and Stokes shift issues*, J. Appl. Phys. **106**, 113517 (2009).

[132] P. G. Moses, C. G. van de Walle, *Band bowing and band alignment in InGaN alloys*, Appl. Phys. Lett. **96**, 021908 (2010).

[133] J. F. Muth, J. H. Lee, I. K. Shmagin, R. M. Kolbas, H. C. Casey, Jr., B. P. Keller, U. K. Mishra, S. P. Denbaars, *Absorption coefficient, energy gap, exciton binding energy, and recombination lifetime of GaN obtained from transmission measurements*, Appl. Phys. Lett. **71**, 2572 (1997).

[134] D. E. Aspnes, *Direct Verification of the Third-Derivative Nature of Electroreflectance Spectra*, Phys. Rev. Lett. **28**, 168 (1972).

[135] K. Okamoto, A. Kaneta, Y. Kawakami, S. Fujita, J. Choi, M. Terazima, T. Mukai, *Confocal microphotoluminescence of InGaN-based light-emitting diodes*, J. Appl. Phys. **98**, 064503 (2005).

[136] D. Dobrovolskas, J. Mickevičius, E. Kuokštis, G. Tamulaitis, M. Shur, M. Shatalov, J. Yang, R. Gaska, *Confocal spectroscopy of InGaN LED structures*, J. Phys. D: Appl. Phys. **44**, 135104 (2011).

[137] F. A. Ponce, S. Srinivasan, A. Bell, L. Geng, R. Liu, M. Stevens, J. Cai, H. Omiya, H. Marui, S. Tanaka, *Microstructure and electronic properties of InGaN alloys*, Phys. Status Solidi B **240**, 273 (2003).

[138] S. Kret, F. Ivaldi, K. Sobczak, R. Czernecki, M. Leszczyński, *Inhomogeneities of InGaN/GaN MOVPE multi quantum wells grown with a two temperatures process studied by transmission electron microscopy*, Phys. Status Solidi A **207**, 1101 (2010).

[139] G. R. Mutta, P. Ruterana, J. L. Doualan, M. P. Chauvat, F. Ivaldi, S. Kret, N. A. K. Kaufmann, A. Dussaigne, D. Martin, N. Grandjean, *Investigation of the In composition in InGaN/GaN quantum wells deposited by MOVPE and/or MBE with emission from violet to green*, Phys. Status Solidi B **248**, 1187 (2011).

[140] S. Chichibu, T. Azuhata, T. Sota, S. Nakamura, *Spontaneous emission of localized excitons in InGaN single and multiquantum well structures*, Appl. Phys. Lett. **69**, 4188 (1996).

[141] Y. Narukawa, Y. Kawakami, M. Funato, S. Fujita, S. Fujita, S. Nakamura, *Role of self-formed InGaN quantum dots for exciton localization in the purple laser diode emitting at 420 nm*, Appl. Phys. Lett. **70**, 981 (1997).

[142] R. Goldhahn, P. Schley, A. T. Winzer, G. Gobsch, V. Cimalla, O. Ambacher, M. Rakel, C. Cobet, N. Esser, H. Lu, W. J. Schaff, *Detailed analysis of the dielectric function for wurtzite InN and In-rich InAlN alloys*, Phys. Status Solidi A **203**, 42 (2006).

[143] R. E. Jones, R. Broesler, K. M. Yu, J. W. Ager, E. E. Haller, W. Walukiewicz, X. Chen, W. J. Schaff, *Band gap bowing parameter of* $In_{1-x}Al_xN$, J. Appl. Phys. **104**, 123501 (2008).

[144] C. Hums, A. Gadanecz, A. Dadgar, J. Bläsing, H. Witte, T. Hempel, A. Dietz, P. Lorenz, S. Krischok, J. A. Schäfer, J. Christen, A. Krost, *MOVPE growth and characterization of AllnN FET structures on Si(111)*, in *Advances in GaN, GaAs, SiC and related alloys on silicon substrates*, Band 1068 (Materials Research Society symposium proceedings, 2008).

[145] O. Ambacher, R. Dimitrov, M. Stutzmann, B.E. Foutz, M.J. Murphy, J.A. Smart, J.R. Shealy, N.G. Weimann, K. Chu, M. Chumbes, B. Green, A.J. Sierakowski, W.J. Schaff, L.F. Eastman, *Role of Spontaneous and Piezoelectric Polarization Induced Effects in Group-III Nitride Based Heterostructures and Devices*, Phys. Satus Solidi B **216**, 381 (1999).

[146] K. Wang, R. R. Reeber, *Thermal expansion and elastic properties of InN*, Appl. Phys. Lett. **79**, 1602 (2001).

[147] A.F. Wright, *Elastic properties of zinc-blende and wurtzite AlN, GaN, and InN*, J. Appl. Phys. **82**, 2833 (1997).

[148] Laurie E. McNeil, Marcos Grimsditch, Roger H. French, *Vibrational Spectroscopy of Aluminum Nitride*, J. Am. Ceram. Soc. **76**, 1132 (1993).

[149] P. Carrier, S.-H. Wei, *Theoretical study of the band-gap anomaly of InN*, J. Appl. Phys. **97**, 033707 (2005).

[150] P.Y. Yu, M. Cardona, *Fundamentals of semiconductors* (Springer-Verlag, Berlin, 1999).

[151] L. X. Benedict, T. Wethkamp, K. Wilmers, C. Cobet, N. Esser, E. L. Shirley, W. Richter, M. Cardona, *Dielectric function of wurtzite GaN and AlN thin films*, Solid State Comm. **112**, 129 (1999).

[152] T. S. Oh, J. Ock Kim, H. Jeong, Y. S. Lee, S. Nagarajan, K. Y. Lim, C.-H. Hong, E.-K. Suh, *Growth and properties of Al-rich* $In_xAl_{1-x}N$ *ternary alloy grown on GaN template by metalorganic chemical vapour deposition*, J. Phys. D: Appl.

Phys. **41**, 095402 (2008).

[153] W. Terashima, S. Che, Y. Ishitani, A. Yoshikawa, *Growth and Characterization of AlInN Ternary Alloys in Whole Composition Range and Fabrication of InN/AlInN Multiple Quantum Wells by RF Molecular Beam Epitaxy*, Jpn. J. Appl. Phys. **45**, 539 (2006).

[154] J. Kamimura, T. Kouno, S. Ishizawa, A. Kikuchi, K. Kishino, *Growth of high-In-content InAlN nanocolums on Si(111) by RF-plasma-assisted molecular-beam epitaxy*, J. Cryst. Growth **300**, 160 (2007).

[155] C. Buchheim, M. Röppischer, R. Goldhahn, G. Gobsch, C. Cobet, C. Werner, N. Esser, A. Dadgar, M. Wieneke, J. Bläsing, A. Krost, *Influence of anisotropic strain on excitonic transitions in a-plane GaN films*, Microelectron. J. **40**, 322 (2009).

[156] L. Rahimzadeh Khoshroo, C. Mauder, H. Behmenburg, J. Woitok, W. Zander, J. Gruis, B. Reuters, J. Schubert, A. Vescan, M. Heuken, H. Kalisch, R. H. Jansen, *Epitaxy and characterisation of AlInGaN heterostructures for HEMT application*, Phys. Status Solidi C **6**, 470 (2009).

[157] Y. Pan, T. Yu, Z. Yang, H. Wang, Z. Qin, X. Hu, K. Wang, S. Yao, G. Zhang, *Influence of growth rate on structural and optical properties of AlInGaN quaternary epilayers*, J. Cryst. Growth **298**, 341 (2007).

[158] C. B. Soh, S. J. Chua, S. Tripathy, W. Liu, D. Z. Chi, *The influence of V defects on luminescence properties of AlInGaN quaternary alloys*, J. Phys.: Condens. Matter **17**, 729 (2005).

[159] J. Liu, *Structural and optical properties of quaternary AlInGaN epilayers grown by MOCVD with various TMGa flows*, J. Cryst. Growth **260**, 388 (2004).

[160] S. Fernández-Garrido, A. Redondo-Cubero, R. Gago, F. Bertram, J. Christen, E. Luna, A. Trampert, J. Pereiro, E. Muñoz, E. Calleja, *Effect of the growth temperature and the AlN mole fraction on In incorporation and properties of quaternary III-nitride layers grown by molecular beam epitaxy*, J. Appl. Phys. **104**, 083510 (2008).

[161] S. Fernández-Garrido, J. Pereiro, F. González-Posada, E. Muñoz, E. Calleja, A. Redondo-Cubero, R. Gago, *Photoluminescence enhancement in quaternary III-nitrides alloys grown by molecular beam epitaxy with increasing Al content*, J. Appl. Phys. **103**, 046104 (2008).

[162] R. Goldhahn, C. Buchheim, P. Schley, A. T. Winzer, H. Wenzel, *Optical Constants of Bulk Nitrides*, in J. Piprek (*Hg.*), *Nitride Semiconductor Devices: Principles and Simulation*, 95 (Wiley-VCH, Weinheim, 2007).